JAERI-M
85-027

EVALUATION REPORT ON CCTF CORE-II REFLOOD TEST C2-6 (RUN 64)

—Effect of radial power profile—

March 1985

Hajime AKIMOTO, Tadashi IGUCHI, Kazuharu OKABE,*
Jun SUGIMOTO, Tsutomu OKUBO and Yoshio MURAO

日本原子力研究所
Japan Atomic Energy Research Institute

JAERI-Mレポートは，日本原子力研究所が不定期に公刊している研究報告書です。
入手の問合わせは，日本原子力研究所技術情報部情報資料課（〒319－11茨城県那珂郡東海村）あて，お申しこしください。なお，このほかに財団法人原子力弘済会資料センター（〒319-11茨城県那珂郡東海村日本原子力研究所内）で複写による実費頒布をおこなっております。

JAERI-M reports are issued irregularly.
Inquiries about availability of the reports should be addressed to Information Division, Department of Technical Information, Japan Atomic Energy Research Institute, Tokai-mura, Naka-gun, Ibaraki-ken 319-11, Japan.

編集兼発行　日本原子力研究所
印　　刷　日立高速印刷株式会社

JAERI-M 85-027

Evaluation Report on CCTF Core-II Reflood Test C2-6 (Run 64) - Effect of radial power profile -

Hajime AKIMOTO, Tadashi IGUCHI, Kazuharu OKABE*
Jun SUGIMOTO, Tsutomu OKUBO and Yoshio MURAO

Department of Nuclear Safety Research,
Tokai Research Establishment, JAERI

(Received January 31, 1985)

In order to evaluate the effect of the radial power profile on the system behavior and the core thermal hydraulic behavior during the reflood phase of a PWR LOCA, a test was performed using the Cylindrical Core Test Facility(CCTF) with the flat radial power profile. The test was conducted with the same total core power as that of the steep radial power test C2-5(Run 63). Through the comparisons of the results from these two tests, the following conclusions were obtained:
(1)The radial power profile in the core has weak effect on the thermal hydraulic behavior in the primary system except the core. (2)Almost the same differential pressure was observed at various elevations in the periphery of the core regardless of different radial power profile. The result suggests that the core differential pressure is determined mainly by the total power and the total stored energy rather than by the local power and the local stored energy. (3)The test results support the single channel core model with the average power rod used in the reactor safety analysis codes such as REFLA-1DS, WREM for the evaluation of the overall system behavior. (4)In the steep radial power test, the heat transfer coefficient in the central(high power) region was higher than that in the peripheral(low power) region. The tendency was not explained by the estimation with the heat transfer correlation developed by Murao and Sugimoto assuming that the void fraction was uniform in a horizontal cross section. It is necessary to study more the dependency of core heat transfer on the radial power profile in the wide core.

The work was performed under the contract with the Atomic Energy Bureau of Science and Technology Agency of Japan.

* Mitsubishi Atomic Power Industry

Keywords: Reactor Safety, PWR, LOCA, Reflood, Radial Power Profile
Thermal Hydraulic Behavior, Heat Transfer

大型再冠水円筒第２次炉心試験Ｃ２－６（Run64）評価報告書 －炉心内半径方向出力分布の影響－

日本原子力研究所東海研究所安全工学部

秋本　肇・井口　正・岡部　一治*
杉本　純・大久保　努・村尾　良夫

（１９８５年１月31日受理）

加圧水型原子炉の冷却材喪失事故再冠水期におけるシステム挙動と炉心内熱水力挙動に対する炉心内半径方向出力分布形の影響を調べる目的で，平担な半径方向出力分布の試験を円筒炉心試験装置を用いて行った。試験は急峻出力試験Ｃ２－５（Run 63）と等しい全炉心出力で実施した。両試験結果の比較検討から以下のことが明らかとなった。

(1)炉心を除く一次系内での熱水力挙動に対して，炉心内半径方向出力分布の影響は小さかった。

(2)炉心内半径方向出力分布形によらず，炉心周辺部ではほぼ等しい差圧が各高さ位置で観察された。炉心内での局所出力や局所蓄積エネルギよりもむしろ炉心全出力や全蓄積エネルギにより炉心内差圧が主として決定されることが示唆された。

(3)上述の試験結果は，ＲＥＦＬＡ－１ＤＳ，ＷＲＥＭ等の原子炉安全解析コードによるシステム解析で採られている平均出力棒による単一チャンネルの炉心解析手法を支持する。

(4)急峻半径方向出力分布試験では，炉心中央（高出力）領域での熱伝達率が，炉心周辺（低出力）領域での熱伝達率に比べて高かった。村尾・杉本の熱伝達率相関式を用い，炉心内ボイド率が水平断面内で一様であることを仮定した評価では，上記の熱伝達率の傾向を説明できなかった。今後半径方向出力分布が広い炉心での炉心冷却に与える影響についてさらに検討する必要がある。

本報告書は，電源開発促進対策特別会計法に基づき，科学技術庁からの受託によって行った研究の成果である。

＊　三菱原子力工業

Contents

目　　次

List of figures

List of tables

1. Introduction

A reflood test program using large scale test facilities has been conducted at Japan Atomic Energy Research Institute(JAERI)[1]-[4]. The facilities are the Cylindrical Core Test Facility(CCTF) and the Slab Core Test Facility(SCTF). This report presents an evaluation for the flat radial power test C2-6(Run 64), which was performed with CCTF on May 26,1983.

The CCTF is an experimental facility designed to model a full-height core section, four primary loops and other major components of a pressurized water reactor(PWR). This facility is used to provide information of thermal-hydraulic behaviors in pressure vessel (core, downcomer and upper and lower plenums) and in primary loops including steam generators and pump simulators during the refill and reflood phases of a hypothetical loss-of-coolant accident(LOCA) of a PWR.

The objectives of the test program using the CCTF are:

a. Demonstration of capability of emergency core cooling system (ECCS) during refill and reflood phases.
b. Verification of reflood analysis codes.
c. Collection of information to improve thermal-hydraulic models in the analysis codes.

As the first series of CCTF tests, the CCTF Core-I series was initiated in March 1979 and completed in April 1981. Subsequently, as the second series of CCTF tests, the CCTF Core-II series was initiated in March 1982.

The main objectives of the flat power test C2-6(Run 64) are (1)to study the core radial power profile effect on the system and core cooling behavior, and (2)to confirm the validity of the one-dimensional treatment in the safety analyses of a PWR LOCA. The test was planned to perform with the flat core radial power profile as the counter part test of the steep core radial power test C2-5(Run 63) in the CCTF Core-II series. The total core power and initial stored energy in core were planned to be identical with the steep radial power test.

This report presents the test results of the flat radial power test in comparison with the results from the steep radial power test for reviewing of the test data and the radial power profile effect under gravity feed condition.

2. Test description

2.1 Test facility

A bird's eye view and schematic diagram of the CCTF are shown in Figs. 2.1 and 2.2, respectively. The scaled dimensions of the components are given in Tables 2.1 and 2.2.

The differences between the CCTF-I and CCTF-II are:

(1) Axial peaking factor of heater rod,
(2) Local peaking factor of heater rod in a bundle,
(3) Grid spacer,
(4) Upper plenum internals, plugging devices in top nozzle region and a upper ring,
(5) Vent valves,
(6) Downcomer and upper plenum injection systems,
(7) Instruments.

2.1.1 Pressure vessel and internals

The pressure vessel is of a cylindrical type as shown in Fig. 2.3. The height is the same as the reference reactor pressure vessel. The dimension in the radial direction is scaled down based on the core flow area scaling, that is, 1/21.44. The upper ring was newly attached for the installation of the upper plenum ECC water injection lines and the instruments. Four vent valves and two downcomer water injection nozzles, which are called Core Flooding Nozzle(CFN), are also newly installed in the CCTF Core-II facility as shown in Figs. 2.3 and 2.4. Vent valves and CFNs are forcedly closed in this test.

The cross section of the pressure vessel is shown in Fig. 2.5. The dimensions of the pressure vessel is shown in Fig. 2.5. The core consists of thirty-two 8x8 rod bundles arranged in a cylindrical configuration. The rod bundles simulate Westinghouse 15x15 type fuel assemblies.

The downcomer is an annulus of 61.5 mm gap. In determining the gap size, the flow area of the core baffle region was added to that of the dowmcomer region. Thus, the core baffle flow area is included in the downcomer simulation in the CCTF. The vessel wall is constructed of carbon steel cladded with stainless steel lining. The wall thickness is 90 mm.

The design of upper plenum internals is based on that of the Westinghouse PWR with 17x17 type fuel assembly. The internals cosists of ten control-rod guide tubes, ten support columns and twelve open holes as shown in Fig. 2.6. The configuration of each intenal is illustrated in Fig. 2.7. The radius of each internal is scaled down by factor of 8/15 from that of a PWR. Flow resistance baffle plates are inserted into the guide tubes. Figure 2.8 shows the configurations of the baffle plates.

The end box and the upper core support plate(UCSP) are installed above the core. Figure 2.9 shows the structure of the end box tie plate for one heater rod bundle. The tie plate is a 10 mm thick perforated plate. Plugging devices are installed in the CCTF-II facility in order to simulate the flow resistance more correctly as shown in Figs. 2.9 and 2.10. The UCSP is a 60 mm thick perforated plate.

2.1.2 Heater rod assembly

Figure 2.11 shows arrangement of heater rods in a bundle. Each bundle consists of fifty-seven heater rods and seven non-heated rods. All heater rods in a bundle have the same power density in the CCTF-II facility. As shown in Fig. 2.5 the core is subdivided into three regions to achieve a desired radial power profile.

Figure 2.12 shows the configuration of a heater rod. A heater rod consists of nichrome heating element, magnesium oxide(MgO) and boron nitride(BN) insulators, and inconel-600 sheath. BN is used only for the central part of the heated part. The length of the core heated part is 3.66 m and the diameter of the heater rod is 10.7 mm. The thickness of the sheath wall is 1.0 mm. By changing the pitch of the helical coil of the heating element, a 17-step chopped-cosine axial-power profile is attained as shown in Fig. 2.13. The axial peaking factor is 1.40 in the CCTF-II, instead of 1.489 in the CCTF-I.

Non-heated rods are either stainless steel pipe or solid pipe of 13.8 mm O.D. All pipes are utilized for installation of instruments such as superheat steam probes and thermocouples. All bars are used to support the assembly loads.

The heater rods and non-heated rods are held in radial position by grid spacers which are located at six elevations along the axial length as shown in Fig. 2.13. A grid spacer is a lattice composed of stainless plates of 0.4 and 0.8 mm thick and 40 mm high. The top and bottom edges

of the stainless steel plates are sharped in the CCTF-II.

The heater rods penetrate through the bottom plate of the pressure vessel to facilitate the connection of the power cables. The outer diameter of the heater rods in the lower plenum is reduced to 8.6 mm.

2.1.3 Primary loops and ECCS

The CCTF has three intact and a broken loops. The facility simulates the double-ended cold-leg break. Figures 2.14 and 2.15 show the primary loop arrangement in the CCTF. The inside diameter of the pipings is scaled down in proportion to the core flow area scaling. The length of each piping section is almost the same as the corresponding sections of the reference PWR.

Figure 2.16 shows the steam generator(SG) simulator. The SG is of U-tube and shell type. The primary coolant passes through the tubes. The secondary side is filled with water. The steam generator simulators of two loops are housed in a single shell assembly. The wall thickness of the U-tube is 2.9 mm instead of 1.27 mm in the reference PWR system because of higher pressure difference between the primary and secondary sides.

The pump simulator consists of the casing and vane simulators and an orifice plate as shown in Fig. 2.17. The each loop flow resistance is simulated with the orifice plate.

ECC water can be injected into each cold leg, lower plenum, upper plenum, and downcomer as shown in Fig. 2.14.

Figure 2.18 shows the upper plenum injection device. The radial location of the water injection pipes are shown in Fig. 2.19.

2.1.4 Instrumentation

The instrumentation is divided into two groups. One is JAERI-supplied instruments and the other is USNRC supplied one.

JAERI instrumentation includes 1316 channels and are recorded on magnetic tapes. The measuring location of the selected data is summarized in Appendix A.

USNRC supplied instruments include the advanced instrumentation for the two-phase flow measurement. 536 channels are used to record data from these instruments. Table 2.3 show the names and quanties of these

instruments.

2.2 Planned test procedure

In the preparation for the test, the Acc tank, the LPCI tank, the saturated water tank, and the secondary side of the steam generators were filled with water which was purified with ion exchange resin. After all the components and instruments were inspected for mechanical and electrical leakages, the instruments were checked for their zero points and sensitivities.

After these preparatory operations, the primary system was heated to the specified temperatures (downcomer wall:471 K, core internals: 393 K, and the primary piping wall: 393 K) and pressurized to a specified pressure (0.2 MPa) by introduing steam into the primary system. The water in the Acc and LPCI tanks was heated to the specified temperature(308 K). The water in the LPCI tank was circulated through the circulation line to preheat the line to the same temperature as the LPCI water. The water in the saturated water tank was preheated to the saturation temperature(393 K) at the expected primary system pressure(0.2 MPa). The water in the secondary side of each steam generator was also heated and pressurized to the specified temperature(539 K) and pressure(5.2 MPa).

After establishing these initial conditions of the test, the lower plenum was filled with the saturated water to the specified level(0.90 m from the bottom of the pressure vessel). When all initial test conditions were stabilized at the allowable tolerance, electric power was supplied to the heater rods in the core and the data recording was started. The temperature rises of the rods were monitored by using a computer. When a specified clad surface temperature(871 K) was attained at more than 20 monitoring locations of the clad surface temperatures, Acc water injection into the lower plenum was initiated(injection rate: 0.105 m^3/s). The clad surface temperature (871 K) of the heater rods for the initiation of the Acc injection into the lower plenum was predetermined by the interpolation of the clad surface temperatures at the test initiation(393 K) and the reflood initiation(914 K). Decay of the core power was programmed to begin when the water level in the pressure vessel was estimated to reach the bottom of the core heated part. The decay of core power decay followed the normarized decay curve of (ANSx1.0 + Actinidex1.1(40 s after scram)).

When the water level in the pressure vessel was estimated to reach the specified level(0.5 m from the bottom of the core heated section), the injection location of Acc water was changed from the lower plenum to the ECC ports in the intact cold legs. The Acc injection into the cold legs was planned to be 0.0892 m^3/s for 11 s. This is defined as the Acc mode in the CCTF tests. After a specified time(11 s), the valves in the Acc lines and the LPCI circulation line started to close. The valves in the LPCI injection lines started to open at the same time in order to switch the ECC water injection mode. The ECC water injection was planned to be 0.0111 m^3/s. This ECC water injection is defined as the LPCI mode in the CCTF tests.

The generated steam in core flowed with the entrained water via primary loops to the containment tanks. The steam was then exhausted to the atmosphere through the flow control valve. The pressure in the containment tank was maintained at the specified level(0.2 MPa). After all thermocouples on the surface of the heater rods were quenched, the power supply to the heater rods and the ECC water injection were terminated. Then, the data recording system was stopped.

Table 2.1 CCTF Component scaled dimensions

Component		PWR	JAERI	Ratio
Pressure vessel				
Vessel inside diameter	(mm)	4394 (173")	1084	
Vessel thickness	(mm)	216 (8 1/2")	90	
Core barrel outside diameter	(mm)	3874	961	
Core barrel inside diameter	(mm)	3760	929	
Thermal shield outside diameter	(mm)	4170		
Thermal shield inside diameter	(mm)	4030		
Downcomer length	(mm)	4849	4849	1/1
Downcomer gap	(mm)	114.3	61.5	
Downcomer flow area	(m^2)	4.23	0.197	1/21.44
Lower plenum volume	(m^3)	29.6	1.38	1/21.44
Upper plenum volume	(m^3)	43.6	2.76	1/15.8
Fuel (heater rod) assembly				
Number of bundles	(—)	193	32	
Rod array	(—)	15×15	8×8	
Rod heated length	(mm)	3660	3660	1/1
Rod pitch	(mm)	14.3	14.3	1/1
Fuel rod outside diameter	(mm)	10.72	10.7	1/1
Thimble tube diameter	(mm)	13.87	13.8	1/1
Instrument tube diameter	(mm)	13.87	13.8	1/1
Number of heater rods	(—)	39372	1824	1/21.58
Number of non-heated rods	(—)	4053	244	1/18.09
Core flow area	(m^2)	5.29	0.25	1/21.2
Core fluid volume	(m^3)	17.95	0.915	1/19.6
Primary loop				
Hot leg inside diameter	(mm)	736.6 (29")	155.2	1/4.75
Hot leg flow area	(m^2)	0.426	0.019	1/22.54
Hot leg length	(mm)	3940	3940	1/1
Pump suction inside diameter	(mm)	787.4 (31")	155.2	1/5.07
Pump suction flow area	(m^2)	0.487	0.019	1/25.77
Pump suction length	(mm)	9750	7950	1/1

Table 2.1 (cont'd)

Component		PWR	JAERI	Ratio
Cold leg inside diameter	(mm)	698.5 (27.5")	155.2	1/4.50
Cold leg flow area	(m^2)	0.383	0.019	1/20.26
Cold leg length	(mm)	5600	5600	1/1
Steam generator simulator				
Number of tubes/loop	(—)	3388	158	1/21.44
Tube length (average)	(m)	20.5	15.2	1/1.35
Tube outside diameter	(mm)	22.225 (0.875")	25.4	
Tube inside diameter	(mm)	19.7 (0.05")	19.6	1/1
Tube wall thickness	(mm)	1.27	2.9	
Heat transfer area/loop	(m^3)	4784 (51500 ft^2)	192	1/24.92
Tube flow area/loop	(m^2)	1.03	0.048	1/21.44
Inlet plenum volume/loop	(m^3)	4.25	0.198	1/21.44
Outlet plenum volume/loop	(m^3)	4.25	0.198	1/21.44
Primary side volume/loop	(m^3)	30.50 (1077 ft^3)	1.2	1/25.4
Secondary side volume/loop	(m^3)	157.33 (5556 ft^3)	2.5	1/62.9
Containment tank 1	(m^3)		30	
Containment tank 2	(m^3)		50	
Storage tank	(m^3)		25	
Acc. tank	(m^3)		5	
Saturated water tank	(m^3)		3.5	

Table 2.2 Component elevations of Cylindrical Core Test Facility

COMPONENT		PWR	CCTF	DISCREPANCY
BOTTOM OF HEATED REGION IN CORE	(mm)	0	0	0
TOP OF HEATED REGION IN CORE	(mm)	3660	3660	0
TOP OF DOWNCOMER	(mm)	4849	4849	0
BOTTOM OF DOWNCOMER	(mm)	0	0	0
CENTERLINE OF COLD LEG	(mm)	5198	4927	-271
BOTTOM OF COLD LEG (INSIDE)	(mm)	4849	4849	0
CENTERLINE OF LOOP SEAL LOWER END	(mm)	2056	2047	- 9
BOTTOM OF LOOP SEAL LOWER END	(mm)	1662	1959	+297
CENTER OF HOT LEG	(mm)	5198	4927	-271
BOTTOM OF HOT LEG (INSIDE)	(mm)	4830	4849	+ 19
BOTTOM OF UPPER CORE PLATE	(mm)	3957	3957	0
TOP OF LOWER CORE PLATE	(mm)	- 108	- 50	+ 58
BOTTOM OF TUBE SHEET OF STEAM GENERATOR SIMULATOR	(mm)	7308	7307	- 1
LOWER END OF STEAM GENERATOR SIMULATOR PLENUM	(mm)	5713	5712	- 1
TOP OF TUBES OF STEAM GENERATOR SIMULATOR (avg)	(mm)	17952.7	14820	

Table 2.3 Instruments provided by USNRC

Instrument	Number of sets	Number of sensors
DC FDG	18	162
DC VOP	1	1
DC drag disk	4	4
Core velocimeter	4	4
Core impedance probe	12	24
Core LLD	6	96
LP LLD	3	15
End box turbine meter	8	8
UP turbine meter	4	4
UP FDG	11	110
UP film probe	2	4
UP prong probe	2	4
UP VOP	1	1
VV turbine meter	2	2
VV string probe	2	2
HL film probe	2	4
HL VOP	1	1
Reference probe	1	1
Spool piece	8	89
Total	92	536

Note :

DC : Downcomer, FDG: Fluid distribution grid,
VOP: Video optical probe, LLD: Liquid level detector,
LP : Lower plenum, UP : Upper plenum,
VV : Vent valve

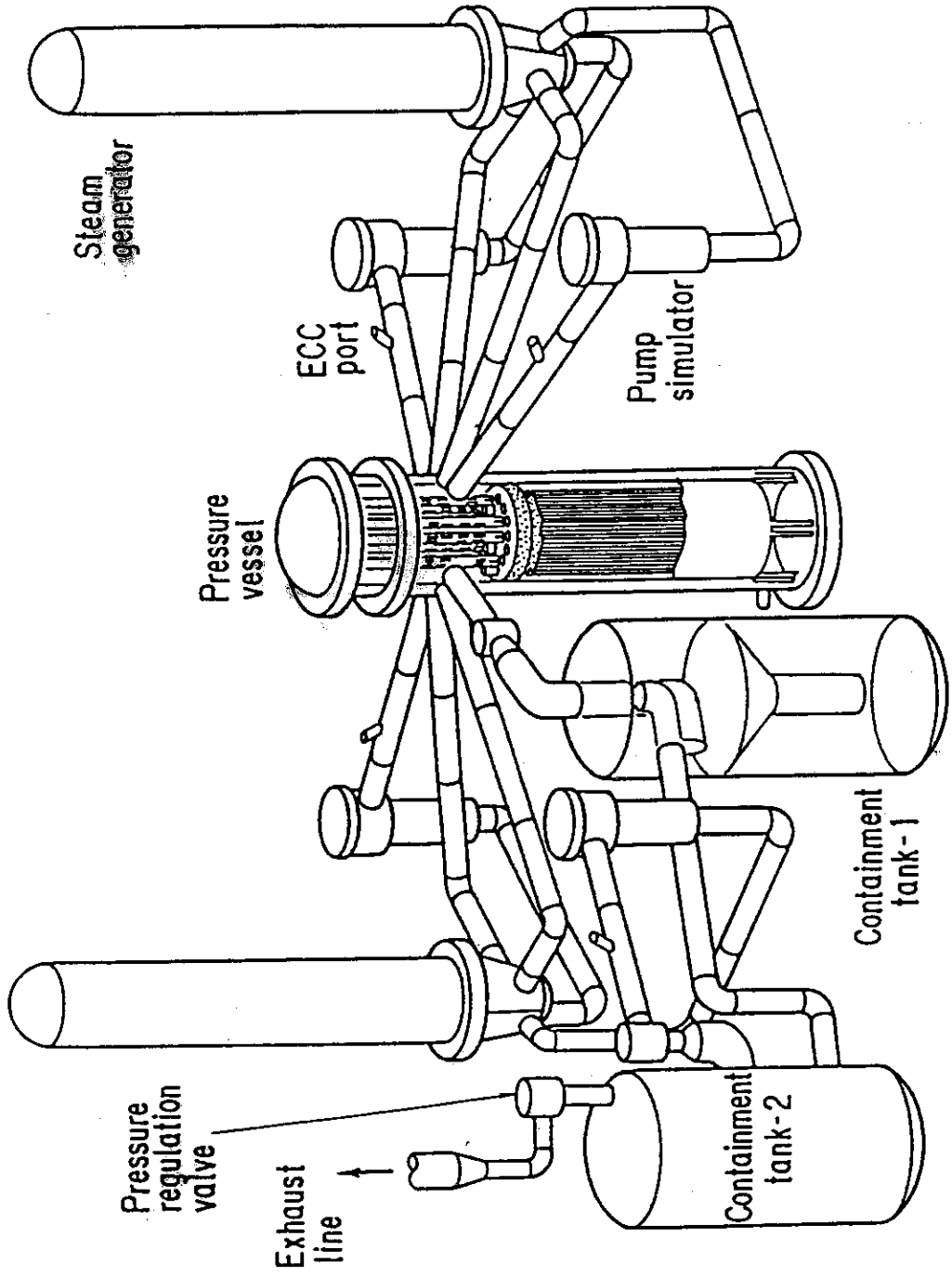

Fig. 2.1 Bird's-eye view of CCTF

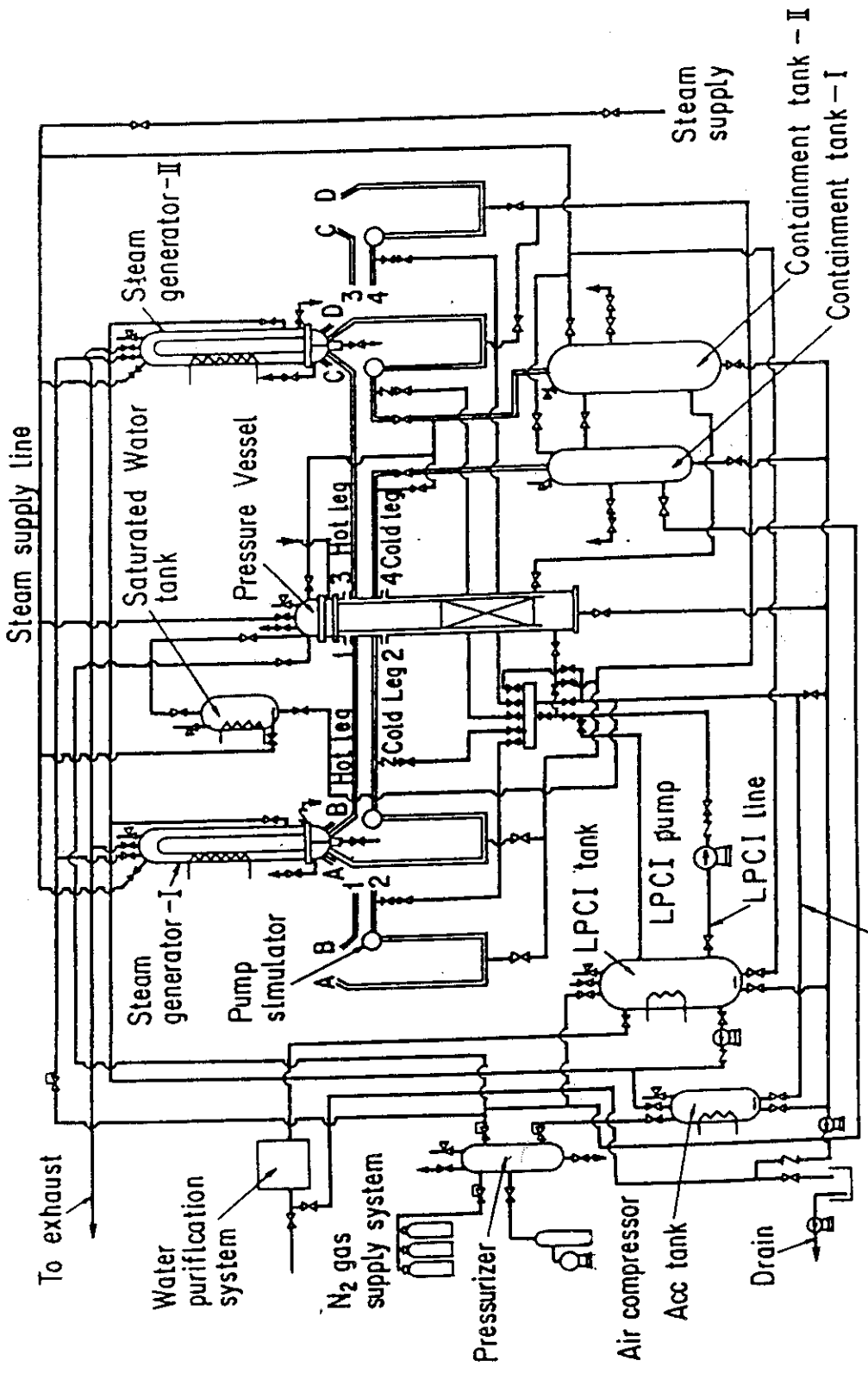

Fig. 2.2 Schematic diagram of CCTF

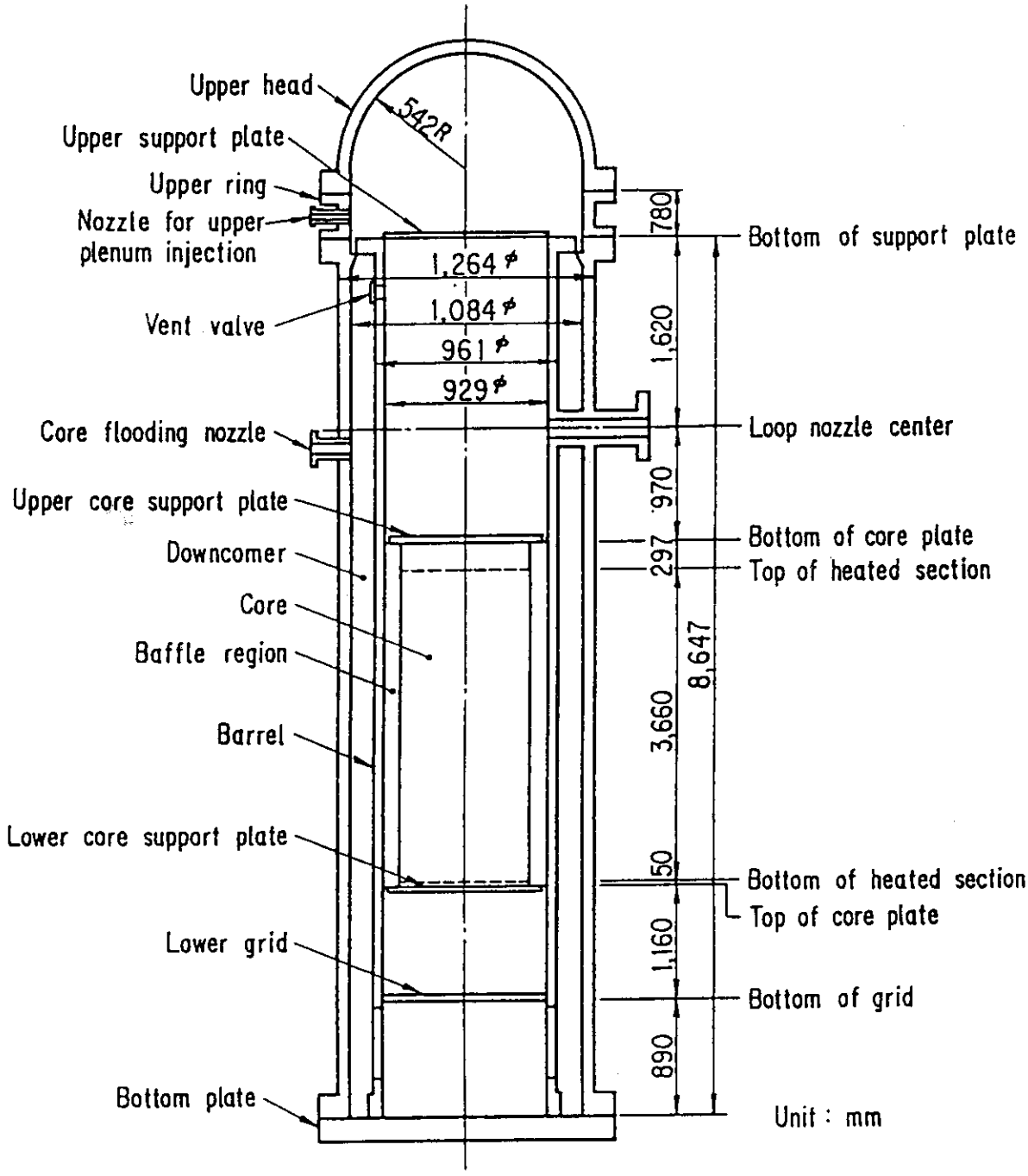

Fig. 2.3 CCTF Core-II pressure vessel

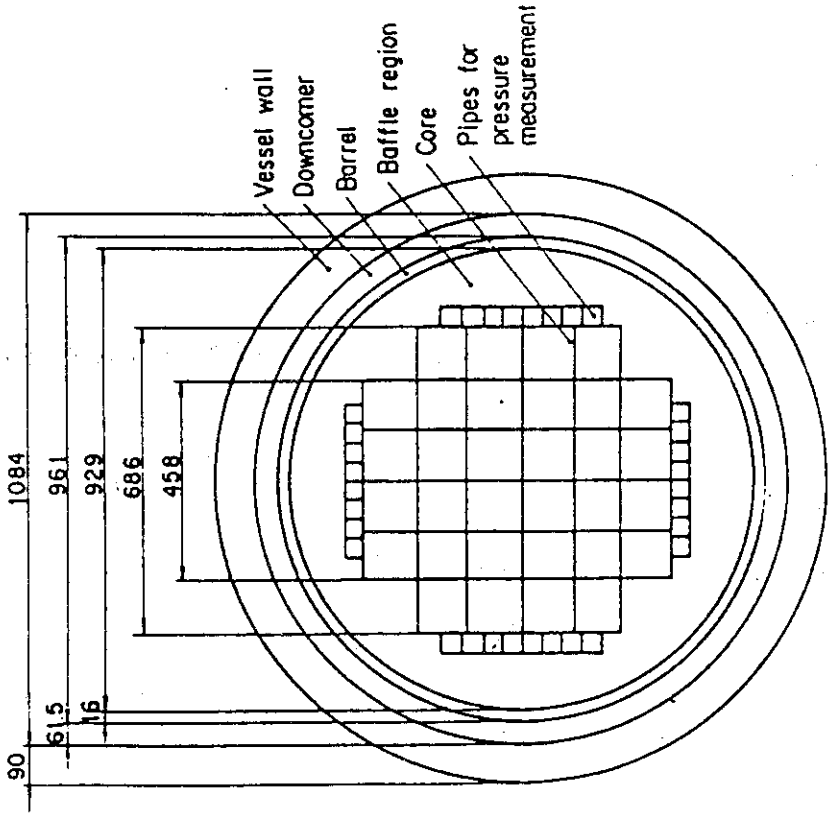

Fig. 2.5 Dimension of CCTF Core-II pressure vessel cross section

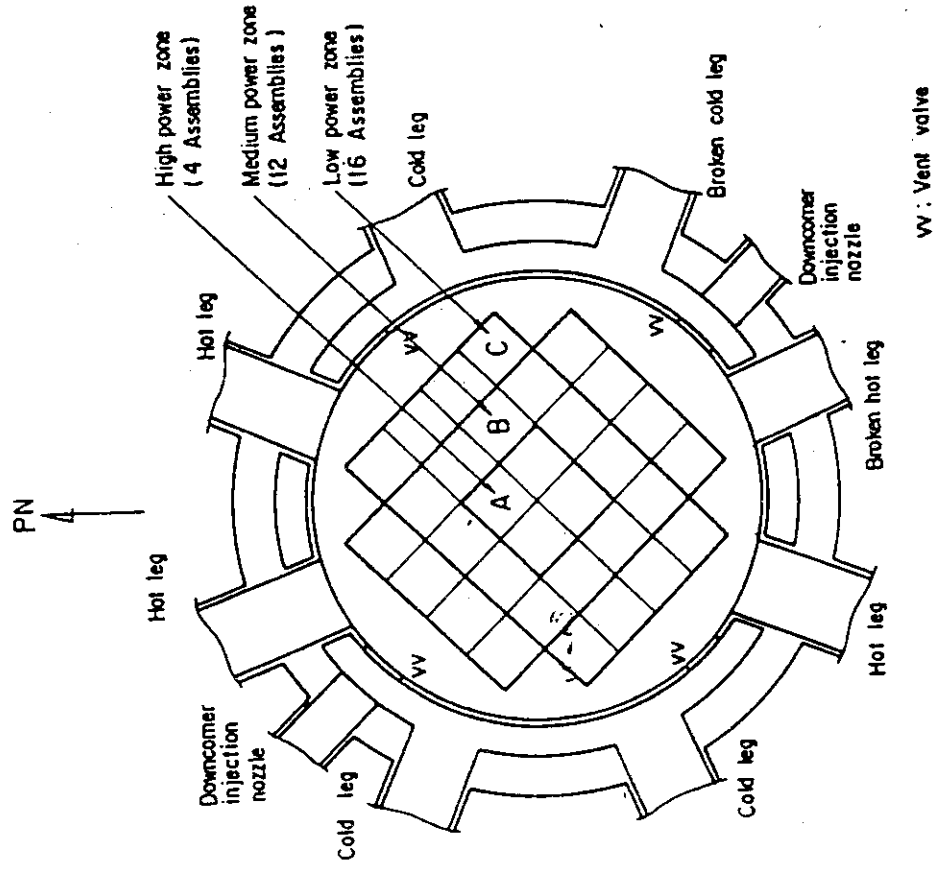

Fig. 2.4 Cross section of CCTF Core-II

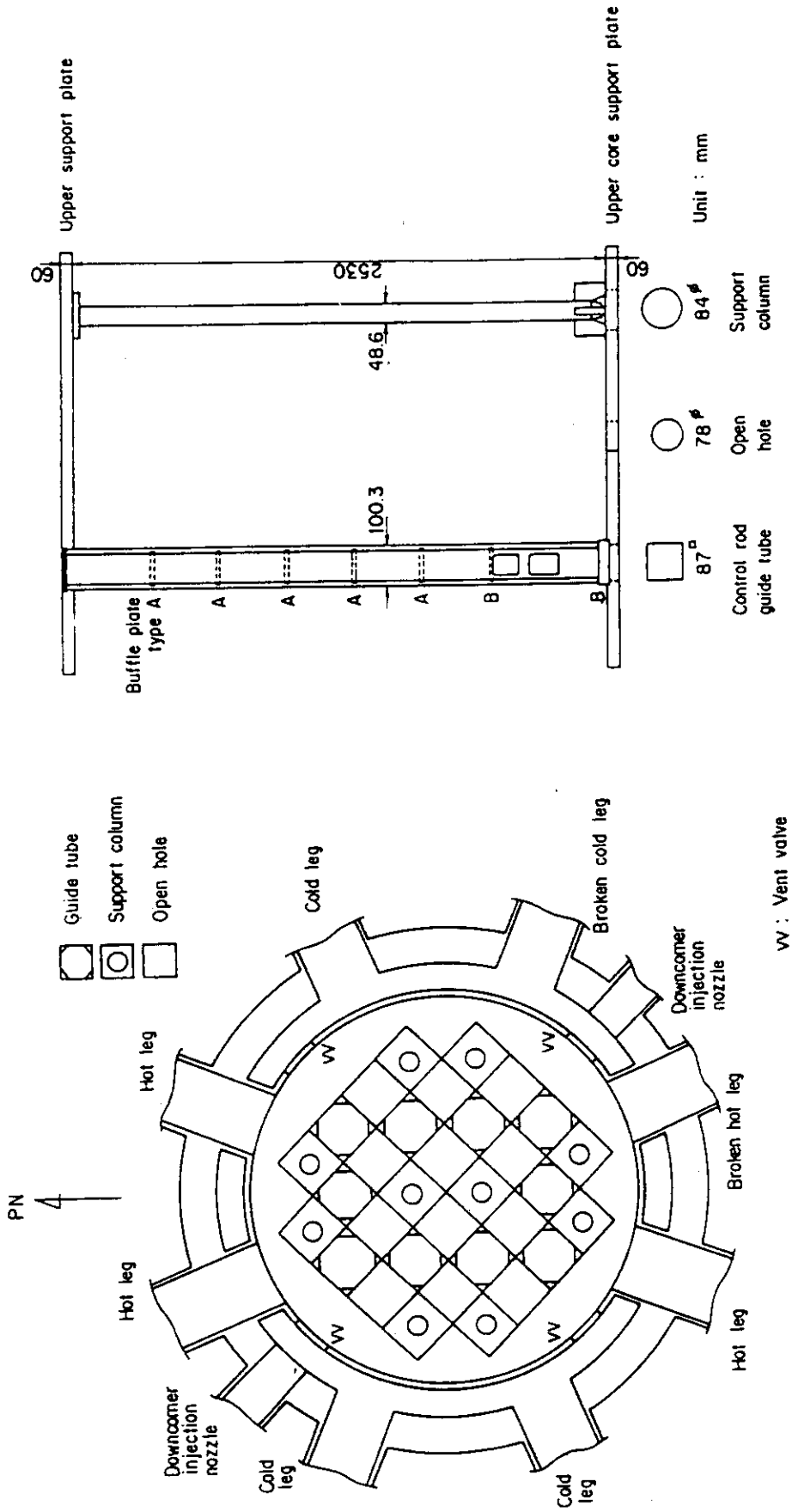

Fig. 2.6 Arrangement of upper plenum internals

Fig. 2.7 Upper plenum internals

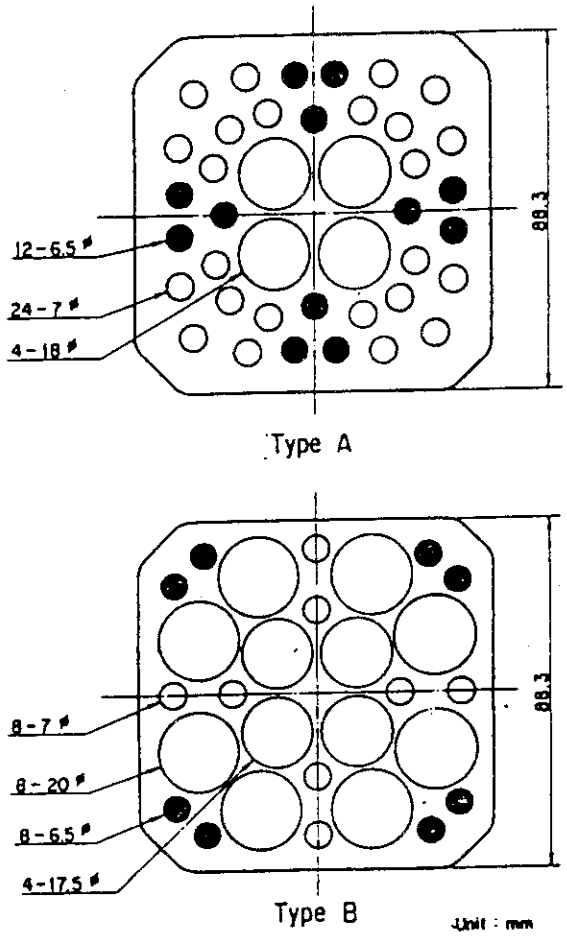

Fig. 2.8 Baffle plates in control rod guide tube

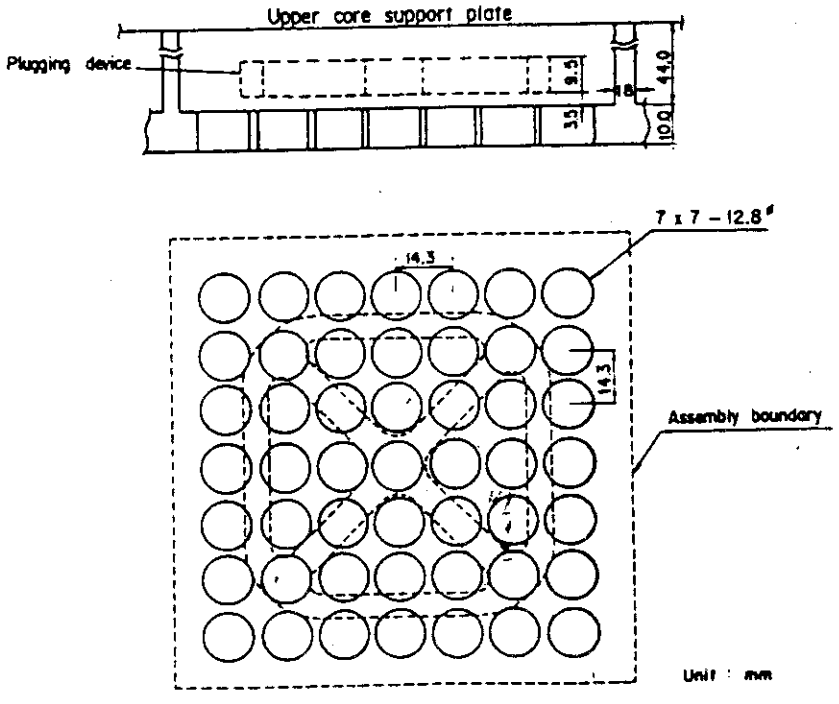

Fig. 2.9 Dimensions of holes of end box tie plate

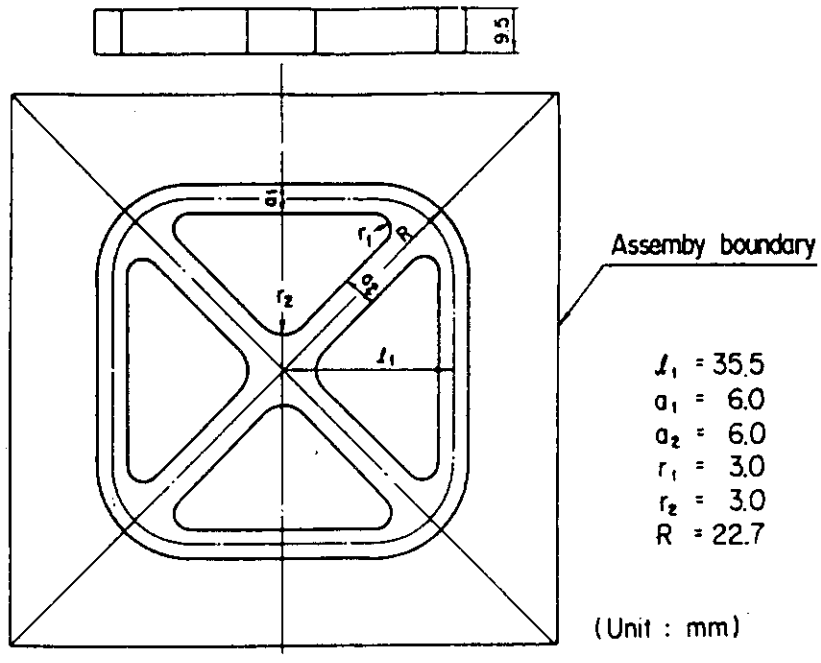

Fig. 2.10 Dimensions of plugging device

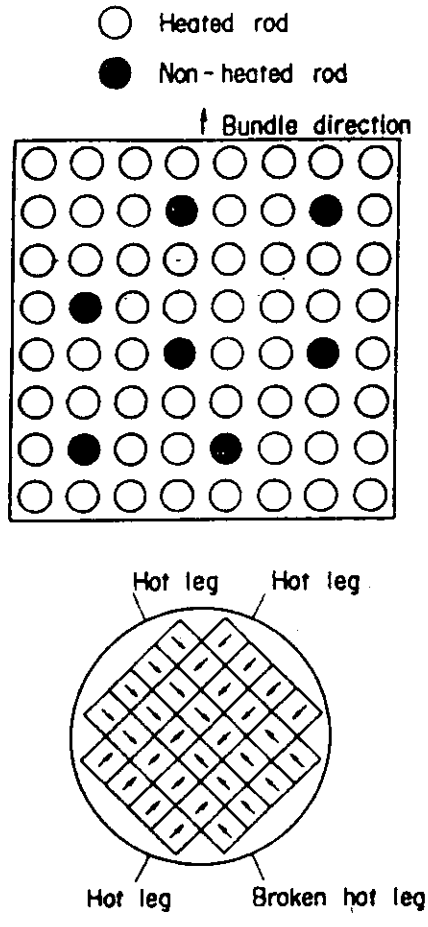

Fig. 2.11 Arrangement of non-heated rods bundle direction

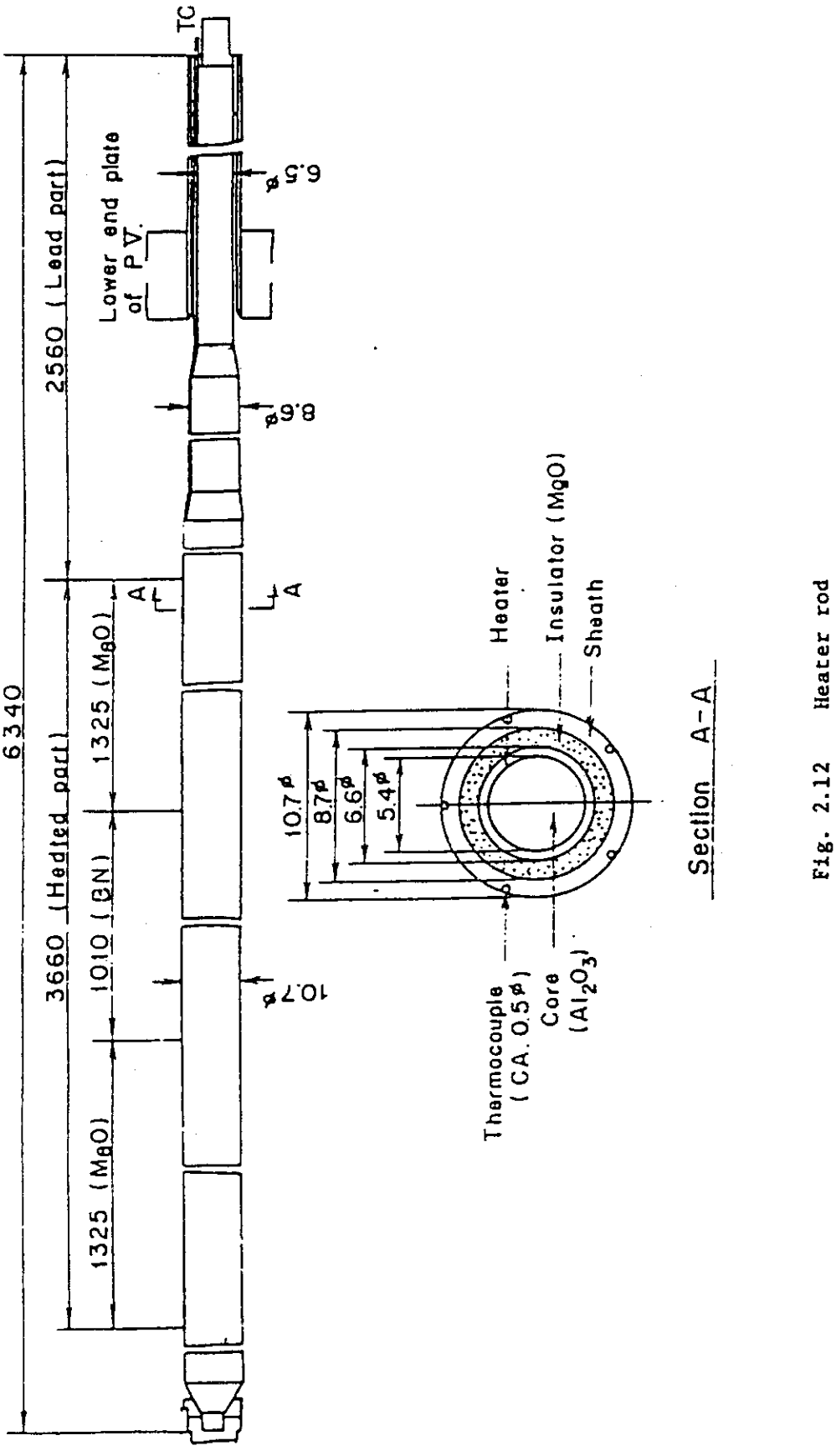

Fig. 2.12 Heater rod

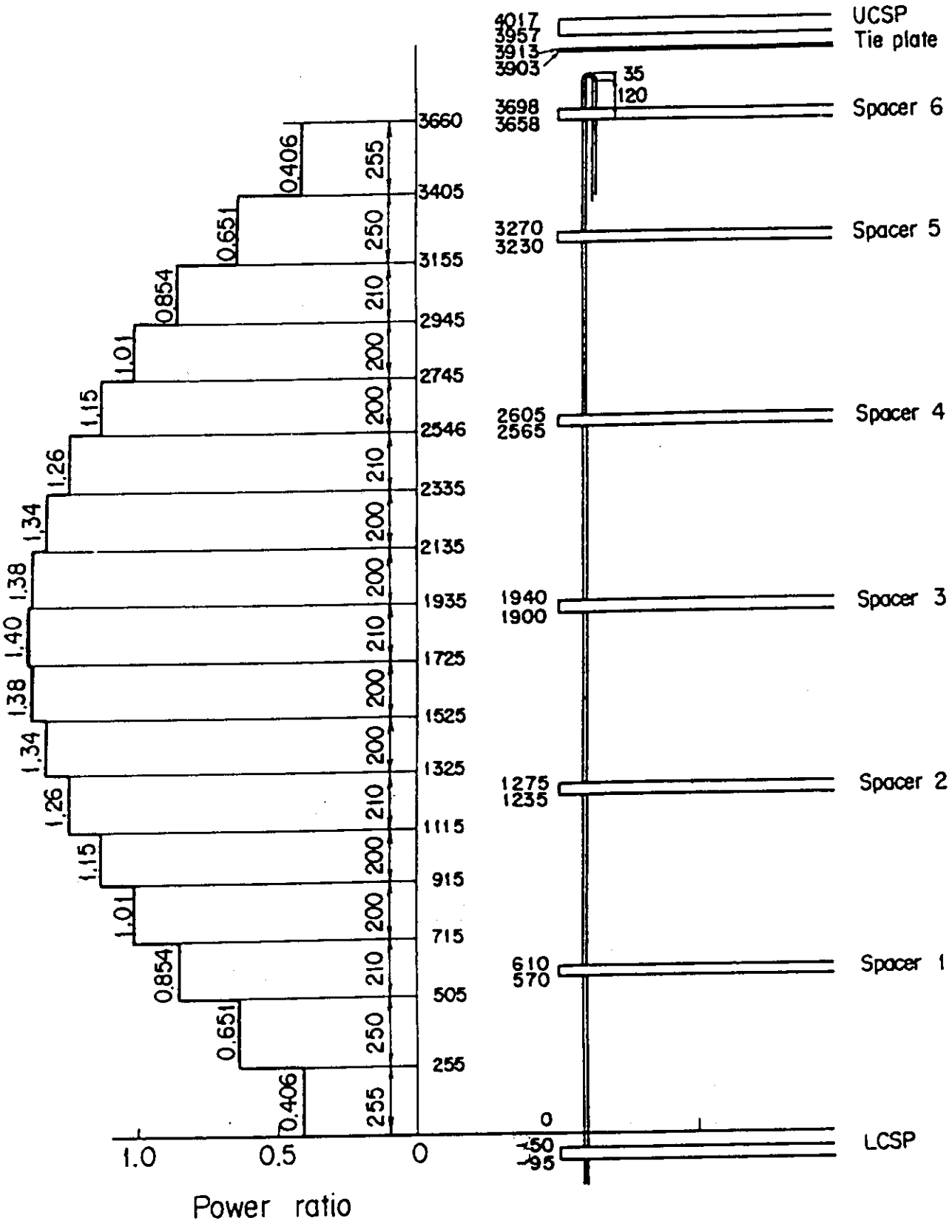

Fig. 2.13 Axial power profile of CCTF Core-II heater rod

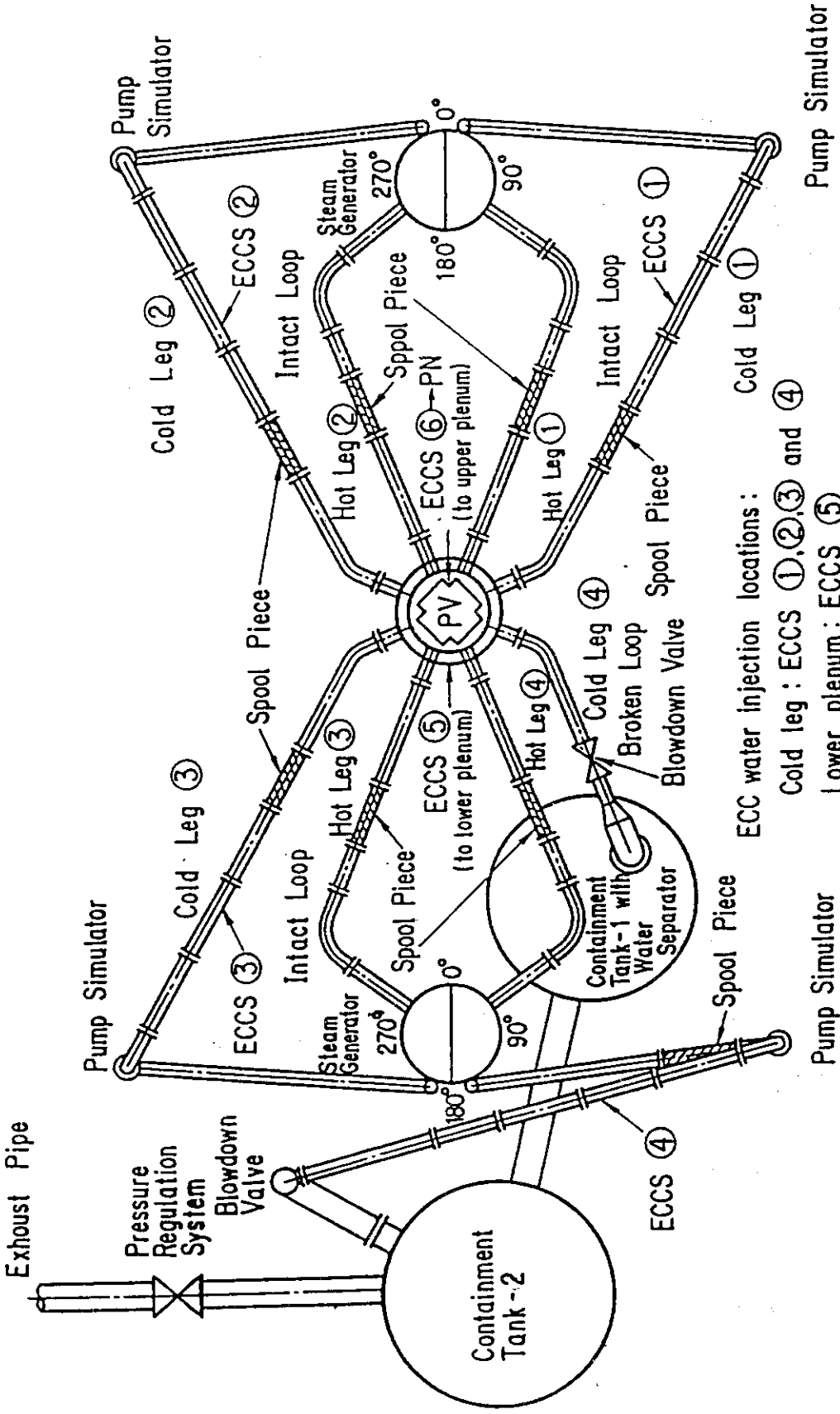

Fig. 2.14 Top view of primary loop pipings

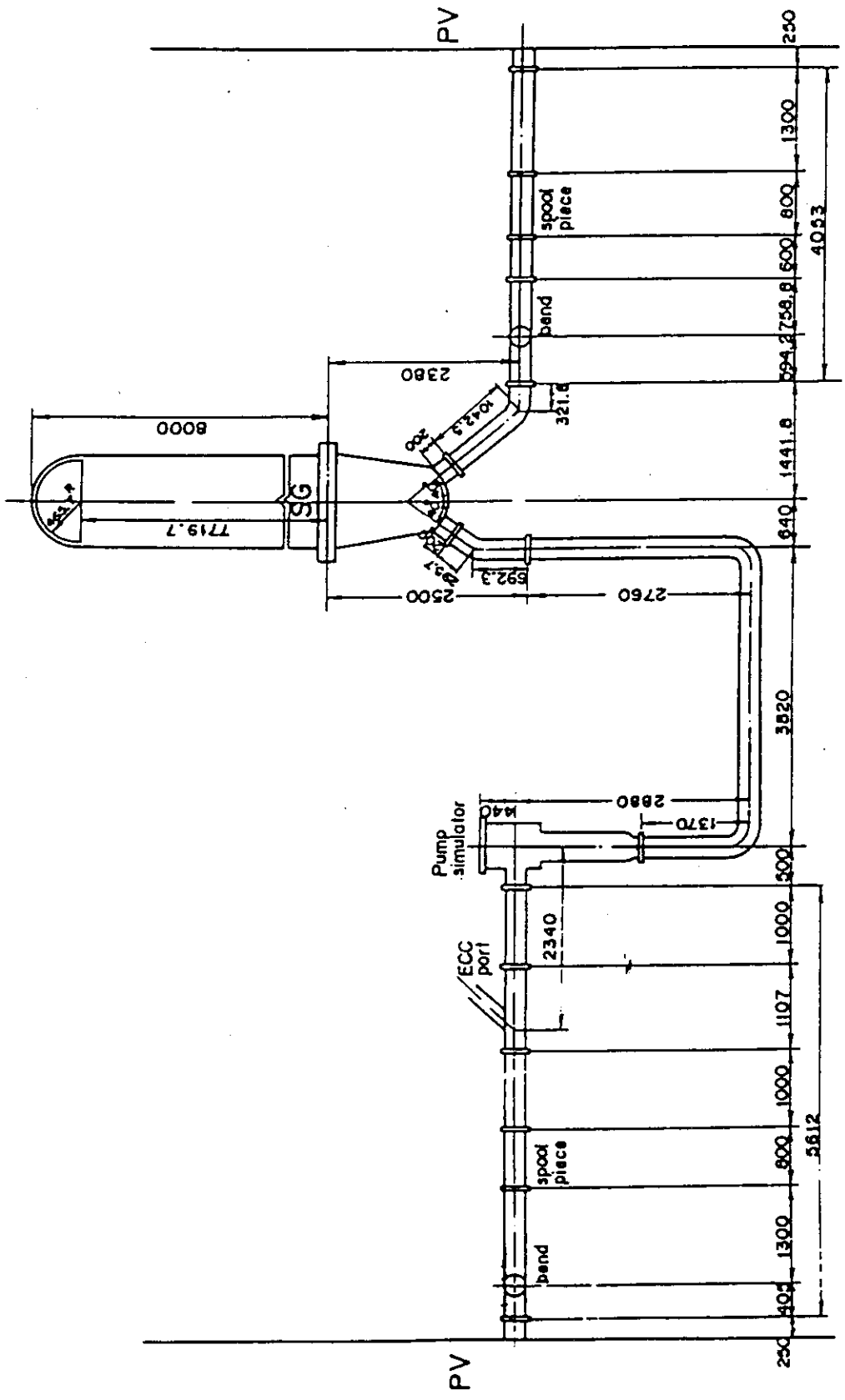

Fig. 2.15 Dimensions of primary loop

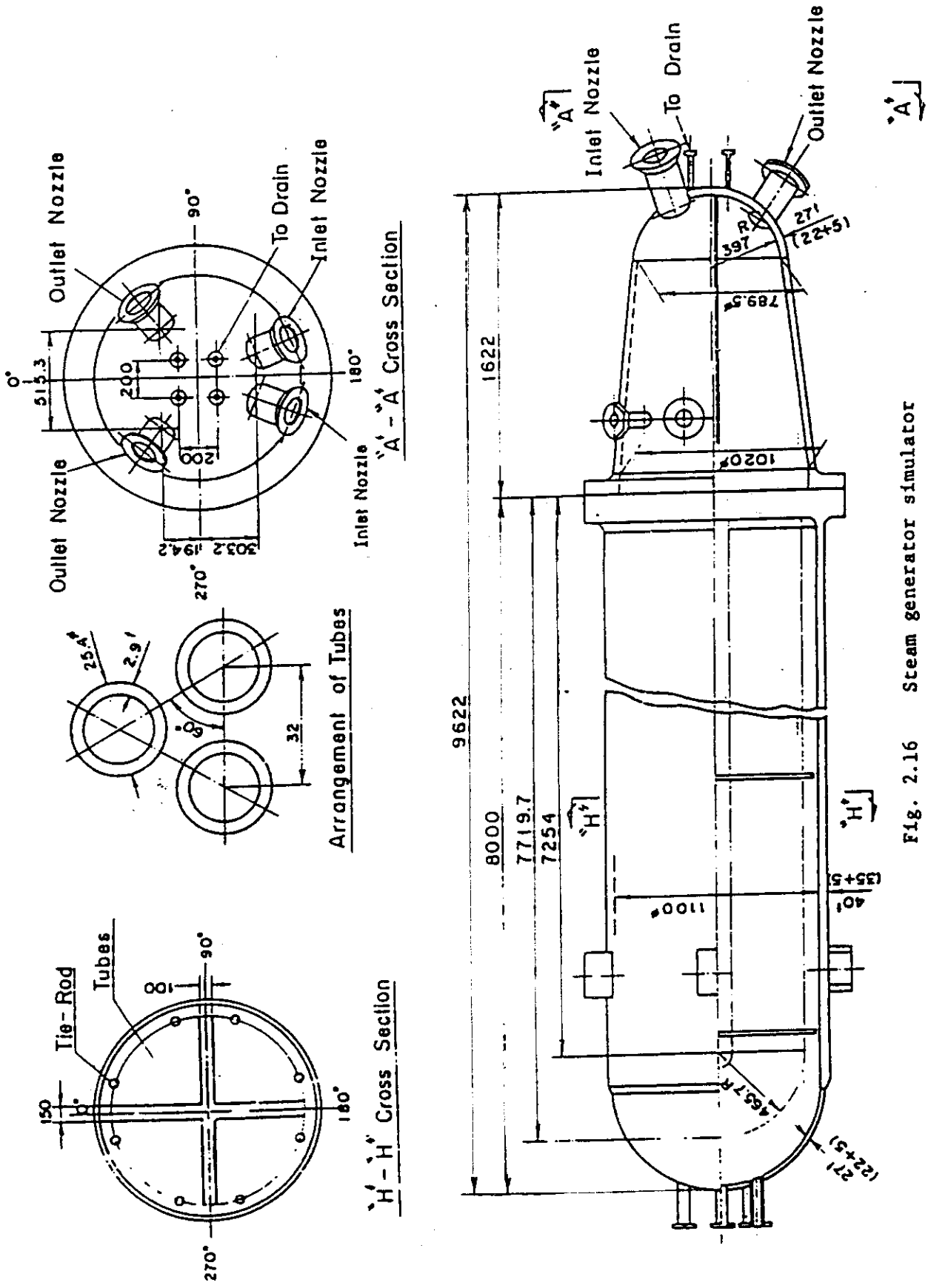

Fig. 2.16 Steam generator simulator

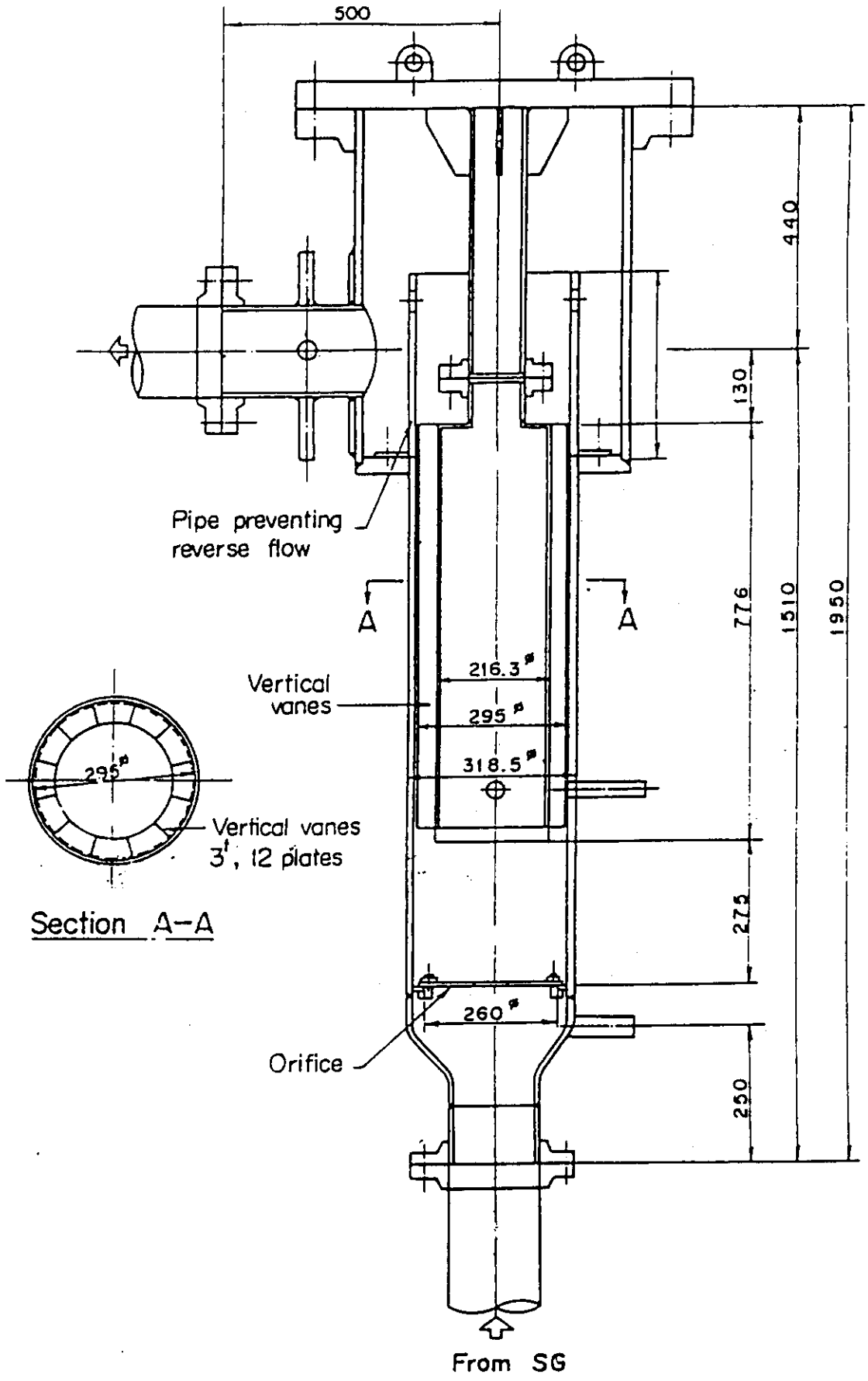

Fig. 2.17 Pump simulator

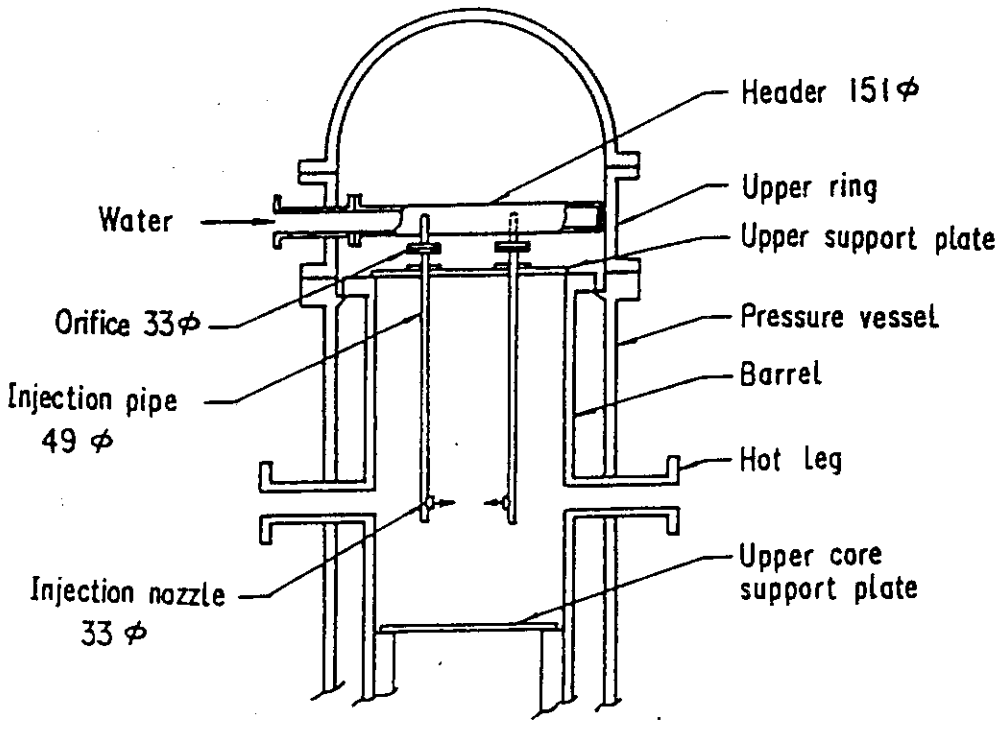

Fig. 2.18 Configuration of upper plenum injection pipe

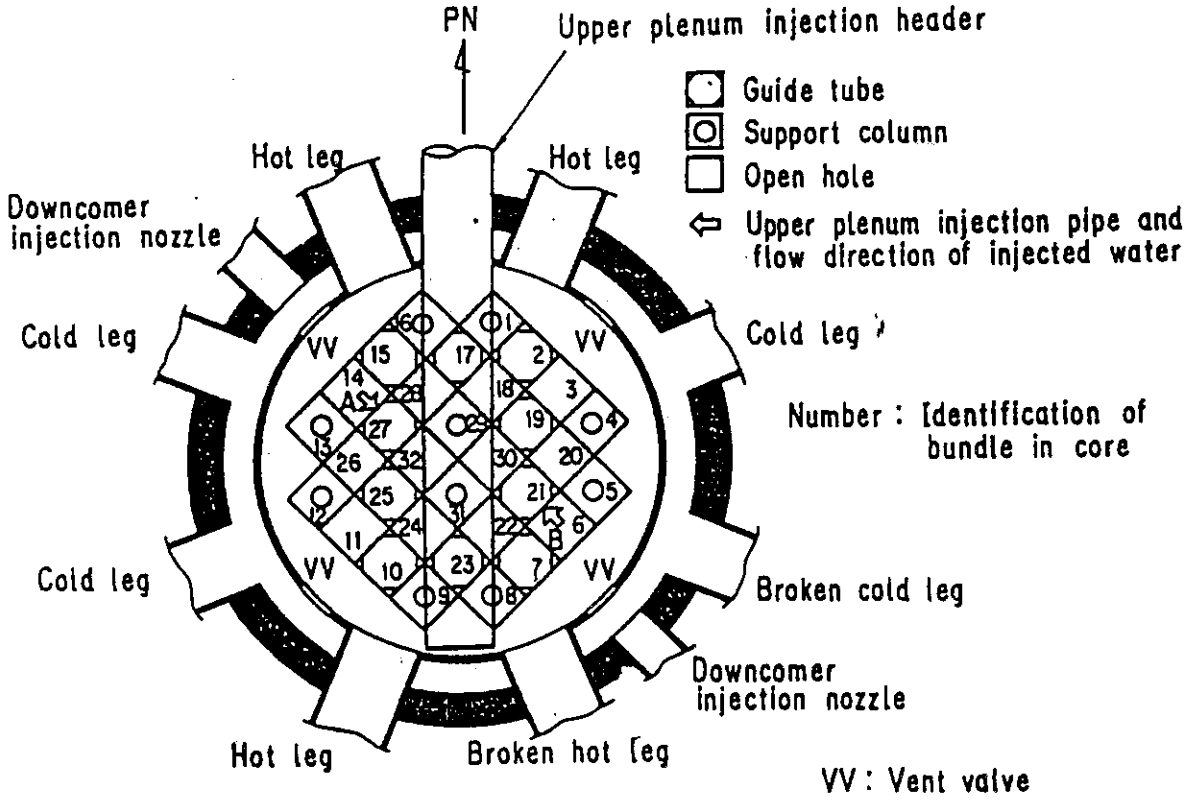

Fig. 2.19 Arrangement and location of upper plenum injection pipe

3. Measured test conditions and data presentation

3.1 Measured test conditions

When the flat radial power test was initiated(t= 0 s), the core was filled with the saturated steam at 0.2 MPa. The clad temperature of heater rods was about 393 K at t=0 s. The bottom of the pressure vessel was filled with saturated water to the specified level (0.87 m from the bottom of the pressure vessel). The initial downcomer wall temperature was 465 K. The wall of the primary piping was preheated to the saturation temperature before the test initiation. The water level in the secondary side of the steam generator 1 and 2 were 7.42 and 7.32 m at the test initiation, respectively. The water temperature in the secondary side of the steam generator was about 540 K.

Figure 3.1 shows the transient of the total power supplied to heater rods in the core. At 0 s, the power is turned on. At 4 s,it reaches 7.11 MW. The decay of the power starts at 120.5 s. The power follows the decay curve type of ANSx1.0+Actinide(40 s after scram). Table 3.1 shows initial average linear power in each power unit. The average linear power of all heater rods in the core is 1.065 kW/m. The maximum linear power is 1.070 kW/m of the power unit 9. The maximum linear power is 0.5 % higher than the whole core average. The minimum linear power is 1.052 kW/m of the power unit 6. The minimum linear power is 1.2 % lower than the whole core averarage. These results show that the flat radial power distribution was attained successfully in the CCTF test C2-6.

Figure 3.2 shows the pressure in the containment tank 2. The initial pressure is 0.2 MPa as planned. In this test, the pressure was controlled in the same way as in the CCTF test C2-5(Run 63), the steep radial power test. Figure 3.2 shows that the pressure control was performed successfully in the CCTF test C2-6.

Figure 3.3 shows the transients of the ECC water injection rates into the lower plenum and the three intact cold legs. Figure 3.4 shows the transients of the fluid temperatures at ECC water injection nozzles. The maximum clad surface temperature reached the specified level(871 K) at 113.5 s and the ECC water injection into the lower plenum was initiated. The injected water was accumulated in the lower plenum. At 122 s, the lower plenum was filled with water and the reflood of the heater rods started. At 126 s, the flow control valve in the lower plenum injection

line started to close and the ECC water injection into lower plenum was terminated at 129.5 s. The flow control valves in the cold-leg accumulator injection line started to open at 126 s. The injection location of ECC water was switched from the lower plenum to the intact cold legs. The injection rate into cold legs increased with time and reached the setting rate(0.0910 m3/s) at 130 s. The high injection rate simulates the accumulator injection in a PWR LOCA. At 138 s, the ECC water injection mode was switched to the LPCI mode. The ECC water injection from the accumulator tank was terminated at 141 s. The subcooled water(310 K) in the LPCI tank was pumped out to the intact cold legs by 1036 s.

Table 3.2 summarizes the measured test conditions with the planned test conditions. The chronology of events are summarized in Table 3.3.

3.2 Data presentation

The selected data from the CCTF test C2-6(Run 64) are presented in Figs. B-1 through B-28 in Appendix B. The Tag-ID of each measurement channel is shown on the upper right-hand corner of each figure. The definitions of Tag IDs are presented in appendix A.

3.3 Comparison of test conditions between the flat and steep radial power test

Table 3.4 shows comparisons of test conditions between the flat and steep radial power tests. As previously mentioned, in the flat radial power test, almost the flat radial power profile was attained in the radial direction. On the other hand, in the steep radial power test, the initial linear powers are 1.455, 1.275 and 0.812 kW/m in the central, intermidiate and peripheral regions, respectively. The ratios of the linear powers to the average linear power for the entire core are 1.364, 1.195 and 0.761, respectively. The linear power in the central region is 79 % higher than the power in the peripheral region. Although the radial power profile is different between these two tests, the average linear power for the entire core, that is the total power supplied to all heater rods in core, is almost the same.

Figure 3.5 shows the comparison of the initial clad surface temperature at the midplane of the heater rods. The initial clad surface temperature means the temperature at the reflood initiation. In the flat radial power test, the average temperature for all regions is 900 K. In the steep radial power test, the average temperatures for the central, intermidiate and peripheral regions are 805, 982 and 1046 K, respectively. The average temperature for all bundles are 901 K in the steep radial power test. The core pressure was 0.2 MPa(T_{sat}=393K) in both test. The average superheats of the heater rods are almost the same at the midplane.

Table 3.1 Initial average linear power in each power unit

Power unit number	Average linear power
1	1.063
2	1.065
3	1.068
4	1.067
5	1.062
6	1.052
7	1.064
8	1.069
9	1.070

Note: Average linear power of each power region

Peripheral region(power unit 1 through 4) --- 1.066 kW/m
Intermidiate region(power unit 7 through 9)-- 1.068 kW/m
Central region(power unit 5 and 6) -- 1.057 kW/m

Whole core average(power unit 1 through 9) -- 1.065 kW/m

Table 3.2 Initial conditions for flat radial power test

	Planned	Measured
Power		
Total (MW) :	7.12	7.11
Linear (kW/m) :	1.067	1.065
Radial power distribution(kW/m) :	1.067:1.067:1.067	1.057:1.068:1.066
Decay type : ANS x 1.0 + Actinide x 1.1 (40 s after scram)		
Pressure		
System (MPa) :	0.20	0.20
Steam generator secondary (MPa) :	5.20/5.20	5.25/5.27
Temperature		
Downcomer wall (K) :	471	465
Primary piping wall (K) :	393	394
Steam generator secondary (K) :	539/539	537/542
Peak clad at ECC initiation (K) :	871	879
Peak clad at reflood initiation (K) :	914	922
Lower plenum liquid (K) :	393	395
ECC liquid (K) :	308	310
Water level		
Lower plenum (m)	0.90	0.87
Steam generator secondary (m) :	7.4/7.4	7.42/7.32
ECC water injection rate		
Accumulator to lower plenum (m^3/s) :	0.1050	0.1054
Accumulator to cold legs (m^3/s) :	0.0892	0.0910
LPCI to cold legs (m^3/s) :	0.0111	0.0111

Table 3.3 Chronology of events for flat radial power test

Event	Time (s)
Test initiated (Heater power on) (Data recording initiated)	0.0
Accumulator injection to lower plenum initiated	113.5
Power decay initiated	120.5
Bottom of core recovery(BOCREC) (Reflood initiated)	122.0
Accumulator injection to cold legs initiated	126.0
Accumulator injection to lower plenum ended	129.0
LPCI injection to cold legs initiated	138.0
Accumulator injection to cold legs ended	141.0
All heater rods quenched	533.0
Power off	1036.0
LPCI injection to cold legs ended	1036.0
Test ended (Data recording ended)	1066.0

Table 3.4 Comparisons of test conditions between the flat and steep radial power tests

Item \ Test name	Flat radial power test	Steep radial power test
Initial linear power (entirecore average) (kW/m)	1.065	1.067
Decay curve type	ANSx1.0+Actinidex1.1 (40 s after scram)	ANSx1.0+Actinidex1.1 (40 s after scram)
Radial power profile (kW/m)	1.057:1.068:1.066	1.455:1.275:0.812
System Pressure (MPa)	0.20	0.20
Acc flow rate into cold legs (m^3)	0.0910	0.0892
LPCI flow rate into cold legs (m^3)	0.0111	0.0111

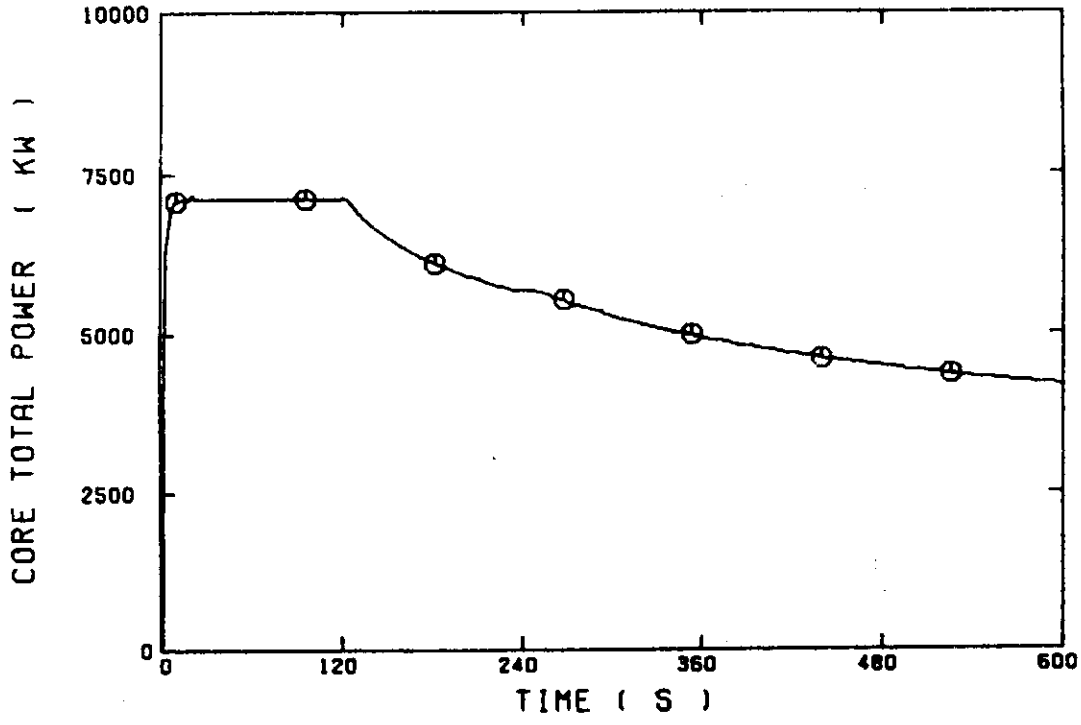

Fig. 3.1 Total power supplied to heater rods in core in the flat radial power test

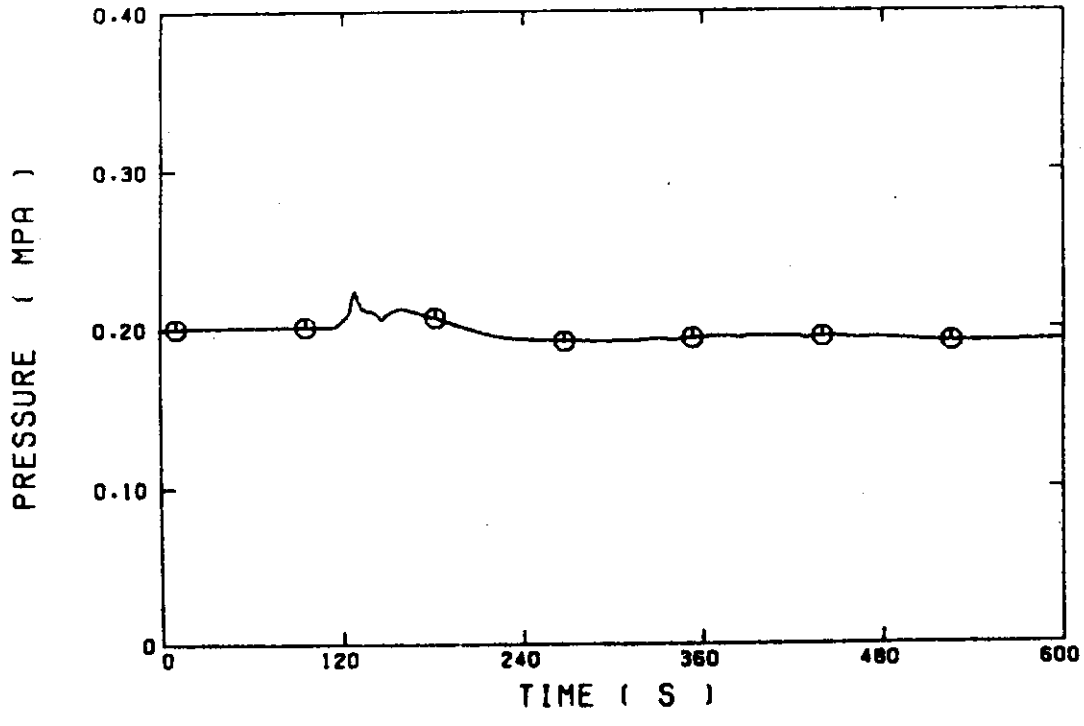

Fig. 3.2 Pressure in containment tank 2 in the flat radial power test

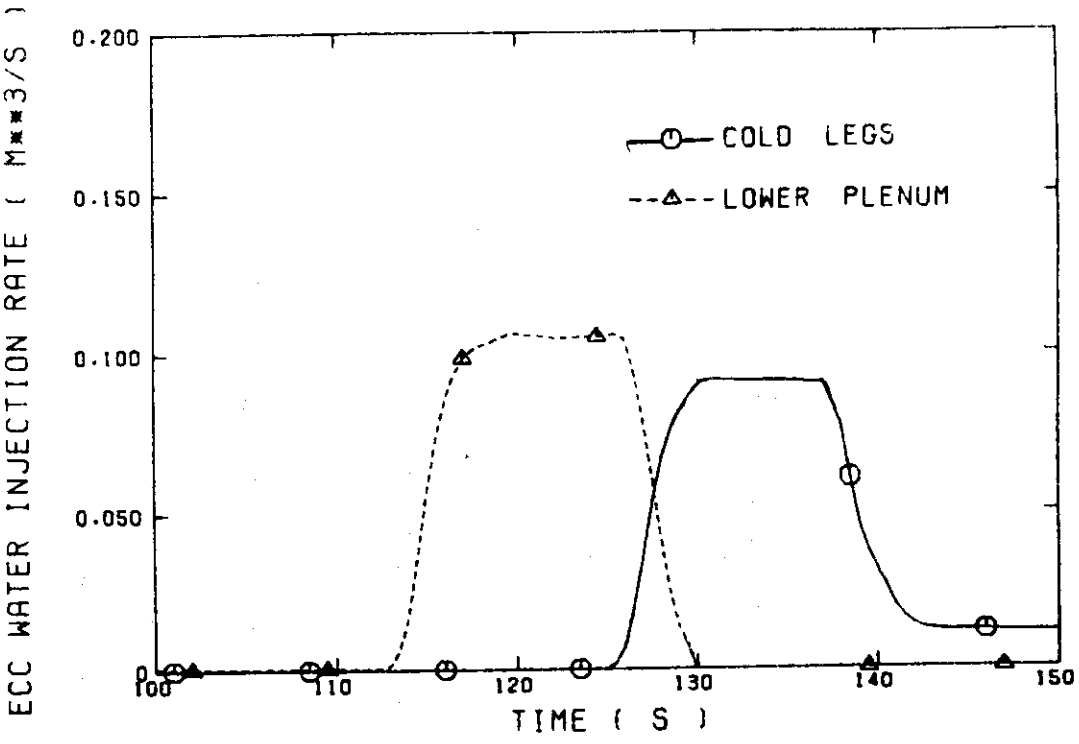

Fig.3.3 ECC water injection rates into lower plenum and three intact cold legs

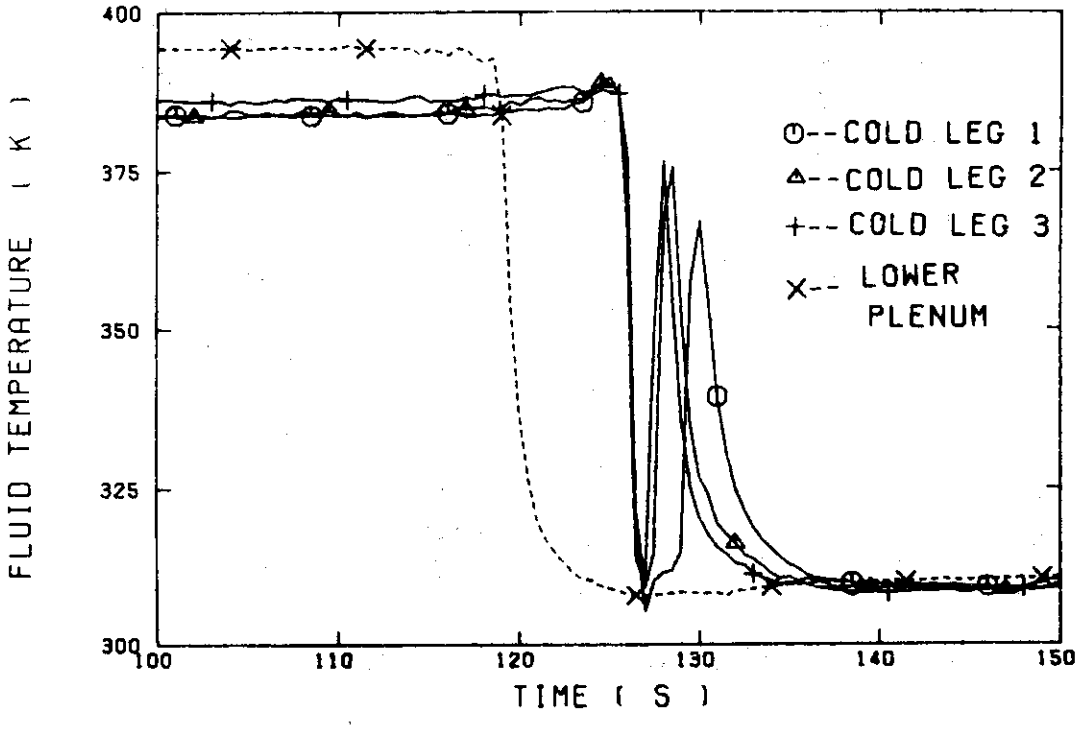

Fig.3.4 Fluid temperatures at ECC water injection nozzles in the flat radial power test

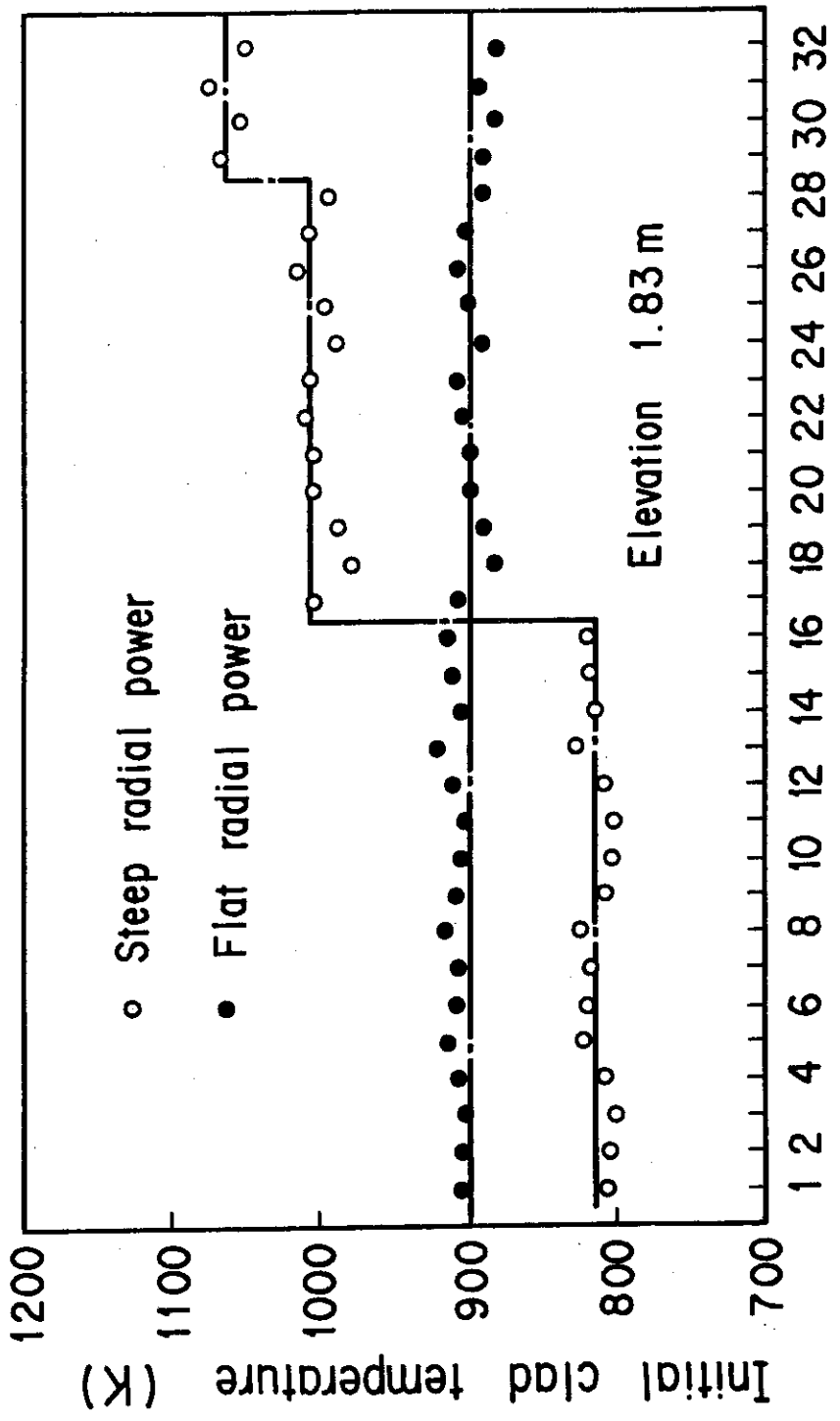

Fig. 3.5 Comparison of initial clad surface temperature at the midplane of heater rods between the flat and steep radial power tests

4. Results and discussion

In the safety analyses for the reflood phenomena of a PWR LOCA, the system composed of the primary loops and the one-dimensional single channel core represented by the average power rod is usually used in the system calculation and obtained are the boundary conditions for the analyses of the hot rod temperature responses, that is, the core inlet mass flow rate, the core inlet fluid temperature and the core inlet and outlet pressures. In this calculation procedure, it is assumed implicitly that the radial power profile in the core has no effect on the system behavior.

The core boundary conditions of the flat radial power test are equivalent to the assumption in the system calculation for the safety analyses of a PWR LOCA because the supplied power and the initial clad surface temperature profiles are flat radially and azimuthally. Thus, it is considered that the test results from the flat radial power test can represent the system behavior using one-dimensional core model. Through the comparisons of test results from the flat and steep radial power tests, it may be possible to identify how accurate the assumption of the one-dimensional core in the system calculation is.

4.1 Effect of radial power profile on system behavior

Figures 4.1 and 4.2 show the comparisons of the core inlet mass flow rate and the core inlet mass flow between the flat and steep radial power tests. The core inlet mass flow rate was estimated using the mass balance relation in the pressure vessel. The error of the mass flow rate was estimated to be within 15 %. The core inlet mass flow is the integration of the core inlet mass flow rate. It is equal to the total mass flow through the core inlet after the reflood initiation.

In the Acc mode(by 19 s), the core inlet mass flow rate is high due to the high ECC water injection rate and the weak steam binding effect. In the period, the core inlet mass flow rate is almost the same between two tests. In the LPCI mode(after 19 s), the core inlet mass flow rate is lowered in both tests. The time-averaged core inlet mass flow rates between 100 and 400 s are 4.41 and 4.25 kg/s in the steep and flat radial power tests, respectively. The rate in the steep radial power test is about 4 % higher than in the flat radial power test. The discrepancy is

only 1/4 of the estimation error of the core inlet mass flow rate. The radial power profile in the core has weak effect on the net flow through the core inlet.

Figures 4.3 and 4.4 show the comparisons of the core inlet subcooling and the core inlet pressure, respectively. The maximum subcoolings are 31 K at 67 s and 28 K at 80 s in the flat and steep radial power tests, respectively. After 100 s, the subcooling decreases with time in both tests. For the core inlet pressure, no significant discrepancy is observed between the tests as shown in Fig. 4.4. The radial power profile in the core has weak effect on the subcooling of the fluid and the pressure at the core inlet.

The core inlet mass flow rate can be related to the flow variables beside the core by the following equations:

$$m_{F,U}=m_{ECC/LP} + 3m_{ECC/CL} + 3m_I - m_{OL} - m_{OV} - m_{DC} - m_{LP}, \quad (1)$$

$$m_{F,D}=m_{CR} + m_{UP} + 3m_I + m_B. \quad (2)$$

where

$m_{F,U}$; Core inlet mass flow rate evaluated using data measured upstream of core inlet,

$m_{F,D}$; Core inlet mass flow rate evaluated using data measured downstream of core inlet,

$m_{ECC/LP}$; ECC injection rate into lower plenum,

$m_{ECC/CL}$; ECC injection rate into an intact loop,

m_I ; Mass flow rate through an intact loop,

m_B ; Mass flow rate through a broken loop,

m_{OL} ; Water mass flow rate through broken cold leg of PV side,

m_{OV} ; Steam mass flow rate through broken cold leg of PV side,

m_{DC} ; Water accumuration rate into downcomer,

m_{LP} ; Water accumuration rate into lower plenum,

m_{CR} ; Water accumuration rate into core,

m_{UP} ; Water accumuration rate into upper plenum.

Equations (1) and (2) show the possibility that the equal core inlet mass flow rate results from the compensation of all terms in the right-hand side of Eqs. (1) and (2). To make sure why almost the same core inlet mass flow rate was obtained regardless of the radial power profile, each term will be compared one by one.

Figure 4.5 shows the comparison of the mass flow rates through the

intact and broken loops, that is m_I and m_B. Figure 4.6 shows the comparison of the steam and water mass flow rates through the broken cold leg, that is m_{OV} and m_{OL}. These result show that the radial power profile has weak effect on the mass flow rate through each part. The water accumulation rates in the downcomer, the lower and upper plenums and the core were not measured directly in the CCTF tests. However, the integration of the rate can be evaluated using the measured differential pressure data because the pressure losses due to the friction and the acceleration are small compared to the static water head in each part. Figures 4.7 and 4.8 show the differntial pressures through the downcomer, the lower and upper plenums, and the core. No significant difference is observed in these differntial pressures between the tests. The core inlet mass flow rates became equal regardless of the radial power distribution because every term in Eqs. (1) and (2) was almost the same between the tests.

4.2 Effect of radial power profile on hydraulic behavior in core

Figures 4.9 through 4.14 show the comparisons of the differential pressure at various sections of the core. The differential pressures were measured at the periphery of the core at four azimuthal locations. Because the measured data showed good axisymmetry, the data from one azimuthal location are presented in these figures.

In the steep radial power test, some differential pressure measurements show significant zero shift at the beginning of the test. This is because some vertical conduits for the differntial pressure measurements were not filled with water. However, the vacant part of the conduit began to be filled with water after the reflood initiation. It is expected that the zero shift is caused by the vacant conduit for the differential pressure measurement. In the following, it is assumed that the reading of the differential pressure is accurate after 100 s because strangeous behavior of the curves disappeared by 100 s.

As shown in Figs. 4.9 through 4.14, the measured differential pressures are almost the same at all sections between both tests,even though the radial power profile is different each other. The results are consistent with the SCTF results[3]. It seems that the fluid mixing in the horizontal direction occured in the CCTF core as well as in the SCTF.

Figures 4.15 and 4.16 show the output from the turbine flowmeters

installed at the end box plate in the upper plenum. The Tag-IDs shown in these figures have a general form of NTXXNE1. XX indicates the bundle number just below each turbine flowmeter. Bundles 4, 8, and 16 belong to the peripheral region of the core. Bundle 28 belongs to the intermidiate region of the core. Bundles 29, 31 and 32 belong to the central region of the core. In the data acqusition of these turbine data, the calibration constants from single phase steam flow were used. Because water flows through the end box plate as well as steam, these data may be suspicious quantitavily.

The data from the steep radial power test show that the velocity is higher in the central region than that in the peripheral region. It may be supposed that this spatial distribution in the velocity is caused by the radial power profile in the core because the supplied power in the central region is 79 % higher than that in the peripheral region. However, this guess is incorrect because the same distribution of the velocity is observed even in the flat radial power test. It is considered that the spatial distribution of the velocity at the end box plate is attributed to the configuration of the CCTF rather than to the spatial distrition of the power in the core. It is necessary to study more the data acqusition of the turbine flowmeter in the two-phase flow.

4.3 Effect on thermal behavior

4.3.1 Estimation of heat capacity of heater rods from results in the flat radial power test

In order to evaluate the scattering of the clad surface temperature data, the temperature rise in the heat-up period was analyzed.

When the flat radial power test was initiated(t=0 s), the core was filled with the saturated steam at 0.2 MPa. The surface temperatures of heater rods were about 393 K at the time. Figure 4.17 shows the axial profile of the clad surface temperature at the reflood initiation(t= 122 s). The experimental data indicate the spatial average for each elevation. The bar with data shows the standard deviation of the averaged data. The number of data used in the averaging procedure is summarized in Table 4.1. The temperature rise in the heat-up period($0<t<122$ s), dT_i can be evaluated by

$$dT_i=(q_H t_H)/C_n \qquad (3)$$

where

C:Heat capacity of heater rods per unit length (J/mK),
q_H:Linear power (kW/m),
t_H:Duration time of the heat-up period (s),
n:Section number of heater power step.

The stepwise curve in Fig. 4.17 shows the calculated clad surface temperature with Eq. (3) assuming that the heat capacities are 347 and 360 J/mK for the BN and MgO sections, respectively. The BN section covers the elevation between 1.325 and 2.335 m from the bottom of the core heated section. The MgO section covers the elevation between 0 and 1.325 m or between 2.335 and 3.66 m. The calculated profile agrees with the measured profile within an error of 40 K.

Figure 4.18 shows the initial clad surface temperature at the elevation of 1.83 m in each bundle. The definition of the bundle and the power-unit numbers in CCTF-II are shown in Fig. 4.19. The average clad surface temperature is 899.6 K at the elevation and all initial clad surface temperatures scatter between 879.6 and 919.6 K. The solid lines show the calculated initial clad surface temperatures with Eq. (3) using the measured linear power of each power-unit and the heat capacity of 347 J/mK. The estimation confirms that the temperature scatter caused by the variation of the supplied power is less than 6 K. The broken lines show the calculated initial clad surface temperature with Eq. (3) assuming +3 % or -3% variation of the heat capacity of the heater rods. The 3 % variation of the heat capacity explains the 15 K variation in the initial clad surface temperatures. The result suggests that the heat capacity of the heater rods is within a variation of 3 % at the midplane of the heater rods at most.

4.3.2 Comparisons of heat transfer coefficient

Figures 4.20 and 4.21 show the comparisons of the averaged clad surface temperatures at the midplane of the heater rods in the central and peripheral regions, respectively. The clad surface temperatures are the arithmetic averages of the data from bundles 1 through 16 for the

peripheral region and from bundles 29 through 32 for the central region, respectively. In the peripheral region, the temperature in the flat radial power test is higher than that in the steep radial power test because of the higher local power. On the other hand, in the central region, the temperature in the flat radial power test is lower than that in the steep radial power test due to the lower local power.

Figures 4.22 and 4.23 show the comparisons of the averaged heat transfer coefficients in the central and peripheral regions, respectively. The heat transfer coefficient in the steep radial power test is higher in the central region and lower in the peripheral region than those in the flat radial power test. The result shows that the heat transfer in core is enhanced in the higher power (central) region and lowered in the lower power (peripheral) region of the steep radial power test. The tendency is consistent with the results in the SCTF tests[3].

Figure 4.24 shows the averaged heat transfer coefficient at the midplane in the central, intermidiate and peripheral regions from the flat radial power test. Figure 4.25 shows the heat transfer coefficients from the steep radial power test. In the flat radial power test, the heat transfer coefficient in the central region is slightly higher than that in the peripheral region between 20 and 150 s. The core heat transfer is not necessarily uniform even in the flat radial power test. It may be supposed that the difference of the heat transfer coefficient is attributed to the variation of the heat capacity of the heater rods. However, the calculation results with REFLA code showed that the 3 % variation of the heat capacity resulted in much small variation of the heat transfer coefficient than that observed in the test. The difference of the heat transfer coefficient may be attributed to the wall effect in the periphery of the core and/or the nonuniform condition at the boundary between the core and the upper plenum as shown in Fig. 4.16.

Even though some slight multidimensional effect was observed even in the flat radial power test, more clear difference is observed in the steep radial power test as shown in Fig. 4.23. The difference should be caused by the radial power profile itself and/or the profile of the clad surface temperature in a horizontal cross section.

Murao and Sugimoto developed a correlation for the heat transfer coefficient during the reflood phase, given by[5]

$$h=0.94(k_g^3\rho_g\rho_l h_{fg}g/L_q\mu_g\Delta T_{sat})^{1/4}(1-f_g)^{1/4} \quad (4)$$
$$+Ee(1-f_g)^{1/2}(T_w^4-T_{sat}^4)/\Delta T_{sat}$$

where

h;Heat transfer coefficient,

k;Themal conductivity,

ρ;Density,

h_{fg};Latent heat for evaporation,

f_g;Void fraction,

g;Acceleration of gravity, or suffix for gas phase,

l;Suffix for liquid phase,

L_q;Distance from quench front,

μ;Viscosity,

ΔT_{sat};Wall superheat,

E;Stefan-Boltzman constant,

e;Emmisivity,

T_w;Wall temperature,

T_{sat};Saturation temperature.

The first and second terms in the right hand side represent the heat transfer due to the film boiling and the radiation, respectively. To assess the effects of the different clad surface temperature and distance from the quench front, the correlation was applied to the CCTF result. In the estimation, it is assumed that the void fraction is uniform in a horizontal cross section based on the results in the previous CCTF tests[2]. The used test results for the calculation of the heat transfer coefficient were the wall and fluid temperatures, and the distance from the quench front. The effect of the different clad surface temperature and local power are considered through the differences in T_{sat}, physical properties of steam and the distance from the quench front.

Figures 4.26 and 4.27 show the comparisons of the heat transfer coefficients between the test and estimated results for the central and peripheral regions, respectively. The estimated results are lower in the central region and higher in the peripheral region than the test results.

Table 4.2 summarizes the estimated results at 100 s in the steep radial power test. The correlation gives lower heat transfer coefficient as the local power is increased. This means that the estimation using Eq. (4) with the assumption of uniform void fraction in a horizontal cross section does not explain the dependency of the heat transfer coefficient

on the power descrepancy in the wide core. There must be some error in the assumption of the uniform void fraction and/or the equation (4) to explain the observed tendency of the heat transfer coefficient. It is necessary to study more the dependency of core heat transfer on the radial power profile in wide core.

Table 4.1 Number of measuring location used in the data averaging for the initial clad surface temperature

Elevation (m)	Central region Bundle numbers 29 through 32	Intermidiate region Bundle numbers 17 through 28	Peripheral region Bundle numbers 1 through 16
0.128	4	12	16
0.380	8	24	32
0.815	4	12	16
1.015	8	24	32
1.425	4	12	16
1.830	8	24	32
2.035	4	12	16
2.440	8	24	32
2.845	1	1	3
3.050	9	25	35
3.340	1	1	3
3.560	5	13	19

Table 4.2 Comparisons of heat transfer coefficient between CCTF results and the estimation with Eq. (4)

Power region	High power region	Medium power region	Low power region
CCTF result (W/m^2K)	131.0	114.0	83.0
Estimation with Eq. (4) (W/m^2s)	82.3	83.9	84.7
First term in Eq. (4) (W/m^2s)	66.6	68.7	75.1
Second term in Eq. (4) (W/m^2s)	15.8	15.2	9.6
L_q (m)	0.865	0.763	0.572
ΔT_{sat} (K)	591.7	577.7	409.0

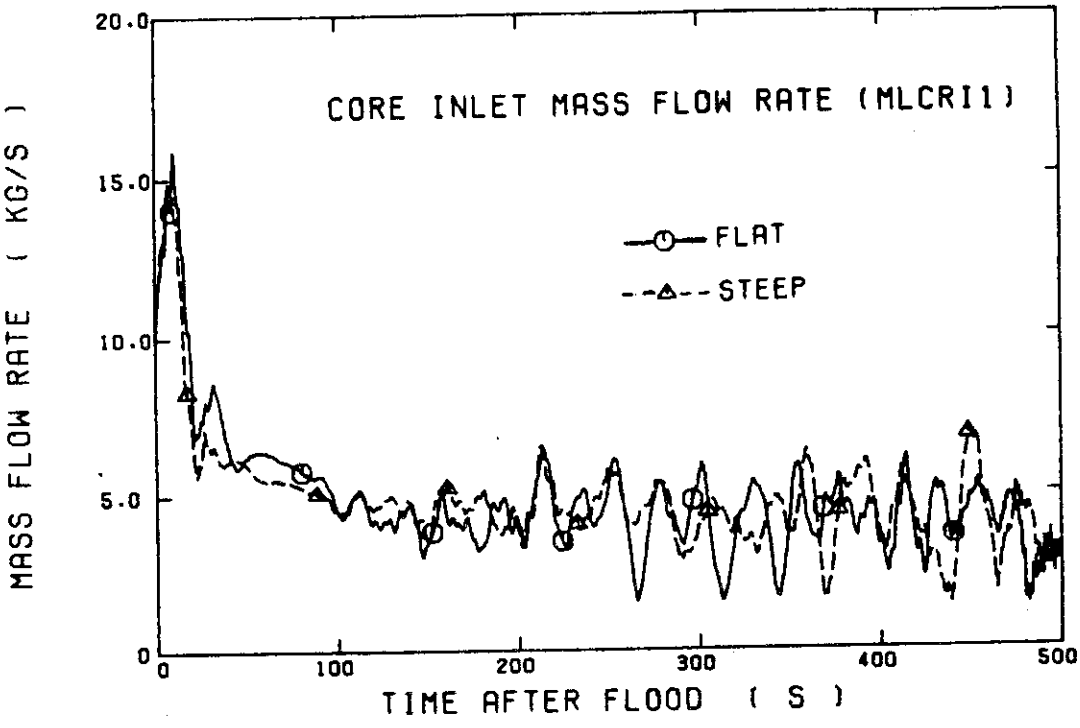

Fig. 4.1 Comparison of core inlet mass flow rate between the flat and steep radial power tests

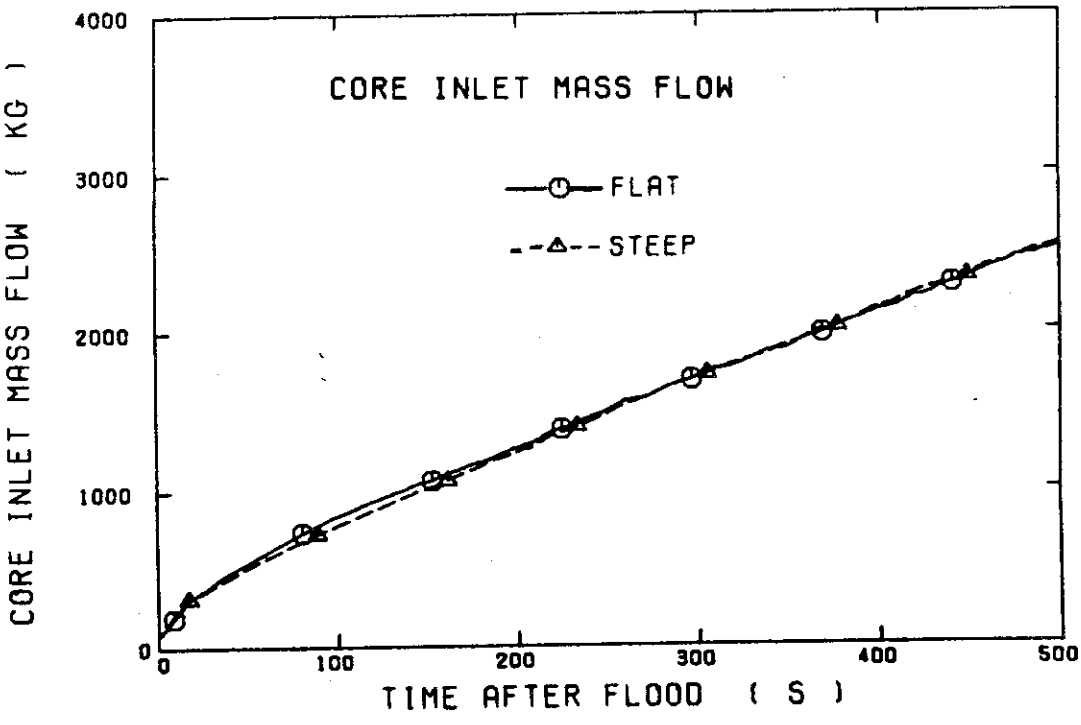

Fig. 4.2 Comparison of core inlet mass flow between the flat and steep radial power tests

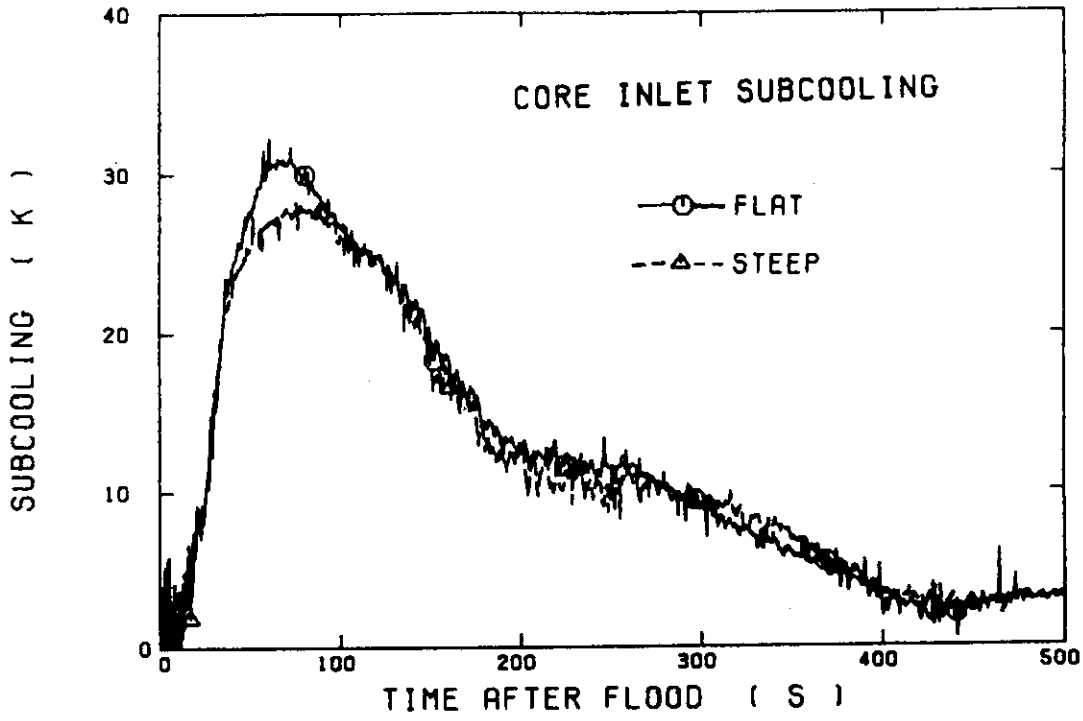

Fig. 4.3 Comparison of core inlet subcooling between the flat and steep radial power tests

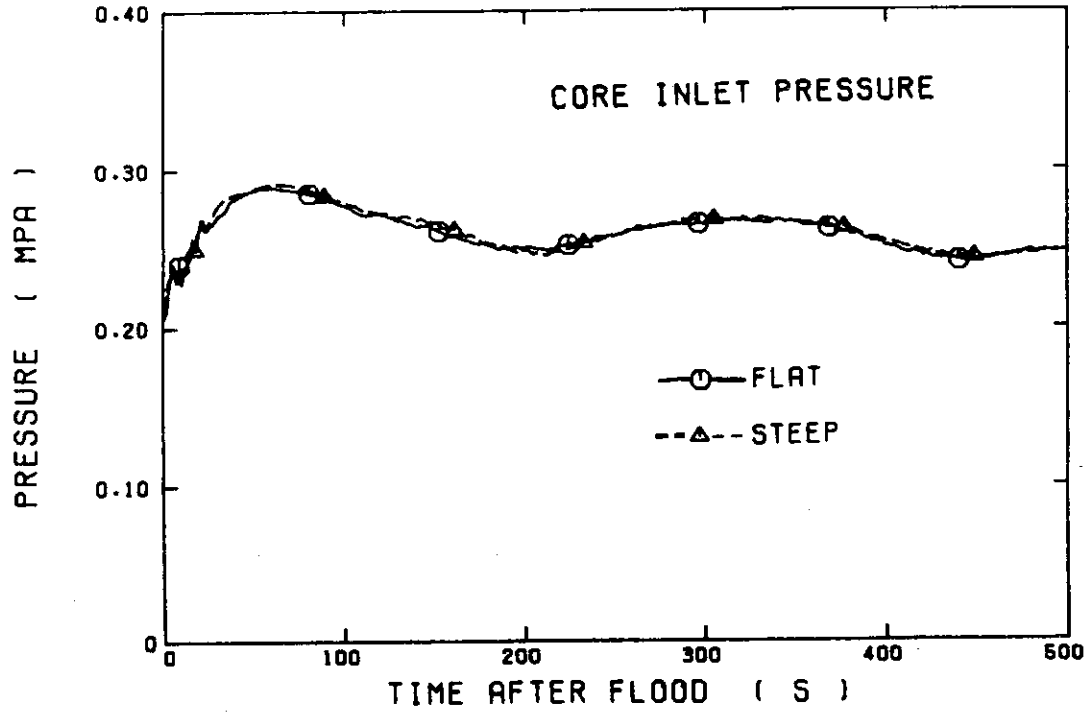

Fig. 4.4 Comparison of core inlet pressure between the flat and steep radial power tests

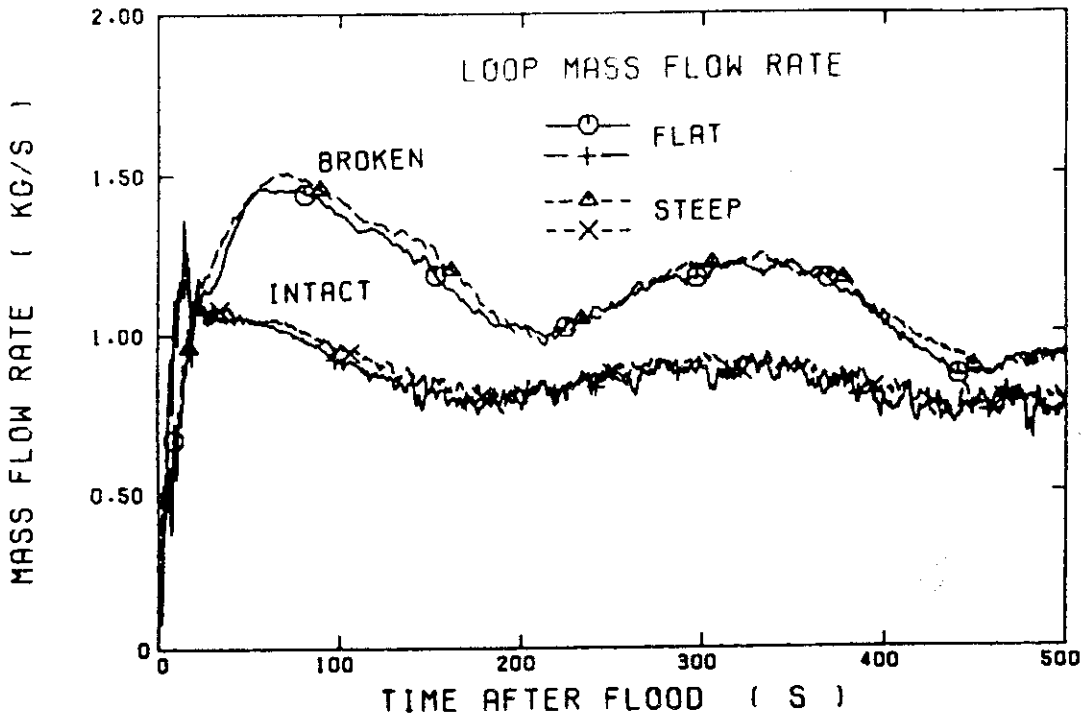

Fig. 4.5 Mass flow rates through the intact and broken loops

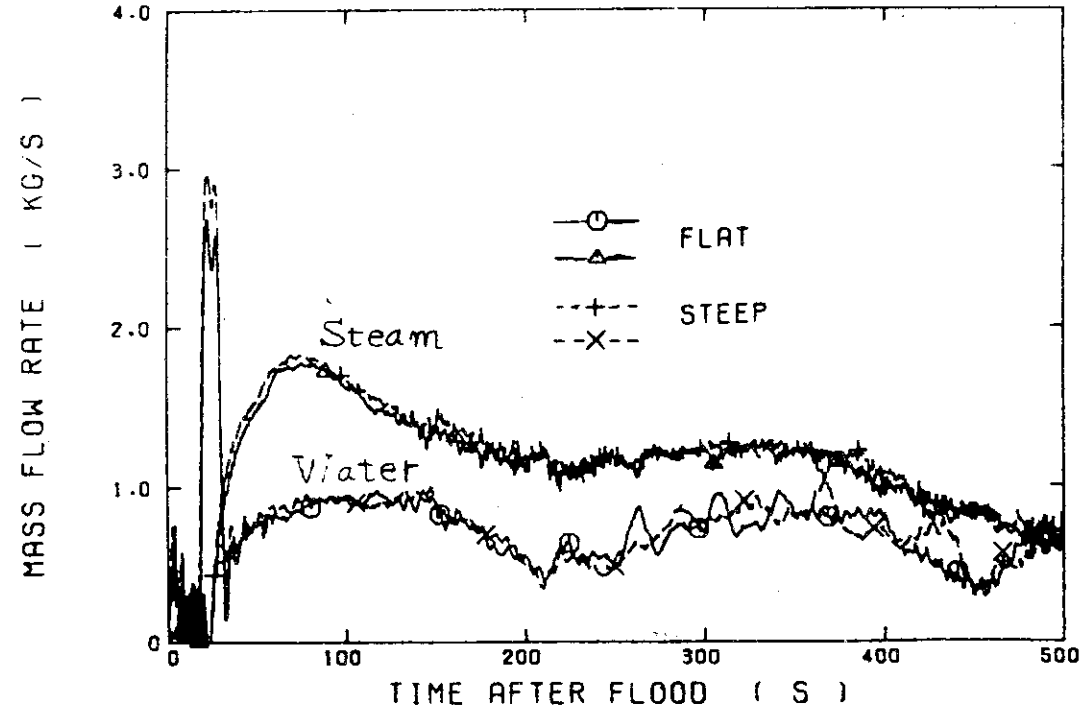

Fig. 4.6 Steam and water mass flow rates through the broken cold leg

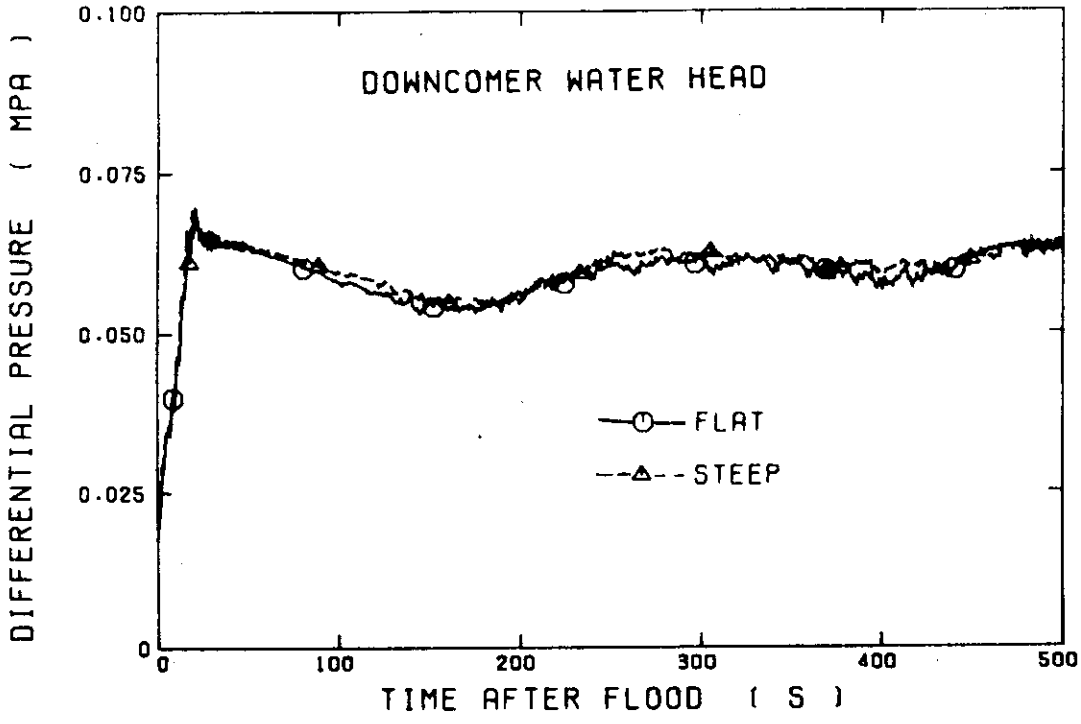

(a) through the downcomer

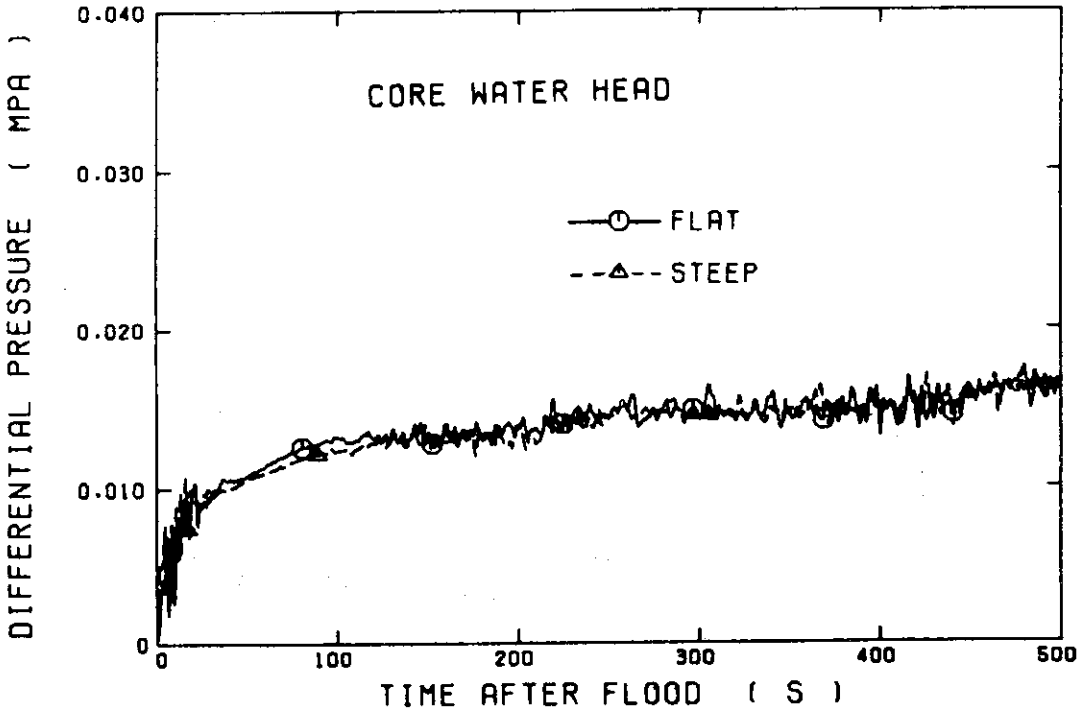

(b) through the core

Fig. 4.7 Differential pressure through the downcomer and the core

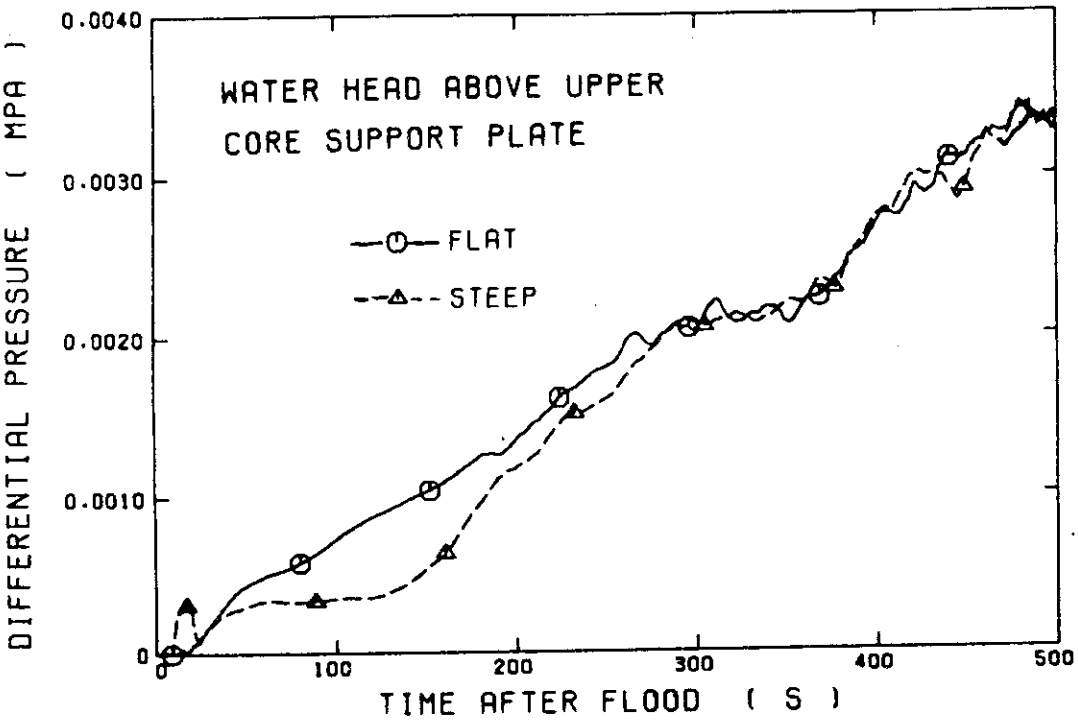

(a) above upper core support plate

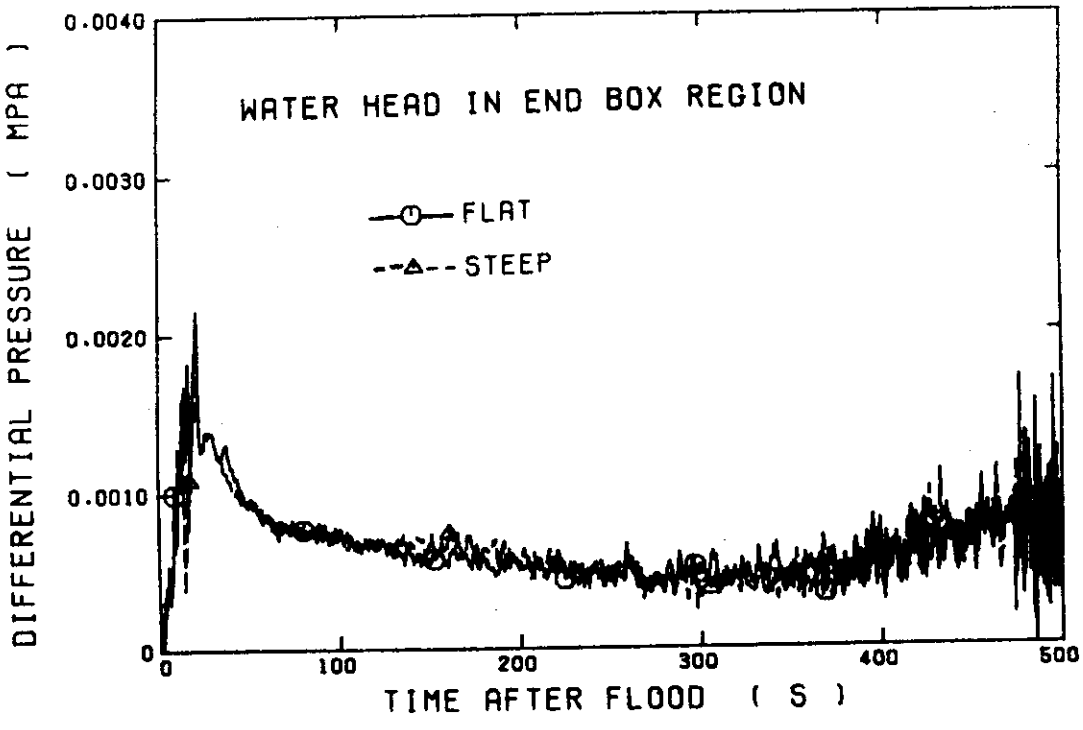

(b) in the end box region

Fig. 4.8 Differntial pressure through the upper plenum

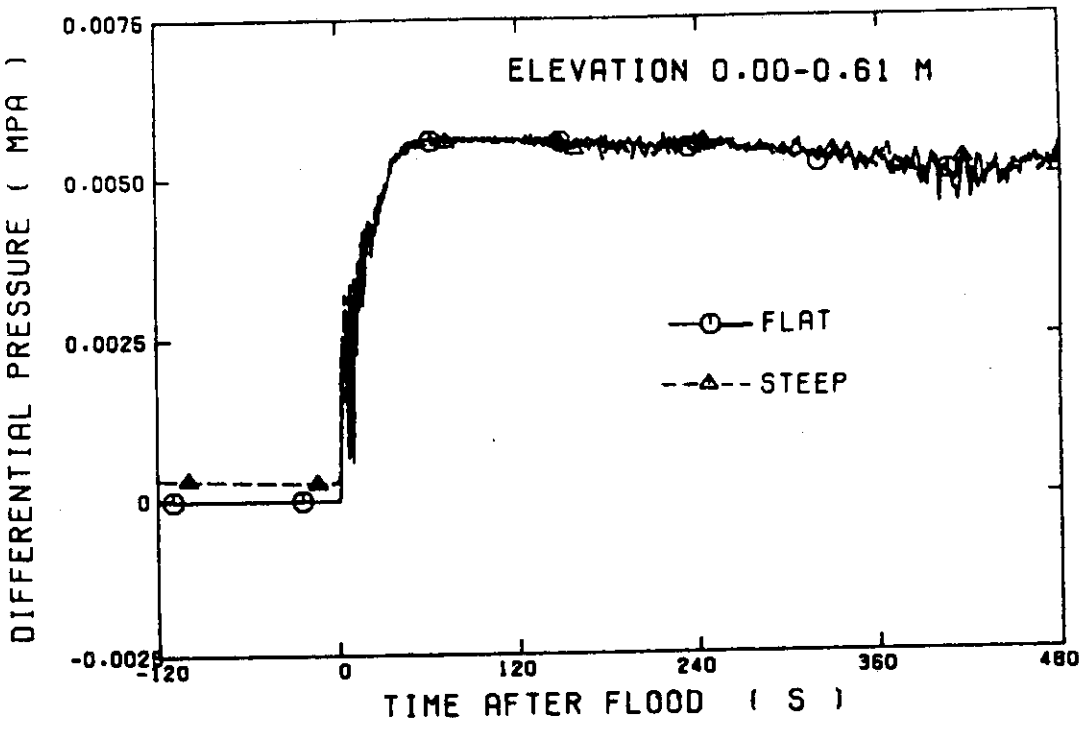

Fig. 4.9 Differential pressure in the core through the section between 0.00 and 0.61 m from the bottom of the core heated part

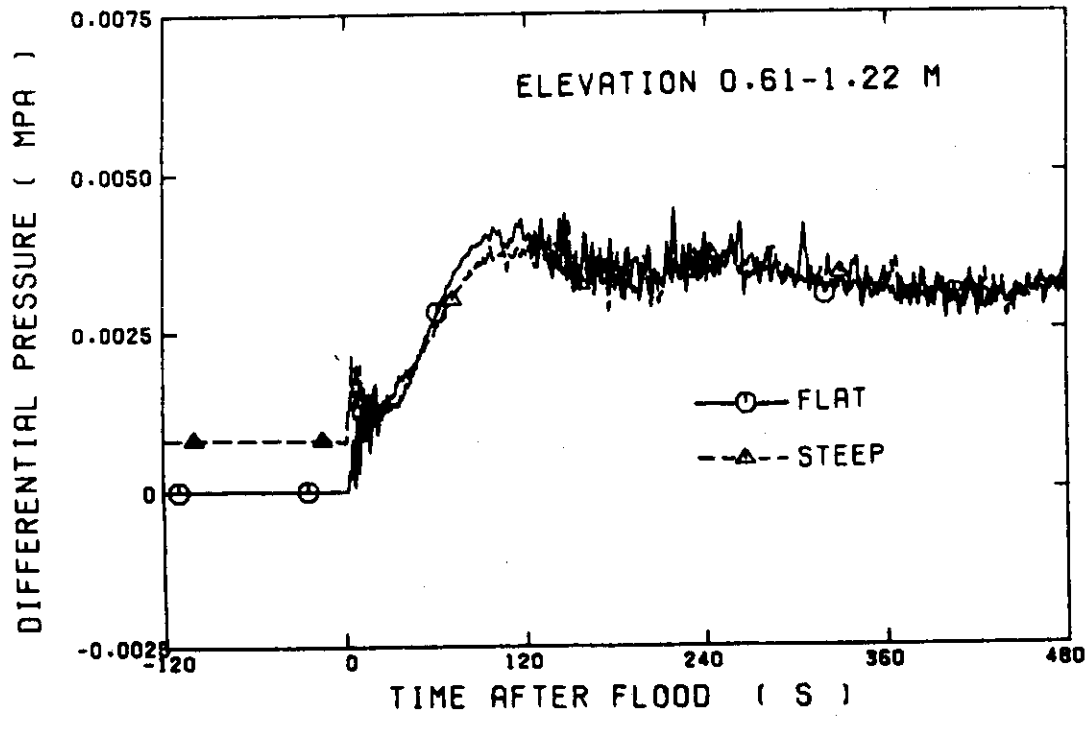

Fig. 4.10 Differential pressure in the core through the section between 0.61 and 1.22 m from the bottom of the core heated part

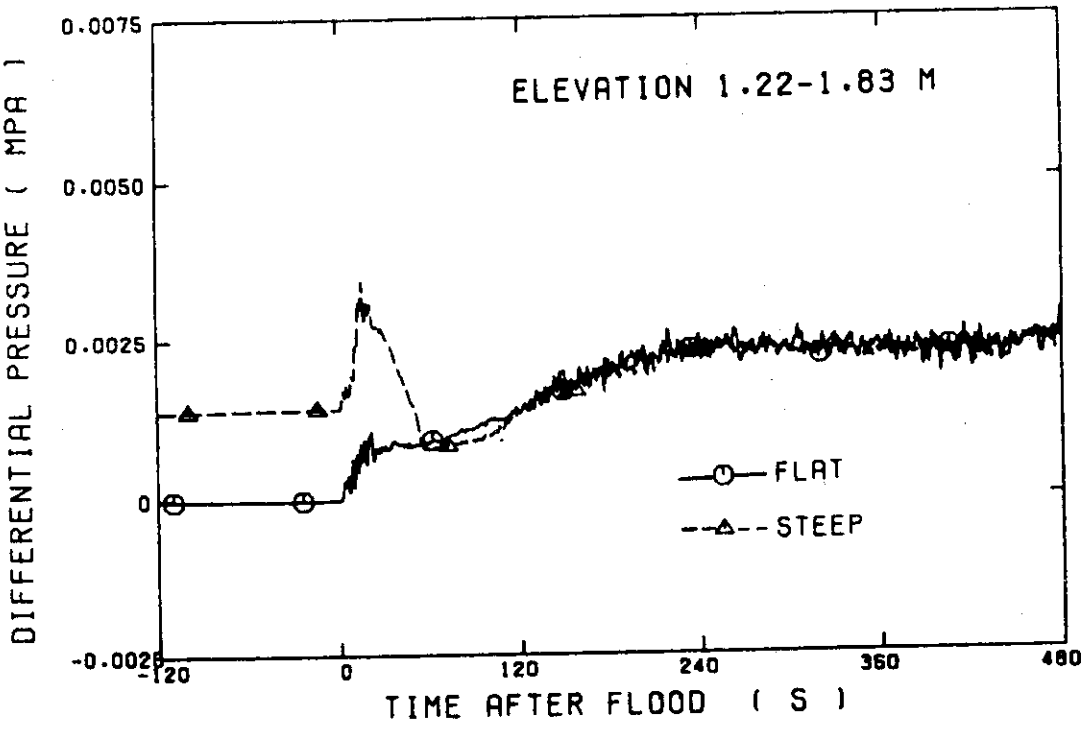

Fig. 4.11 Differential pressure in the core through the section between 1.22 and 1.83 m from the bottom of the core heated part

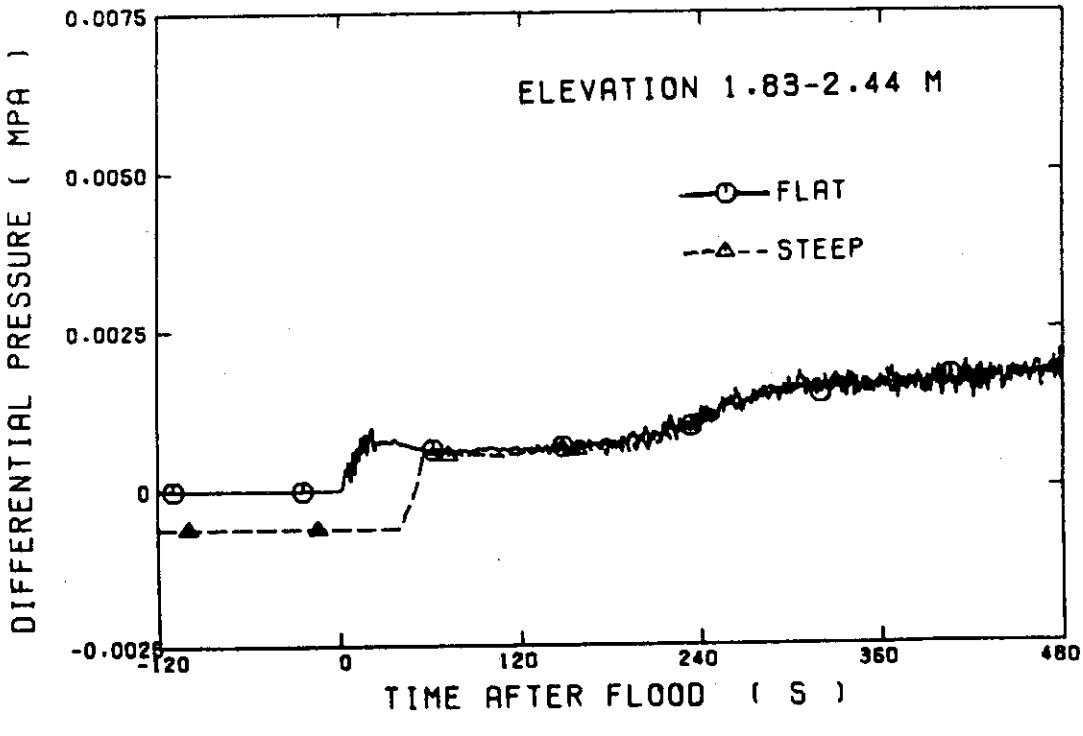

Fig. 4.12 Differential pressure in the core through the section between 1.83 and 2.44 m from the bottom of the core heated part

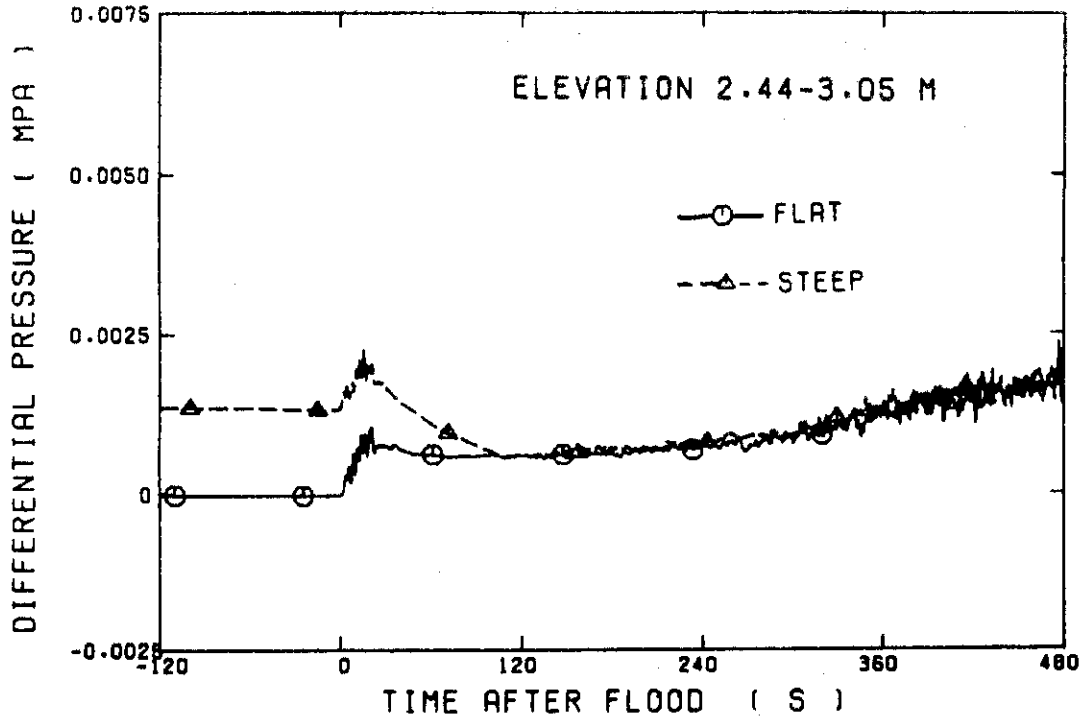

Fig. 4.13 Differential pressure in the core through the section between 2.44 and 3.05 m from the bottom of the core heated part

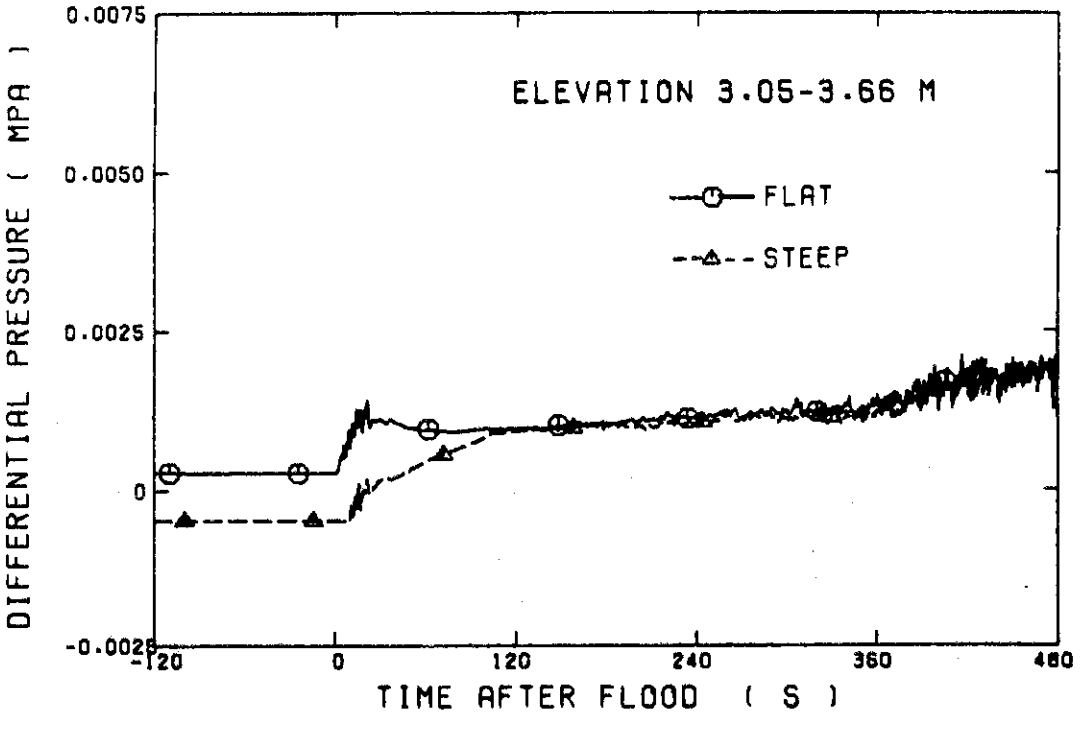

Fig. 4.14 Differential pressure in the core through the section between 3.05 and 3.66 m from the bottom of the core heated part

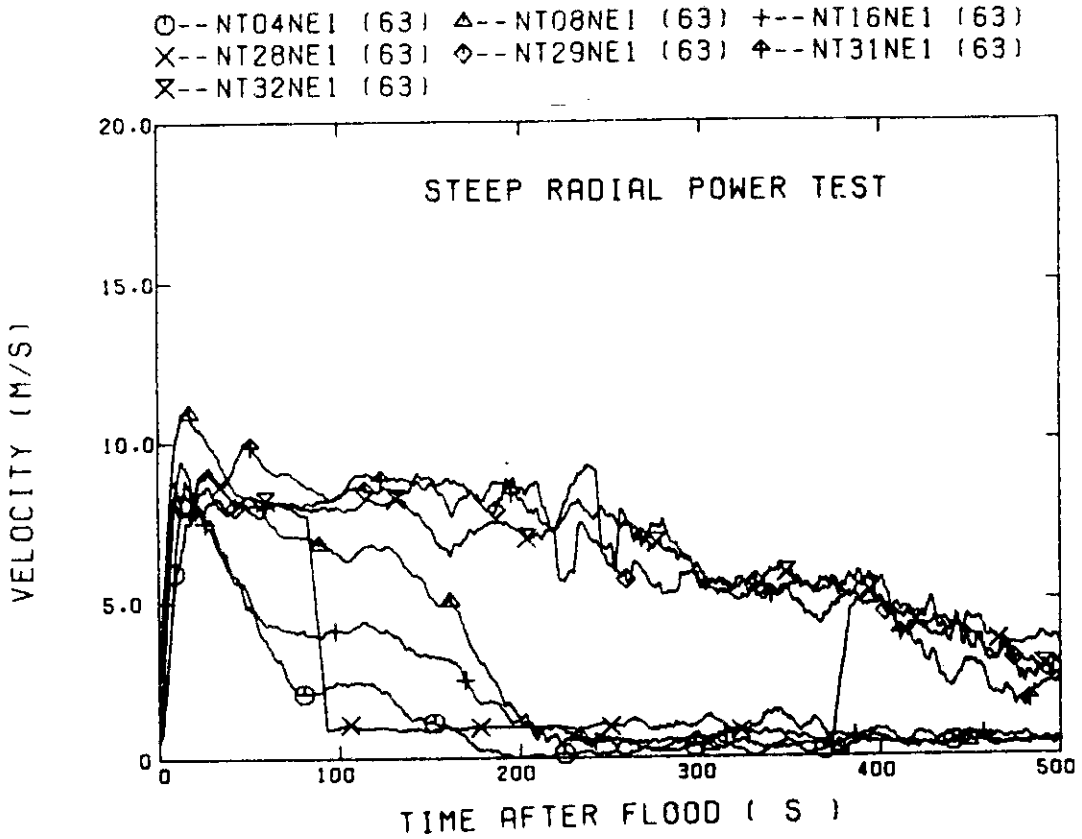

Fig. 4.15 Turbine flowmeter outputs from the steep radial power test

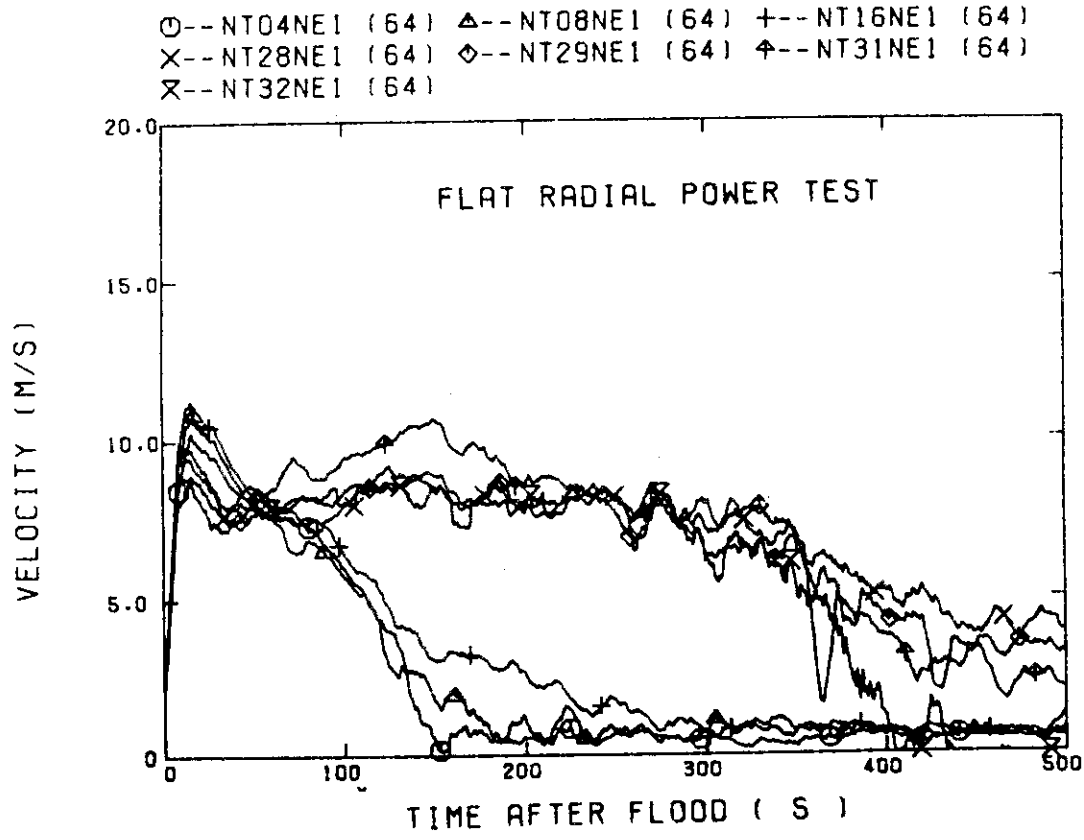

Fig. 4.16 Turbine flowmeter outputs from the flat radial power test

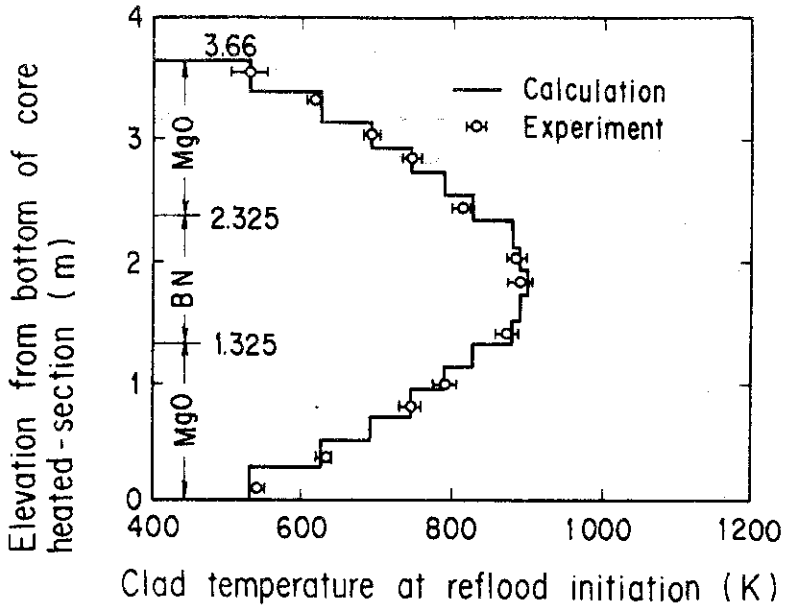

Fig. 4.17 Axial profile of the clad surface temperature at the reflood initiation in the flat radial power test

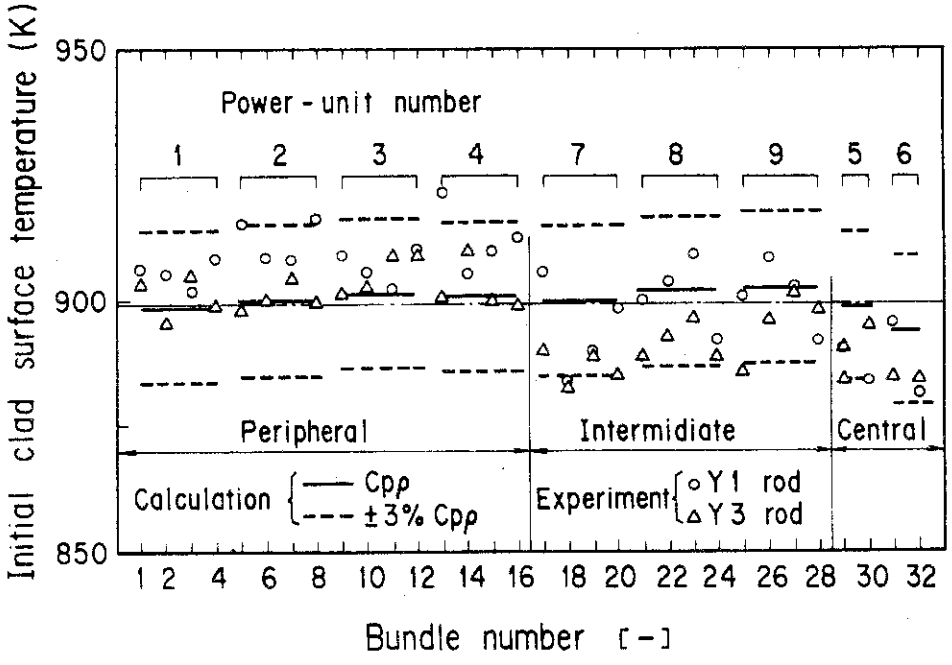

Fig. 4.18 Initial clad surface temperature at the midplane of heater rods in the flat radial power test

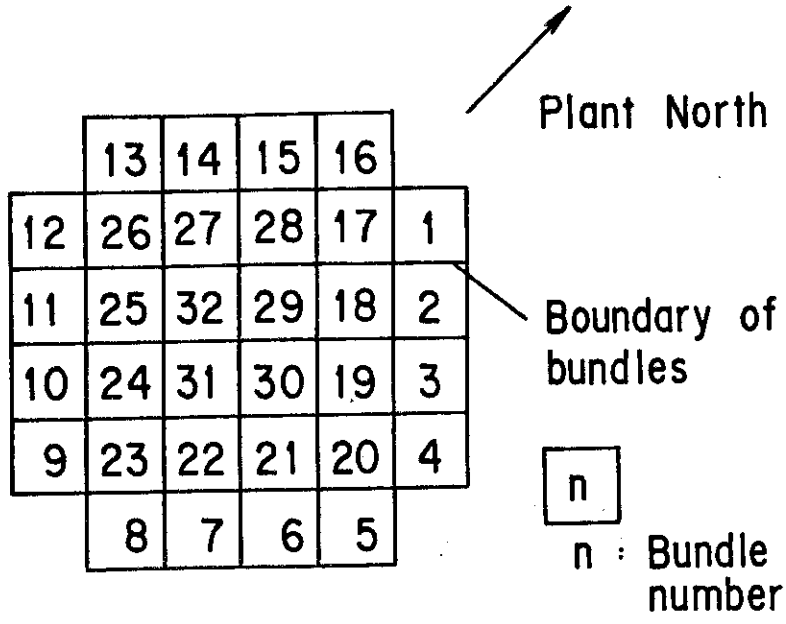

(a) Definition of bundle number

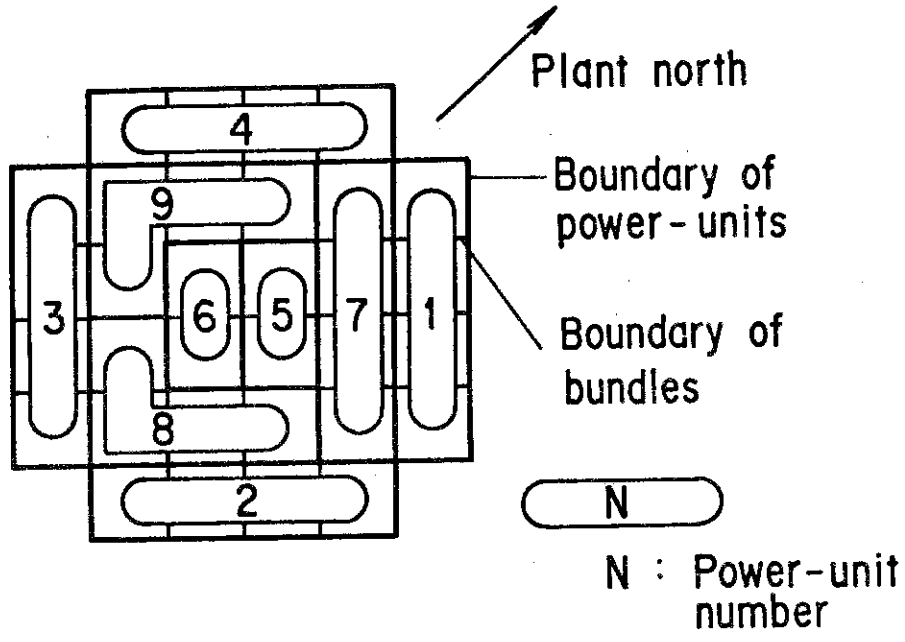

(b) Definition of power-unit number

Fig. 4.19 Definition of the power-unit and the bundle numbers

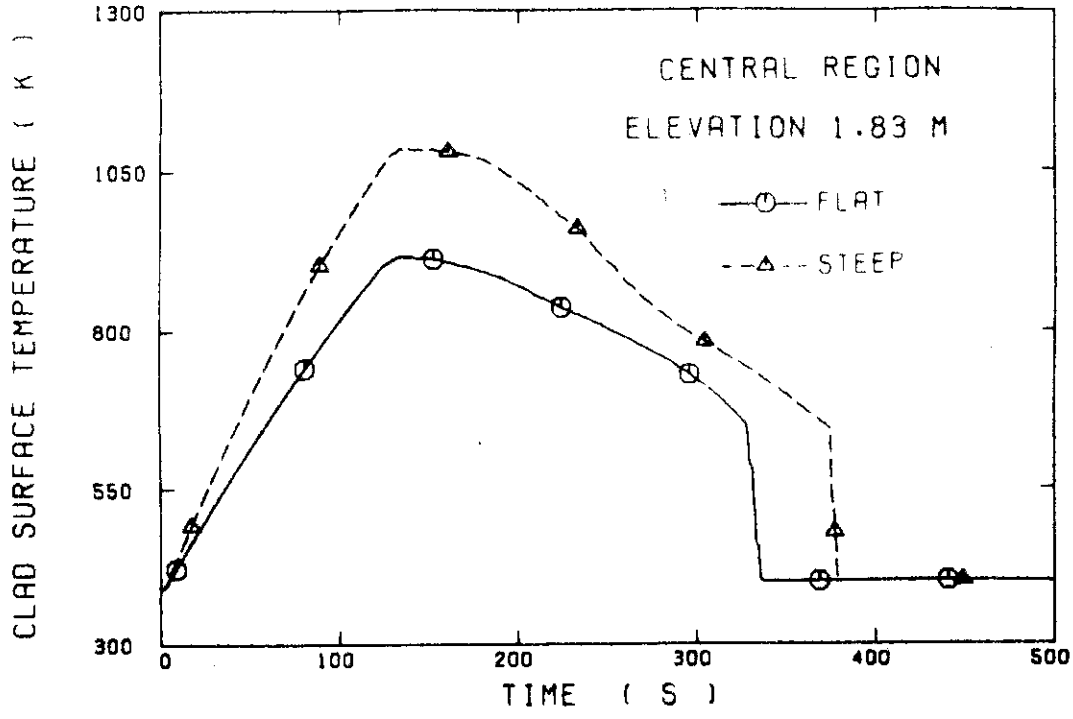

Fig. 4.20 Comparison of clad surface temperature at the midplane in the central region between the flat and steep radial power tests

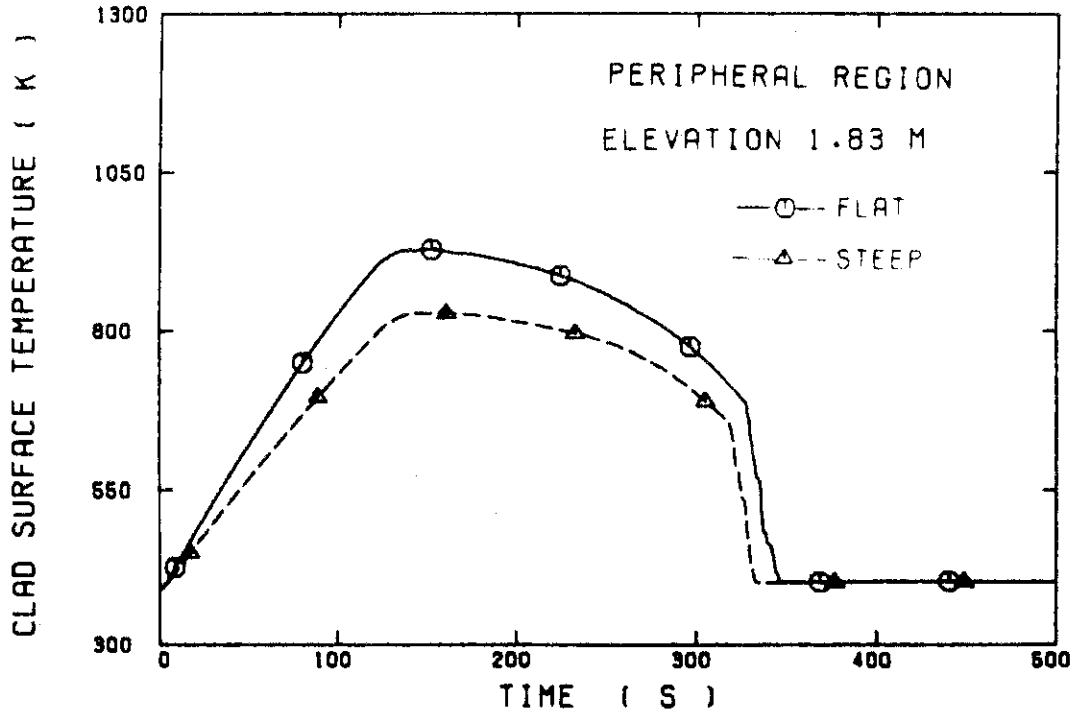

Fig. 4.21 Comparison of clad surface temperature at the midplane in peripheral region between the flat and steep radial power tests

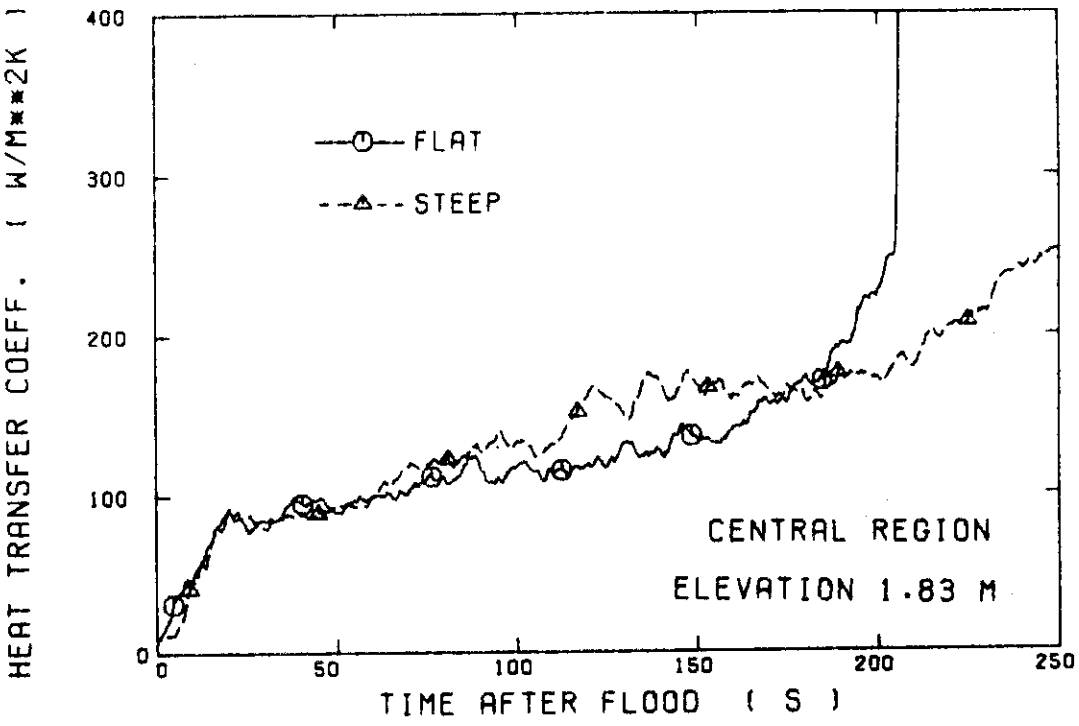

Fig. 4.22 Comparison of heat transfer coefficient at the midplane in the central region between the flat and steep radial power tests

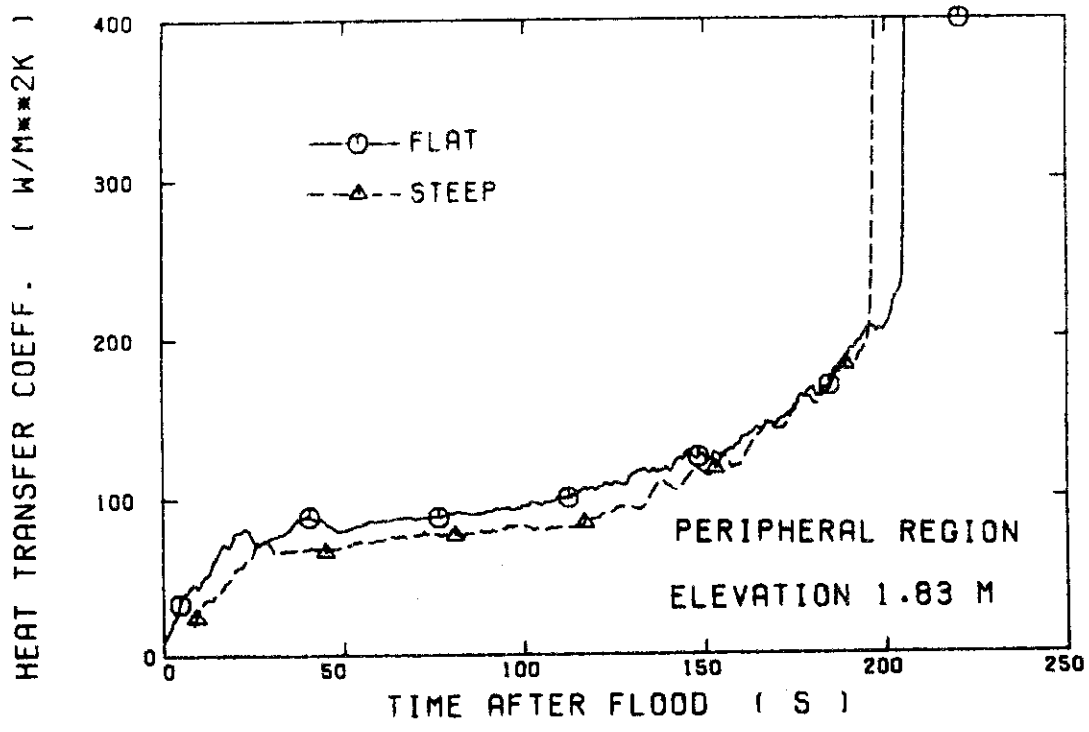

Fig. 4.23 Comparison of heat transfer coefficient at the midplane in the peripheral region between the flat and steep radial power tests

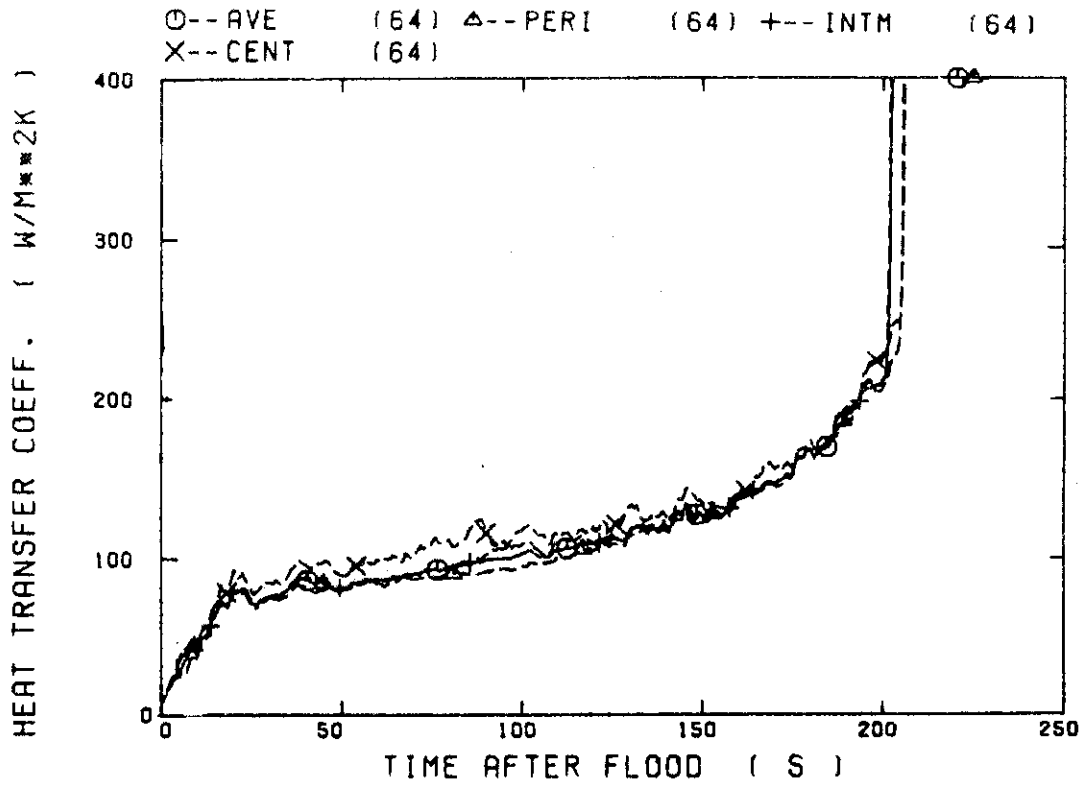

Fig.4.24 Heat transfer coefficient at the midplane in the flat radial power test

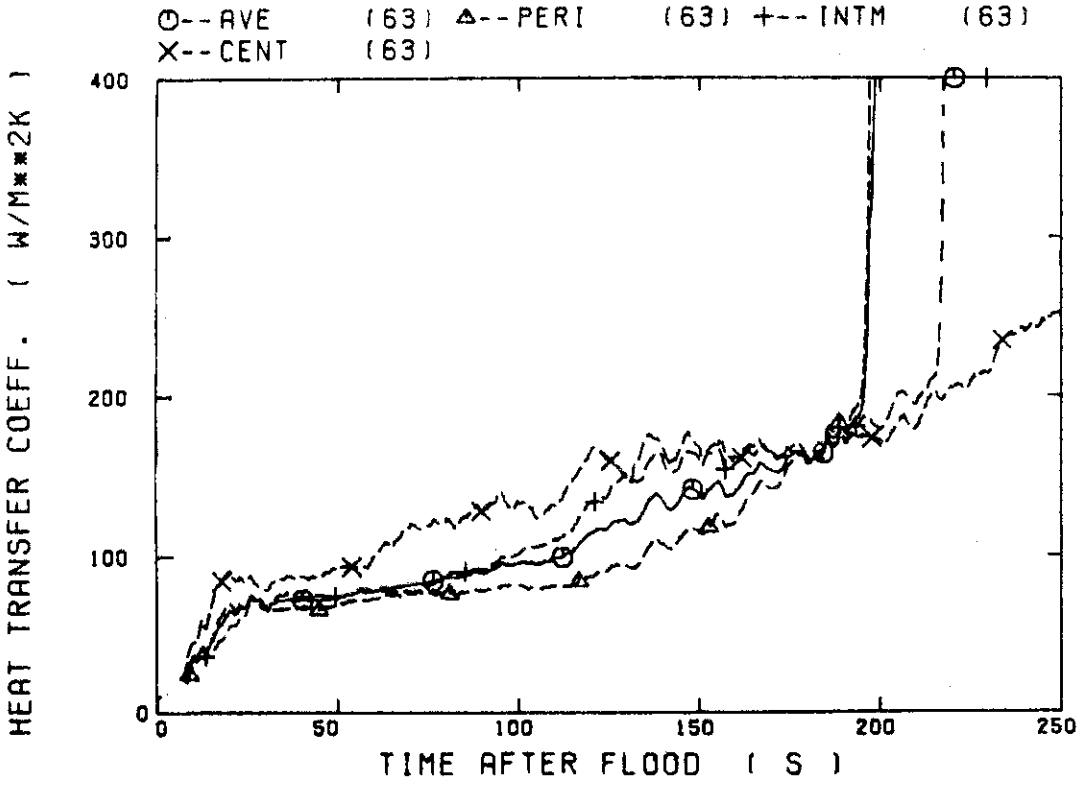

Fig.4.25 Heat transfer coefficient at the midplane in the steep radial power test

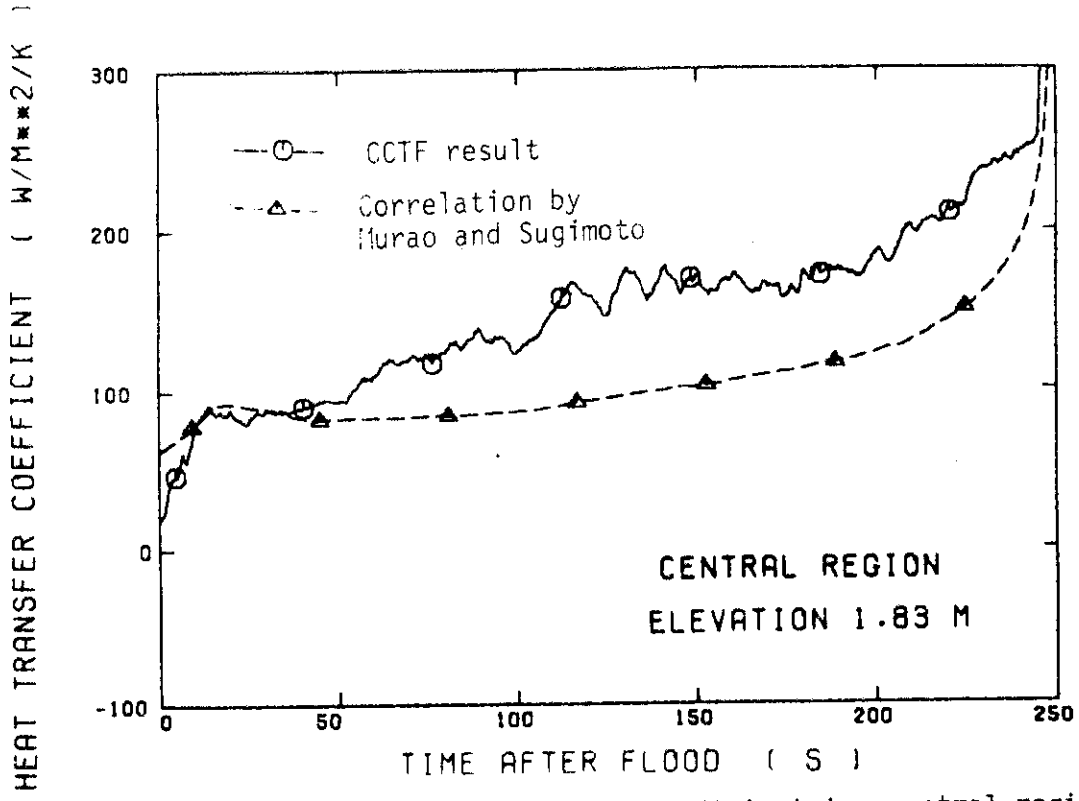

Fig. 4.26 Comparison of heat transfer coefficient in central region

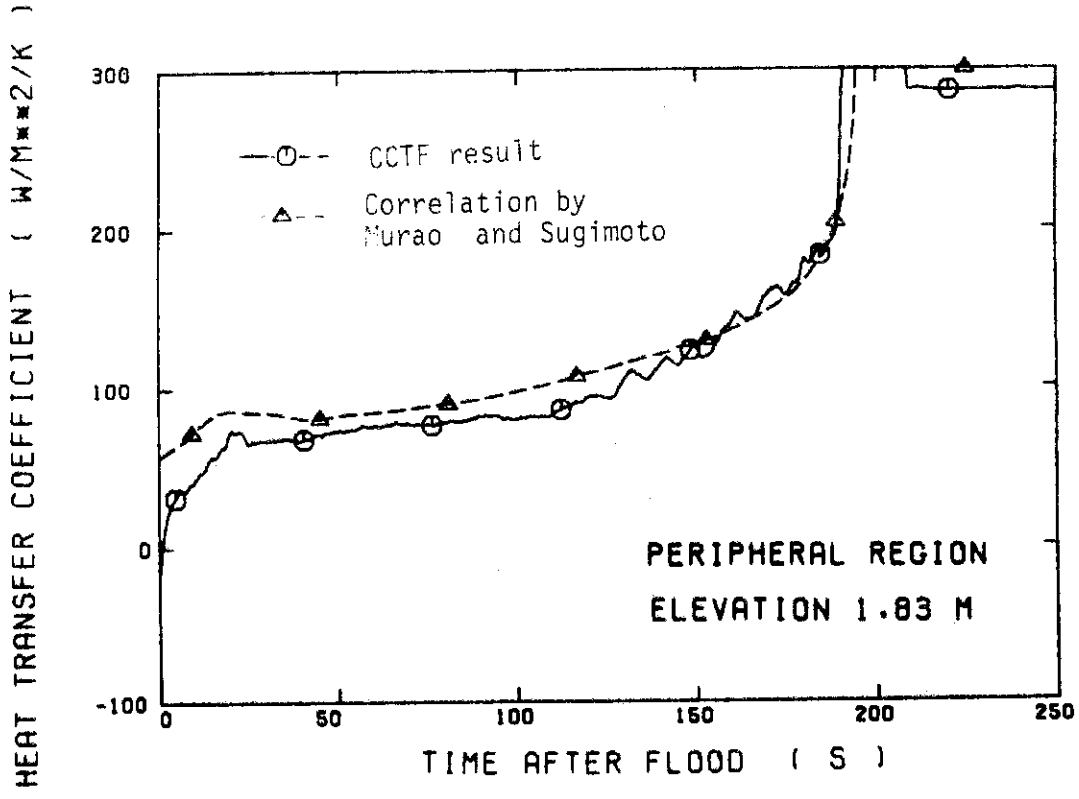

Fig. 4.27 Comparison of heat transfer coefficient in peripheral region

5. Conclusions

In order to evaluate the effect of the radial power profile on the system behavior and the core thermal hydraulic behavior during the reflood phase of a PWR LOCA, a test was performed using the Cylindrical Core Test Facility(CCTF) with the flat radial power profile. The test was conducted with the same total core power as that of the steep radial power test C2-5(Run 63). Through the comparisons of the results from these two tests, the following conclusions were obtained:

(1) The radial power profile in the core has weak effect on the thermal hydraulic behavior in the primary system except the core.

(2) Almost the same differential pressure was observed at various elevations in the periphery of the core regardless of different radial power profile. The result suggests that the core differential pressure is determined mainly by the total power and the total stored energy rather than by the local power and the local stored energy.

(3)The test results support the single channel core model with the average power rod used in the reactor safety analysis codes such as REFLA-1DS, WREM for the evaluation of the overall system behavior.

(4) In the steep radial power test, the heat transfer coefficient in the central(high power) region was higher than that in the peripheral(low power) region. The tendency was not explained by the estimation with the heat transfer correlation developed by Murao et al. [5] assuming that the void fraction was uniform in a horizontal cross section. It is necessary to study more the dependency of core heat transfer on the radial power profile in the wide core.

Acknowledgements

The authors are much indebted to Drs. M. Nozawa, M. Hirata, and K. Hirano for their guidance and encouragement for this program.

The authors would like to express appreciation to the members of SCTF analysis group, especially Mr. H. Adachi, Dr. Y. Sudo, and Messrs. M. Sobajima, T. Iwamura, M.Osakabe, A.Ohnuki and Y. Abe for valuable discussions. The authors are deeply indebted to Messrs. Y.Fukaya, I. Arase, T. Wakabayashi, T.Oyama, Y. Niitsuma, K. Nakajima, T. Chiba, J. Matsumoto, K. Komori and H. Sonobe for their contribution of the test conduction.

References

(1)Murao,Y.,et al.: J. Nucl. Sci. Technol., 19(9), 705 (1982).
(2)Murao,Y. and Iguchi T.:JAERI-M 83-028, (1983).
(3)Iwamura,T.,et al.:J. Nucl. Sci. Technol.,20(9),743(1983).
(4)Hirano,K. and Murao Y.: J. At. Energy Soc. Japan,(in Japanese), 22(10), 681 (1980).
(5)Murao,Y. and Sugimoto,J.:J. Nucl. Sci. Technol.,18(4),275 (1981).

Acknowledgements

The authors are much indebted to Drs. M. Nozawa, M. Hirata, and K. Hirano for their guidance and encouragement for this program.

The authors would like to express appreciation to the members of SCTF analysis group, especially Mr. H. Adachi, Dr. Y. Sudo, and Messrs. M. Sobajima, T. Iwamura, M.Osakabe, A.Ohnuki and Y. Abe for valuable discussions. The authors are deeply indebted to Messrs. Y.Fukaya, I. Arase, T. Wakabayashi, T.Oyama, Y. Niitsuma, K. Nakajima, T. Chiba, J. Matsumoto, K. Komori and H. Sonobe for their contribution of the test conduction.

References

(1)Murao,Y.,et al.: J. Nucl. Sci. Technol., 19(9), 705 (1982).
(2)Murao,Y. and Iguchi T.:JAERI-M 83-028, (1983).
(3)Iwamura,T.,et al.:J. Nucl. Sci. Technol.,20(9),743(1983).
(4)Hirano,K. and Murao Y.: J. At. Energy Soc. Japan,(in Japanese), 22(10), 681 (1980).
(5)Murao,Y. and Sugimoto,J.:J. Nucl. Sci. Technol.,18(4),275 (1981).

Appendix A

Definition of Tag IDs

Figure List

1. Definition of Tag. ID for clad surface temperatures and heat fransfer coefficients

Notation : TEnnYlm (temperature)

HTEmmYlm (heat transfer coefficient)

nn : Bundle number (see Fig. A.1)

m : Elevation number

	Elevation (m)	Axial power factor
3	0.38	0.651
5	1.015	1.147
7	1.83	1.40
9	2.44	1.256
A	3.05	0.854

2. Definition of power zone and boundle number

See Fig. A.1

3. Definition of Tag. ID for void fraction

See Fig. A.2

4. Definition of Tag. ID for average linear power of heater rod in each power unit zone

See Fig. A.3

5. Definition of Tag. ID for differential pressure through downcomer, upper plenum, core and lower plenum

See Fig. A.4

6. Definition of Tag. ID for differential pressure through intact and broken loop and broken cold leg nozzle

See Fig. A.5

7. Definition of Tag. ID for fluid temperature in inlet and outlet plenum and secondary side of steam generator

See Fig. A.6

8. Definition of Tag. ID for ECC water injection rate, ECC water temperature and vented steam flow rate

See Fig. A.7

9. Definition of initial temperature, turnaround temperature quench temperature, temperature rise, turnaround time and quench time. (See Fig. A.8

T_i : Initial temperature (Clad surface temperature at reflood initiation)

T_t : Turnaround temperature (Maximum clad surface temperature in each temperature history)

ΔT_r : Temperature rise ($= T_t - T_i$)

T_q : Quench temperature (Clad surface temperature at quenching)

10. Definition of quenching

See Fig. A.8

Quench time t_t is determined as

$$t_t = i \times \Delta t - \text{(reflood initiation time)}$$

In above equation, i is determined by the following criteria.

(1) Clad surface temperature is high, compared with the saturation temperature.

$$T_i > T_{sat} + \Delta T_1$$

(2) Decreasing rate of clad surface temperature is large.

$$\frac{T_{i+1} - T_i}{\Delta t} < - C_{st}$$

(3) Clad surface temperature falls around the saturation temperature.

$$T_{i + k_1} \leq T_{sat} + \Delta T_1$$

(4) If the determined i is inadequate, the value i is manually re-determined.

Δt : Data sampling period (s)

T_i : Clad surface temperature (K)

T_{sat} : Saturation temperature at the pressure in upper plenum (K)

ΔT_1 : Temperature discrepancy (K)
Default value = 50.0

C_{st} : Decreasing rate of clad surface temperature (K/S)
Default value = 25.0

k_1 : Number of referred data (-)
Default value = 6

11. Definition of Tag. ID for core inlet mass flow rate, time-integral core inlet mass flow rate and carry-over rate fraction

(1) Core inlet mass flow rate : $\dot{m}_F$
Notation : MLCRI□ (□ = N, 1 or 11)

(2) Time-intefral core inlet mass flow rate : $\int \dot{m}_F dt$
Notation : IMLCRI□ (□ = N, 1 or 11)

(3) Carry-over rate fraction : $(\dot{m}_F - \dot{m}_{CR})/\dot{m}_F$
Natation : CRF□ (□ = N, 1 or 11)

where $\dot{m}_F$: Core inlet mass flow rate (See item 12)

$\dot{m}_{CR}$: Water accumulation rate in core

Suffix	$\dot{m}_F$ base on
N	Eq.(A.2)
1	Eq.(A.1) with K=15
11	Eq.(A.1) with K=20

12. Evaluation of core inlet mass flow rate

The reflood phenomena is a relatively slow transient and a steady state condition can be applied. In a steady state condition, based on the mass balance relations of the system, the core flooding mass flow rates $\dot{m}_F$s can be written as follows:

By using the data measured at the downstream of the core inlet, $\dot{m}_F$ is derived as,

$$\dot{m}_F = \dot{m}_C + \dot{m}_U + \dot{m}_B + \lambda \dot{m}_I \quad , \qquad (A.1)$$

where $\dot{m}_C$ and $\dot{m}_U$ are the mass accumulation rates in the core and the upper plenum respectively. The $\dot{m}_B$ and $\dot{m}_I$ are the mass flow rates in the broken loop and the intact loop, respectively.

By using the data measured at the upstream of the core inlet, $\dot{m}_F$ is derived as,

$$\dot{m}_F = \Sigma \dot{m}_{DL} - \dot{m}_D - \dot{m}_O + \dot{m}_{ECC/LP} \quad , \tag{A.2}$$

where $\dot{m}_{DL}$ and $\dot{m}_O$ are the mass flow rates of the water flowing into and overflowing from the downcomer, $\dot{m}_{ECC/LP}$ and $\dot{m}_D$ are the mass flow rate of the ECC water injected into the lower plenum and the water accumulation rate in the dowmcomer respectively.

The $\dot{m}_I$s and $\dot{m}_B$ can be obtained from the pressure drops at the pump simulators with orifices by assuming the K-factor of the orifice is constant. The values of $\dot{m}_C$, $\dot{m}_D$ and $\dot{m}_U$ can be evaluated with the differential pressure ΔP_C, ΔP_D and ΔP_U, respectively, as follows:

$$\dot{m}_n = d(\Delta P_n S_n/g)/dt \quad (n : C, D, U) \quad , \tag{A.3}$$

where g is the gravitational acceleration and S_n is the cross sectional area. The value of $\dot{m}_O$ can be obtained from the liquid level X in the Containment tank 1 as,

$$\dot{m}_O = d(X\rho_\ell S_o)/dt \quad , \tag{A.4}$$

where ρ_ℓ is the liquid density and S_o is the cross sectional area of the containment tank 1.

The value of $\dot{m}_{DL}$, $\dot{m}_{DV}$ and h, which are liquid flow rate, steam flow rate and enthalpy of two phase mixture downstream each ECC port respectively, are obtained from the following mass and energy balance relations at each ECC port under the assumption of thermal equilibrium:

$$\dot{m}_{DV} + \dot{m}_{DL} = \dot{m}_{ECC} + \dot{m}_I \quad , \tag{A.5}$$

$$(\dot{m}_{DV} + \dot{m}_{DL})i = \dot{m}_{ECC}h_{ECC} + \dot{m}_I h_I \quad , \tag{A.6}$$

$$\text{if} \quad h_g \geq h \geq h_\ell \; , \; (\dot{m}_{DV} + \dot{m}_{DL})h = \dot{m}_{DV}h_g + \dot{m}_{DL}h_\ell$$

$$\text{if} \quad h \geq h_g \quad , \; \dot{m}_{DL} = 0 \quad , \tag{A.7}$$

$$\text{if} \quad h \geq h_\ell \quad , \; \dot{m}_{DV} = 0$$

where h is enthalpy of fluid and h_ℓ and h_g are enthalpies of liquid and steam at the saturation temperature, respectively.

The fluid temperatures can be measured with thermocouples immersed in the fluid and the enthalpies h_I and h_{ECC} can be estimated.

Mass balance calculations were performed with Eqs. (A.1) and (A.2). The K-factor of the orifice in the pump simulator was evaluated in the following two ways.

The K-factor of 20 was obtained with the steam and water single phase calibration tests using the flow meter and spool piece data. The K-factor of 15 was obtained with the Pitot tube measurement in a typical reflood condition assuming the flat velocity profile in the pipings. In the differentiation, higher frequency components of the data tends to be amplified more. Therefore, in the differentiation of the differential pressure data, the smoothing procedure was used to suppress the high frequency components of the data.

In the Acc injection period, the calculated $\dot{m}_F$s with Eqs. (A.1) and (A.2) are significantly different from each other. This discrepancy may be caused by inaccuracy of the mass flow rate injected into the system and by the unaccounting of the storage of water in the cold leg pipe. The former might be introduced from the slow time response of the flow meter (time constant 1 second) and the change of the gas volume in the injection line. In this period, especially before the steam generation from the core becomes noticeable, the mass flow rate, $\dot{m}_F$, calculated with Eq. (A.1) is probably reasonable, since the calculation uses the increasing rates of the masses in the core and the upper plenum and their accuracy is good enough for our estimation.

In the LPCI injection period, the calculated $\dot{m}_F$s are slightly different from each other. Judging from the time-integral values of both $\dot{m}_F$s, their average values are nearly proportional. The discrepancy was inferred to be caused by the disregard of the bypass of steam and liquid from the upper plenum without going through the hot legs in the calculation with Eq. (A.1). And additionally the discrepancy was caused by the disregard of the steam generation in the downcomer due to the hot wall of the pressure vessel in the calculation with Eq. (A.2). It was estimated that the disregard of the downcomer steam generation causes the error of 0.25 kg/s on predicted $\dot{m}_F$. The estimation was made by comparing the results of the tests with hot and cold downcomer conditions.

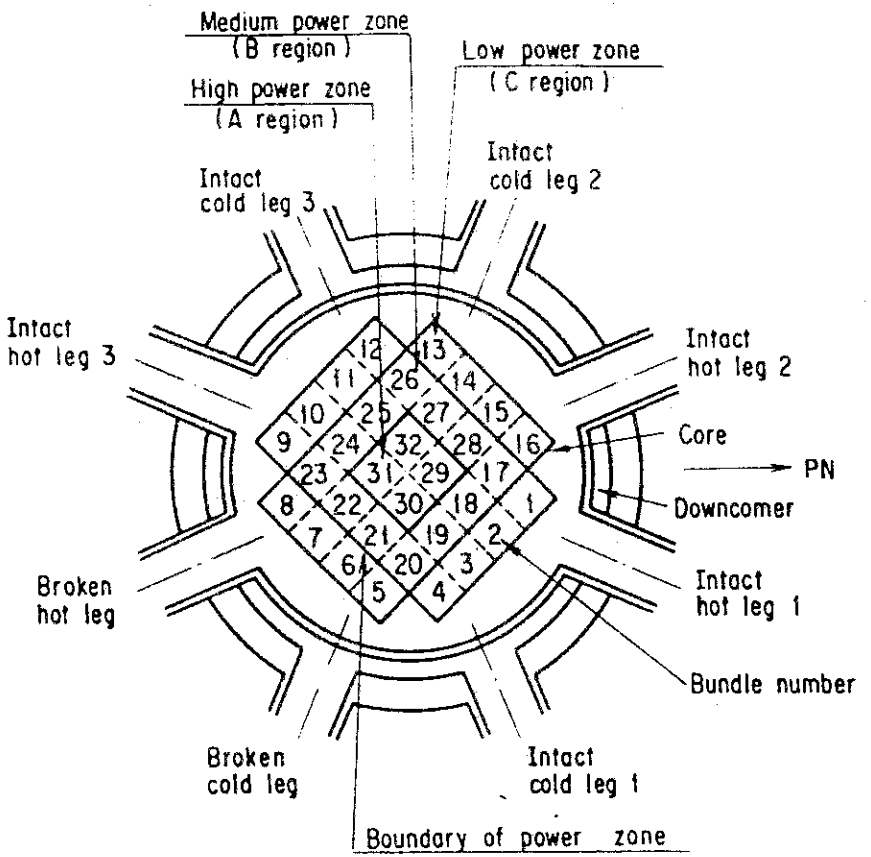

Fig. A. 1 Definition of power zones and bundle numbers

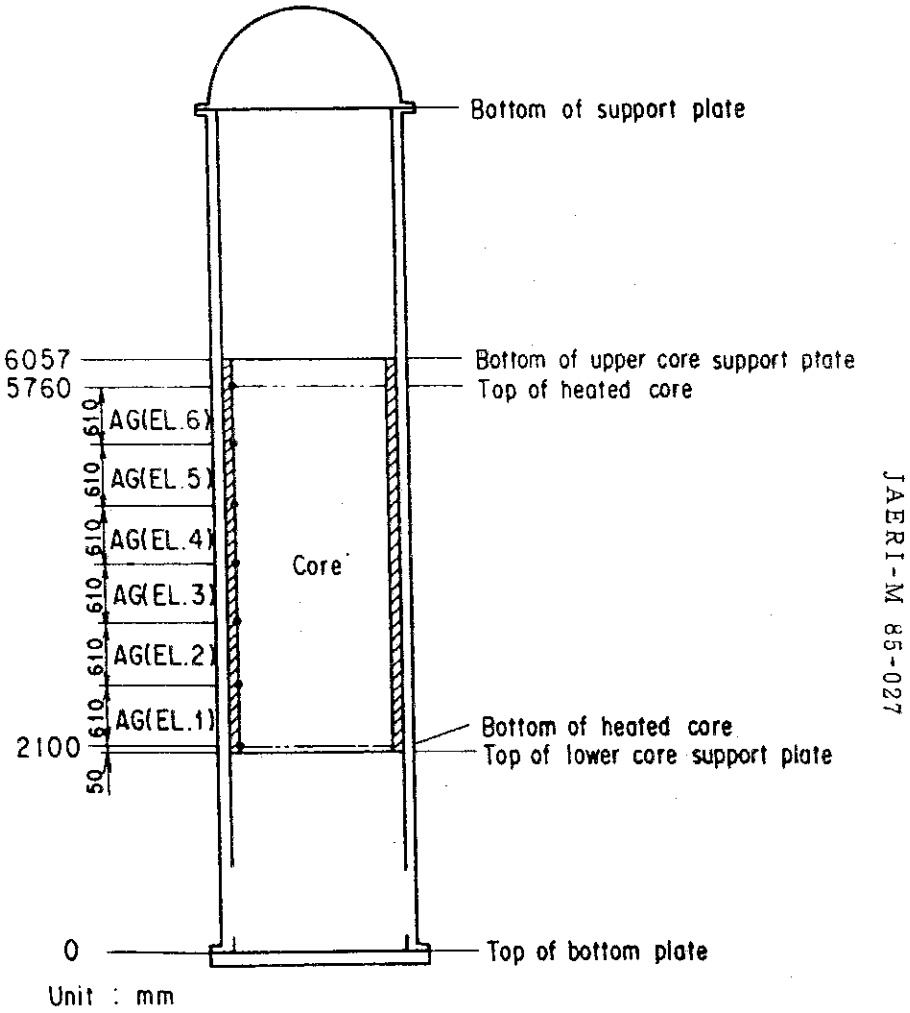

Fig. A. 2 Definition of Tag ID for void fraction (AG(EL. 1) ~ AG(EL. 6))

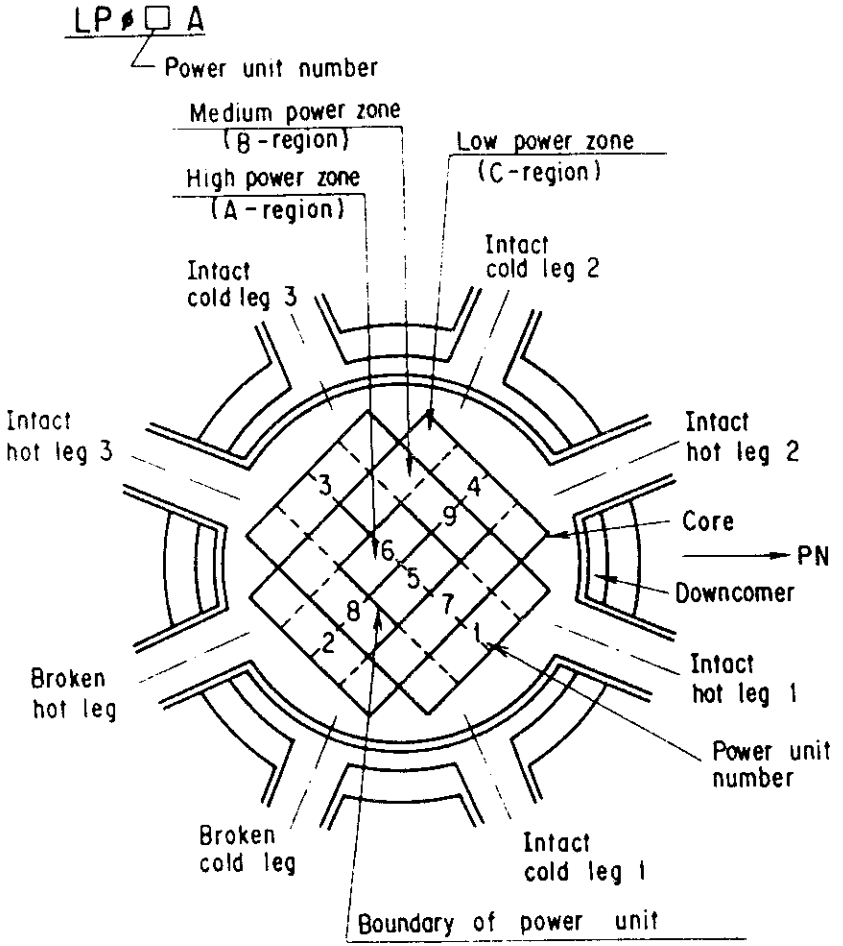

Fig. A. 3 Definition of Tag. ID for average linear power of heater rod in each power unit zone
(LP01A ~ LP09A)

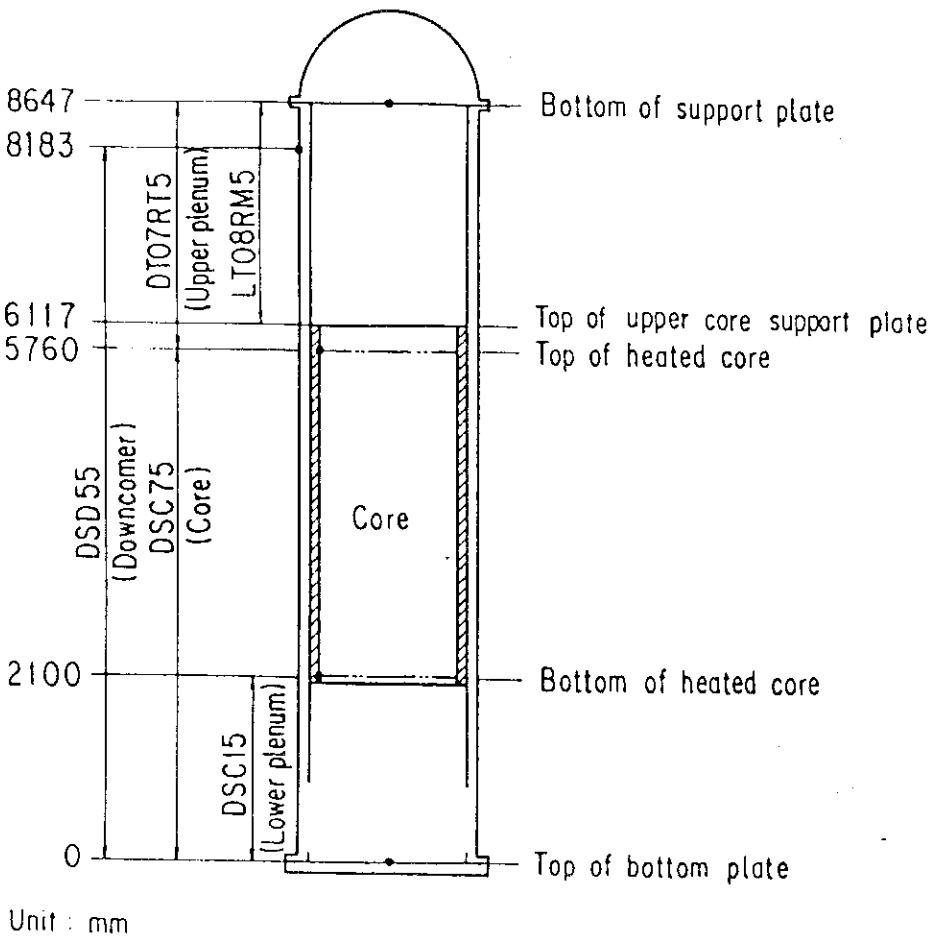

Fig. A. 4 Definition of Tag. ID for differential pressure through downcomer, upper plenum, core, and lower plenum
(DSD55, DT07RT5, LT08RM5, DSC75, DSC15)

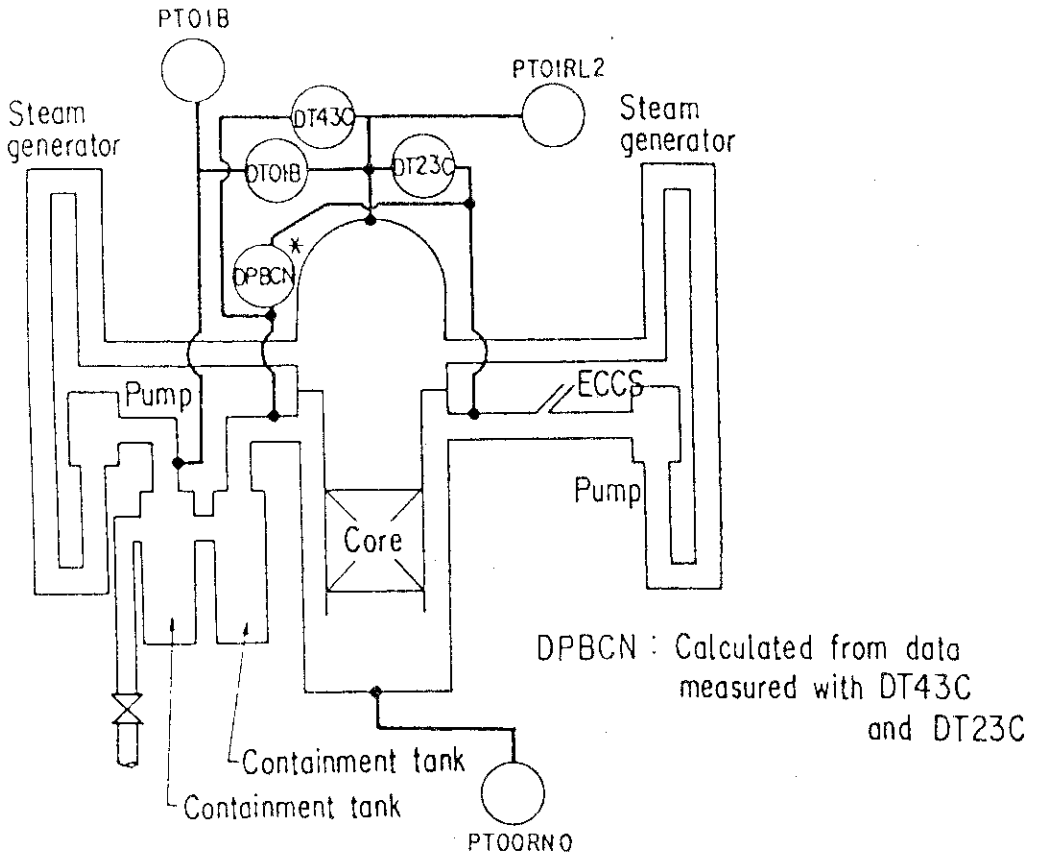

Fig. A. 5 Definition of Tag. ID for pressures in upper and lower plena and containment tank 2 (PT01RL2, PT00RN0, PT01B) and for differential pressure through intact and broken loop and broken cold leg nozzle (DT23C, DT01B, DPBCN)

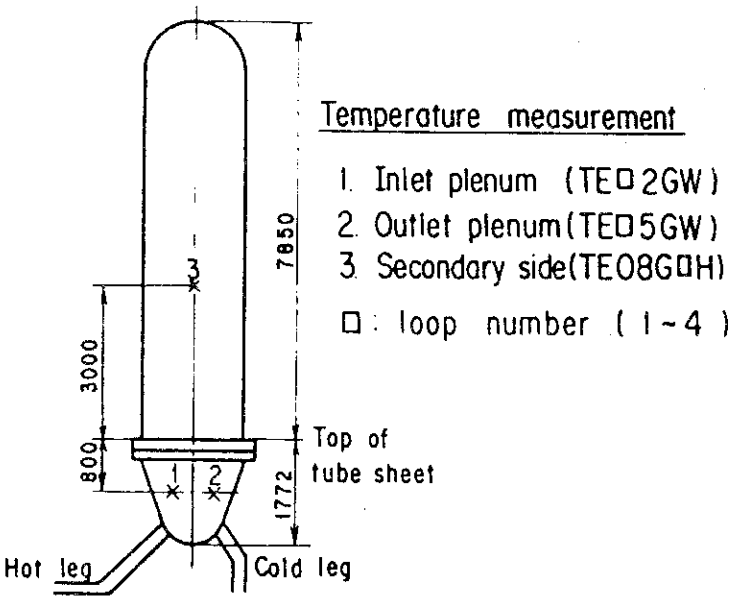

Fig. A. 6 Definition of Tag. ID for fluid temperature in inlet and outlet plenum and secondary of steam generator (TE□2GW, TE□5GW, TE08G□H)

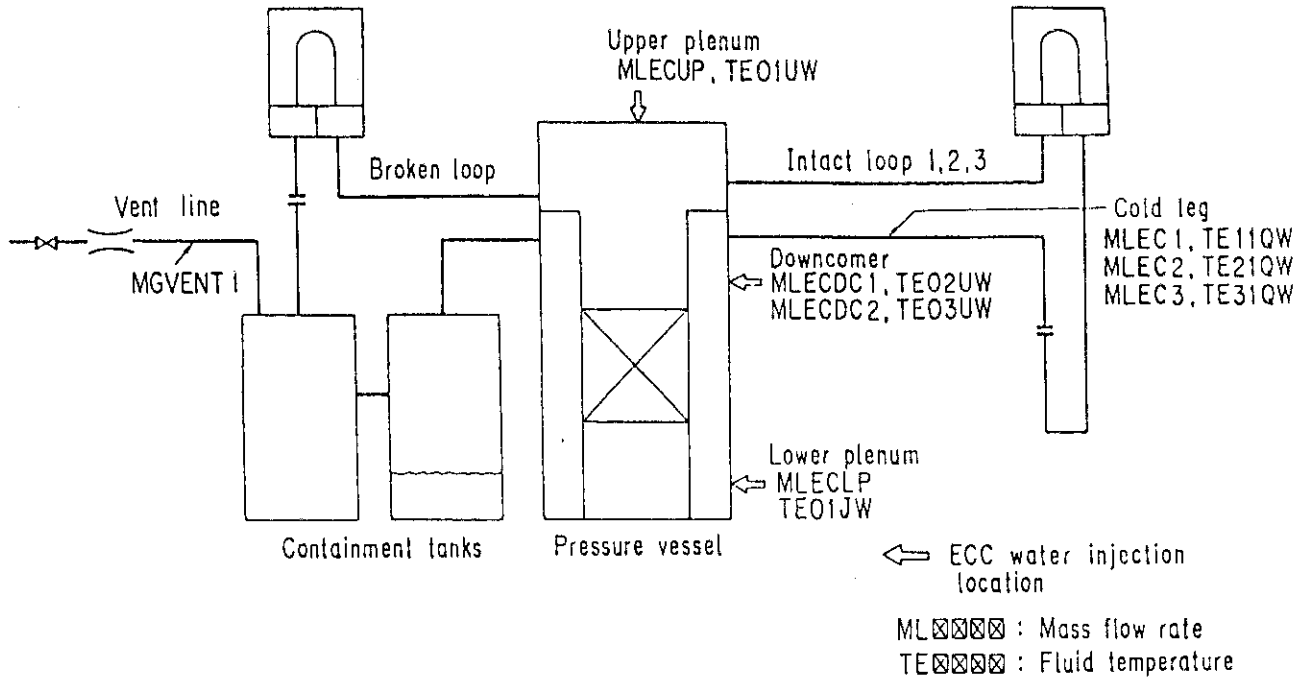

Fig. A. 7 Definition of Tag. ID for ECC water injection rate, ECC water temperature and vented steam flow rate

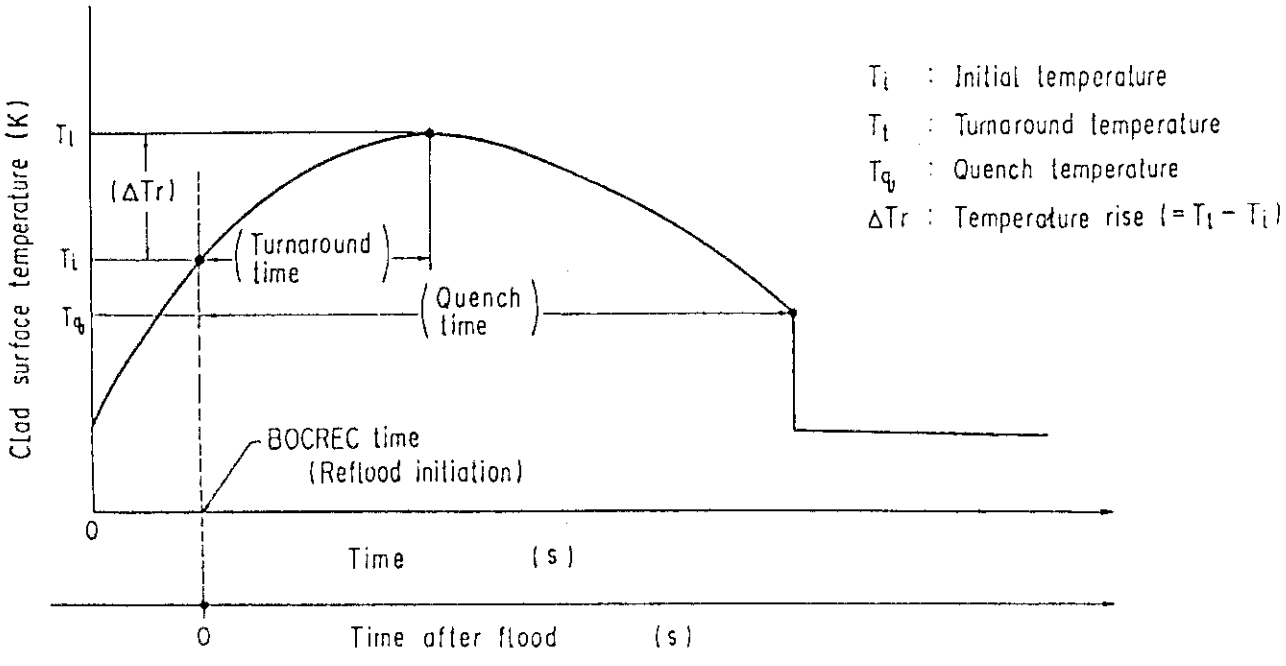

Fig. A. 8 Definition of initial temperature, turnaround temperature, quench temperature, temperature rise, turnaround time and quench time

Appendix B

Selected data of CCTF Test C2-6 (Run 64)

Figure List

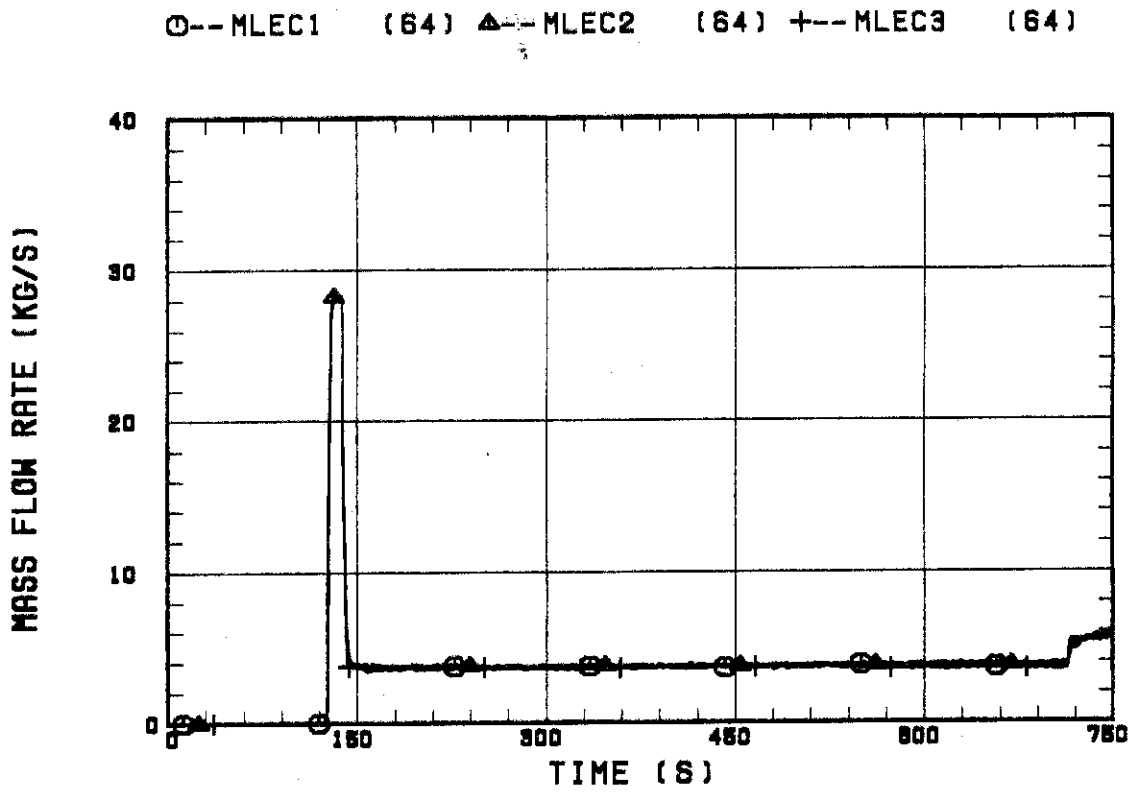

Fig. B.1 ECC water injection rates into the primary system.

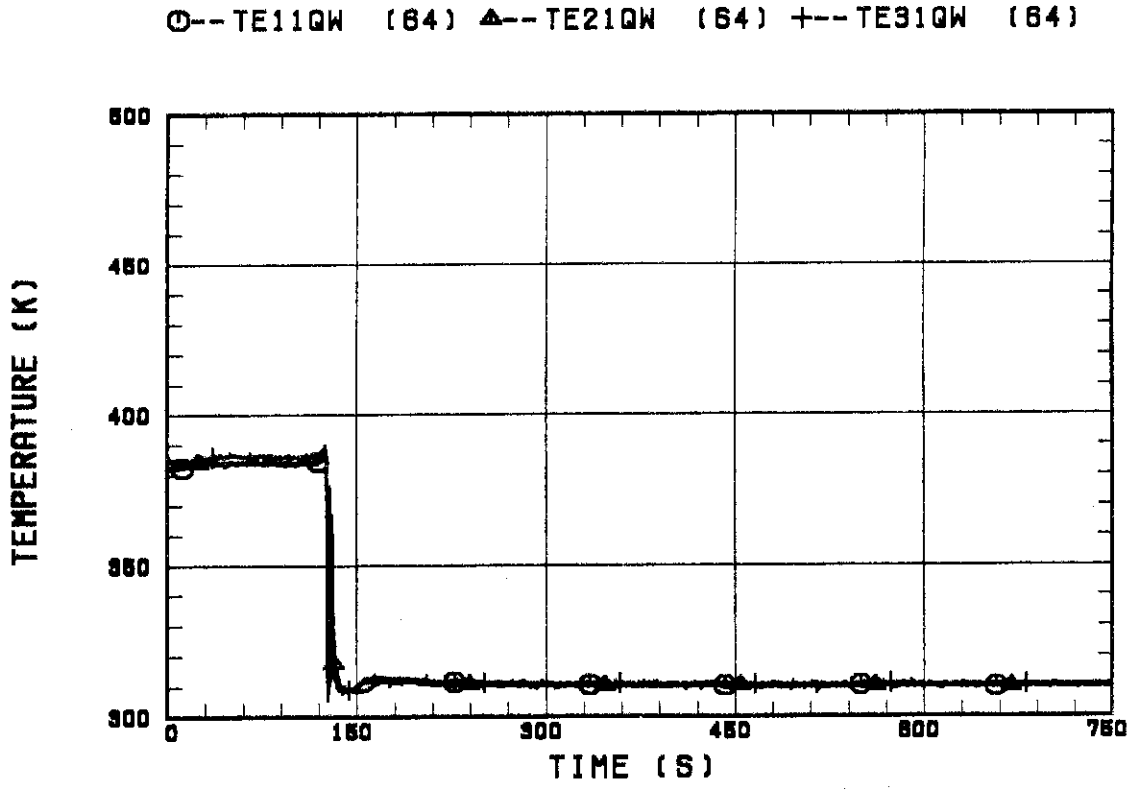

Fig. B.2 ECC water temperature.

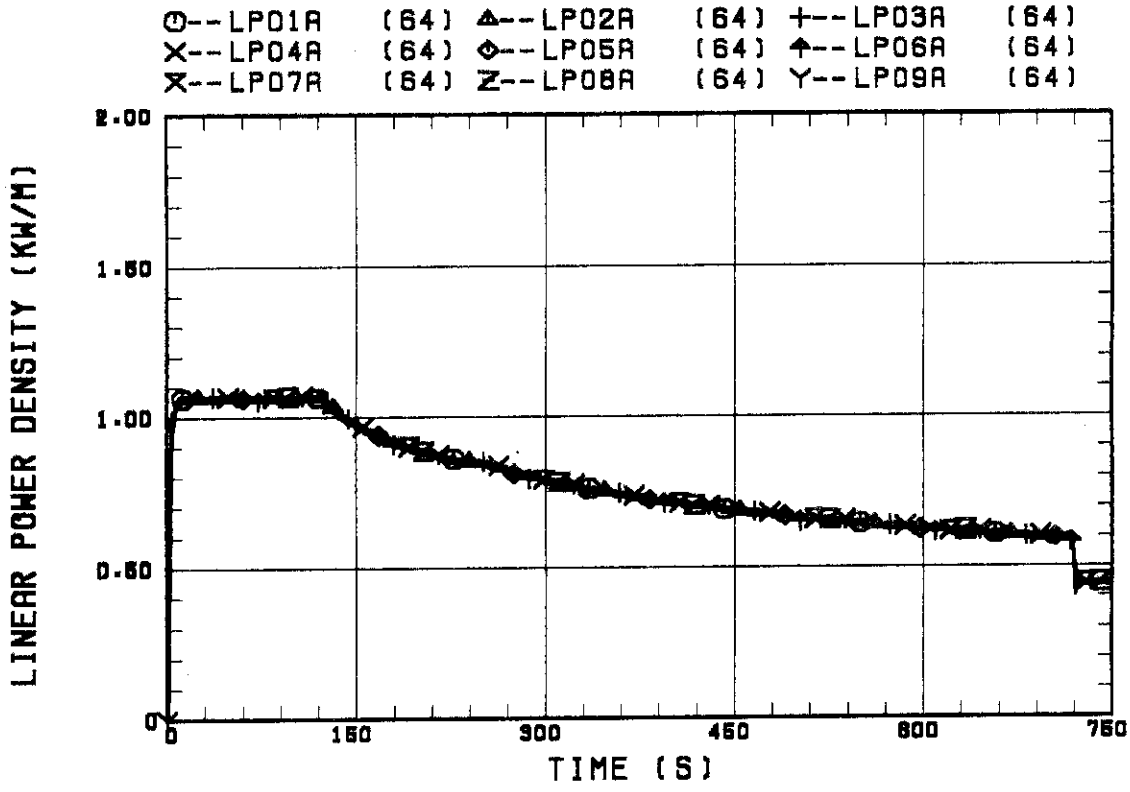

Fig. B.3 Average linear power of heater rod in each power unit zone.

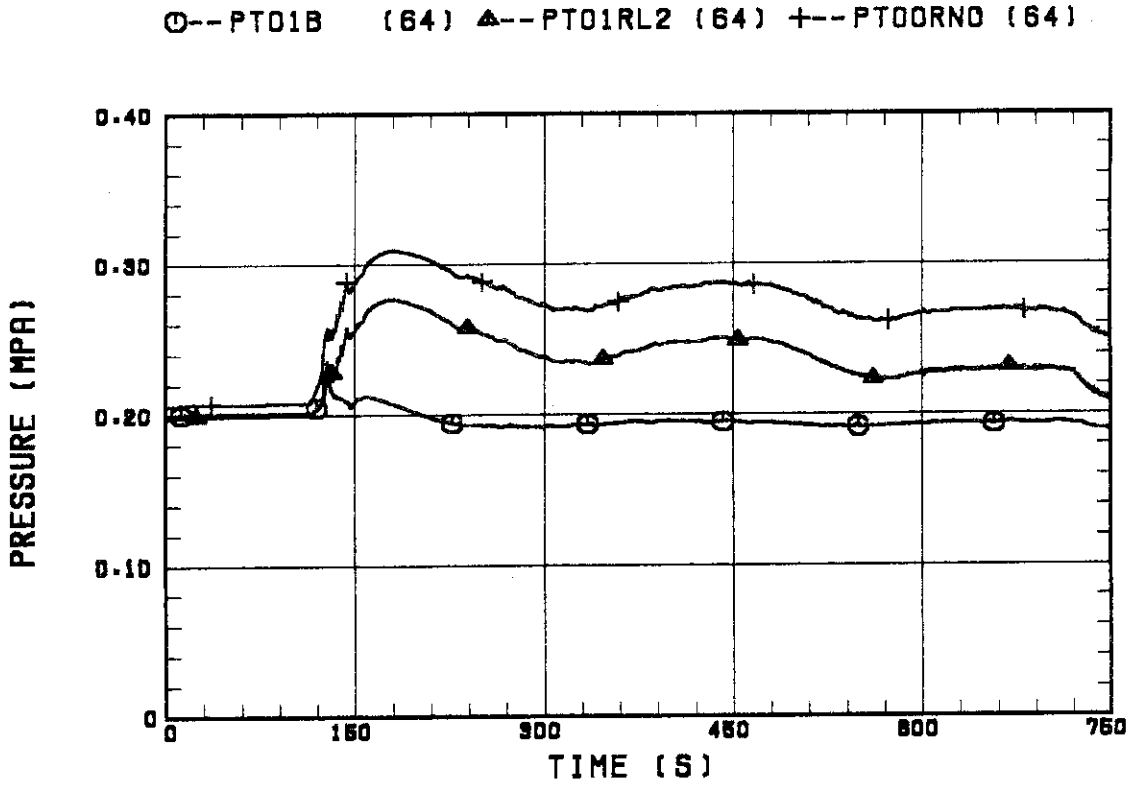

Fig. B.4 Pressure history in containment tank 2, upper plenum and lower plenum.

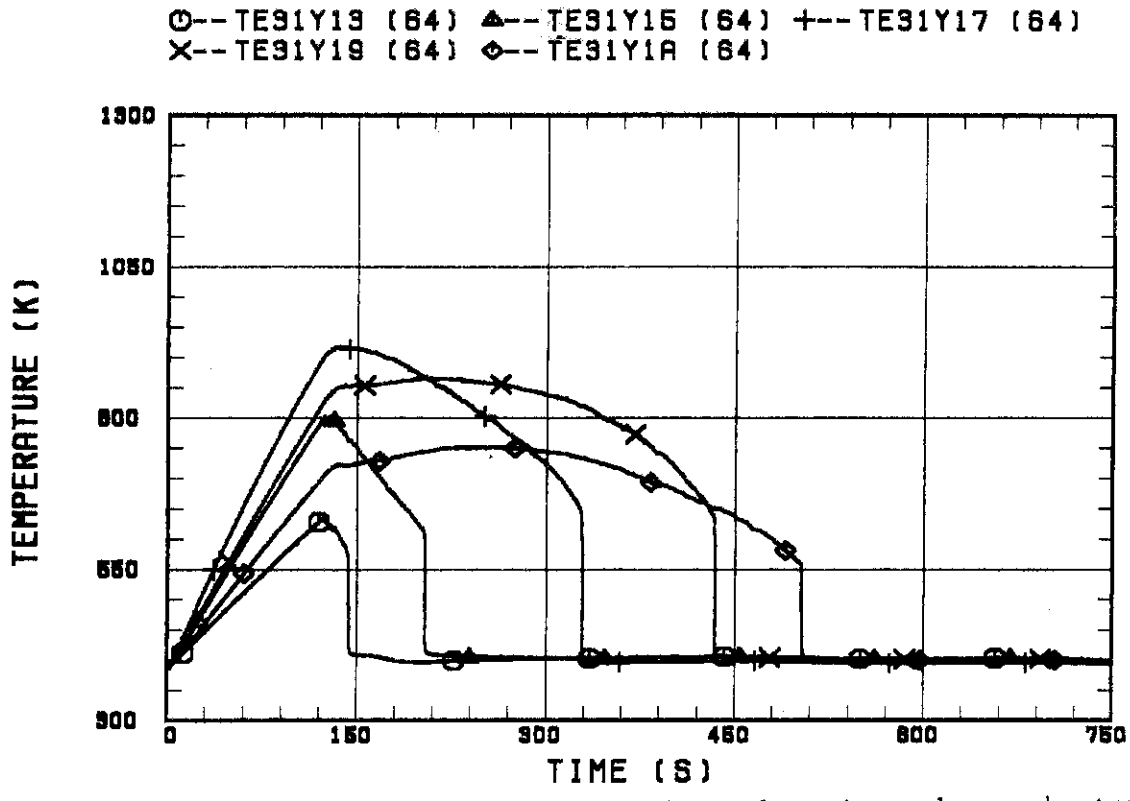

Fig. B.5 Clad surface temperature at various elevations along a heater rod in high power region (A region).

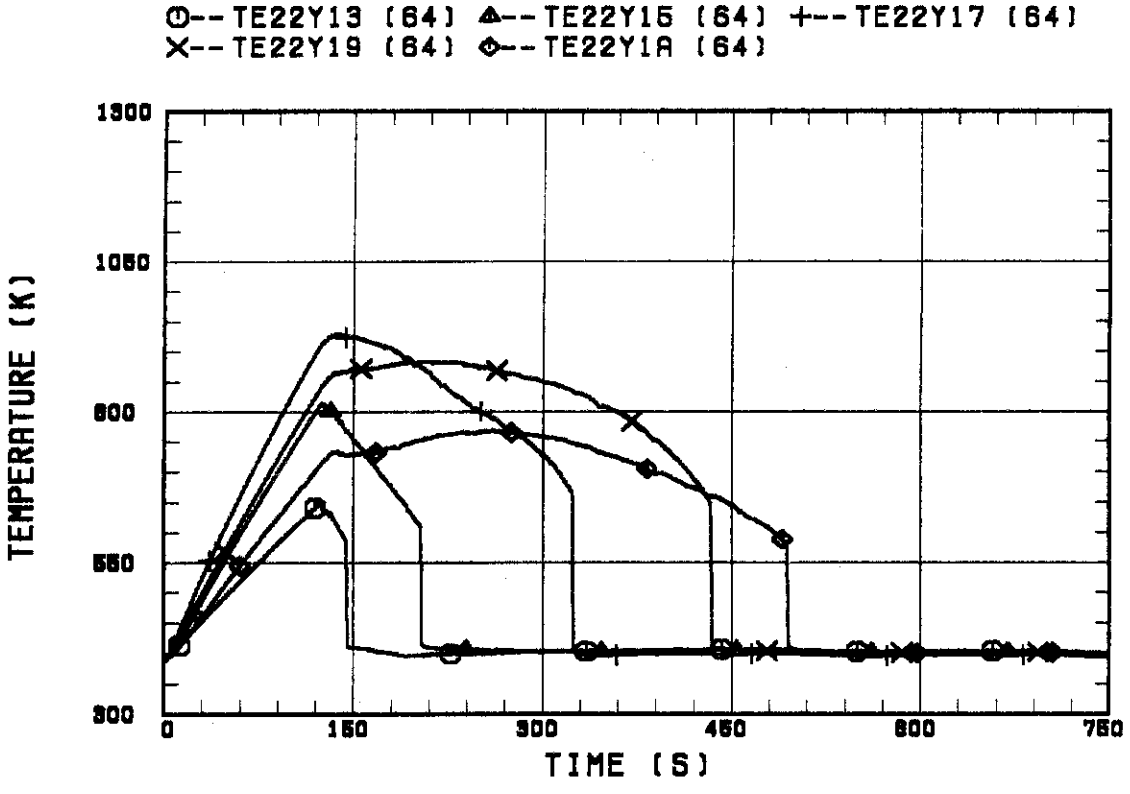

Fig. B.6 Clad surface temperature at various elevations along a heater rod in medium power region (B region).

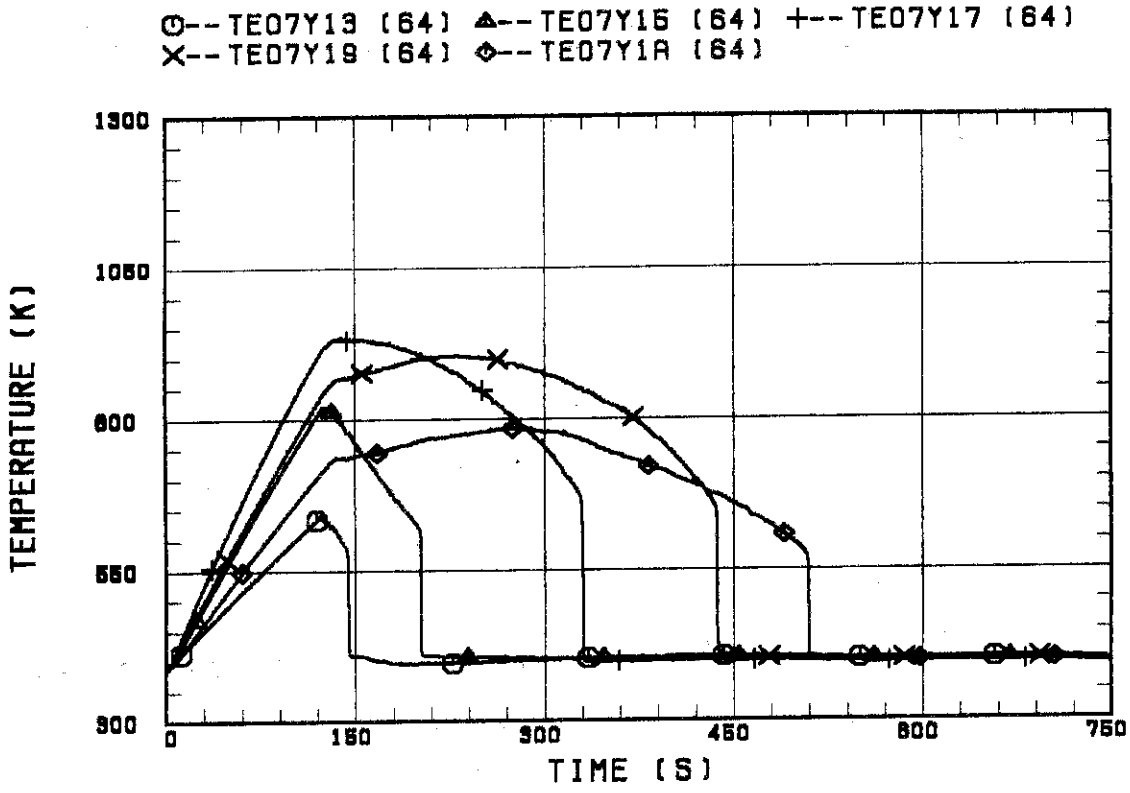

Fig. B.7 Clad surface temperature at various elevations along a heater rod in low power region (C region).

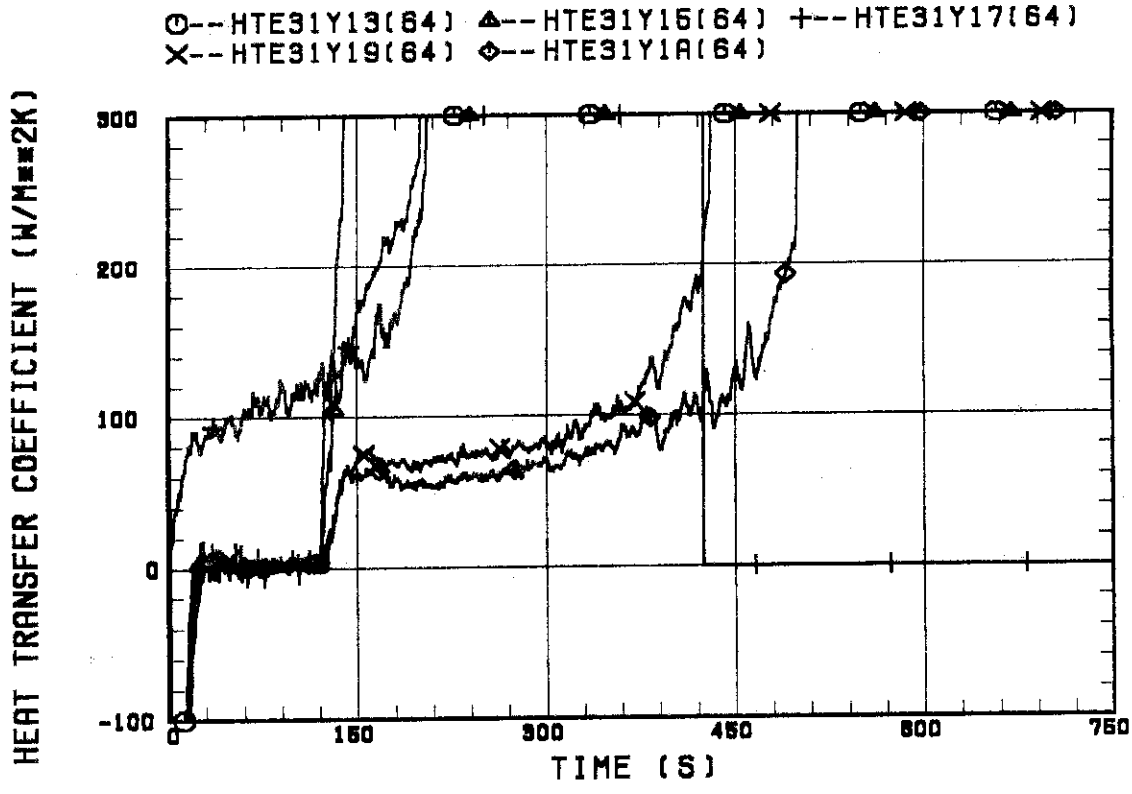

Fig. B.8 Heat transfer coefficient at various elevations along a heater rod in high power region (A region).

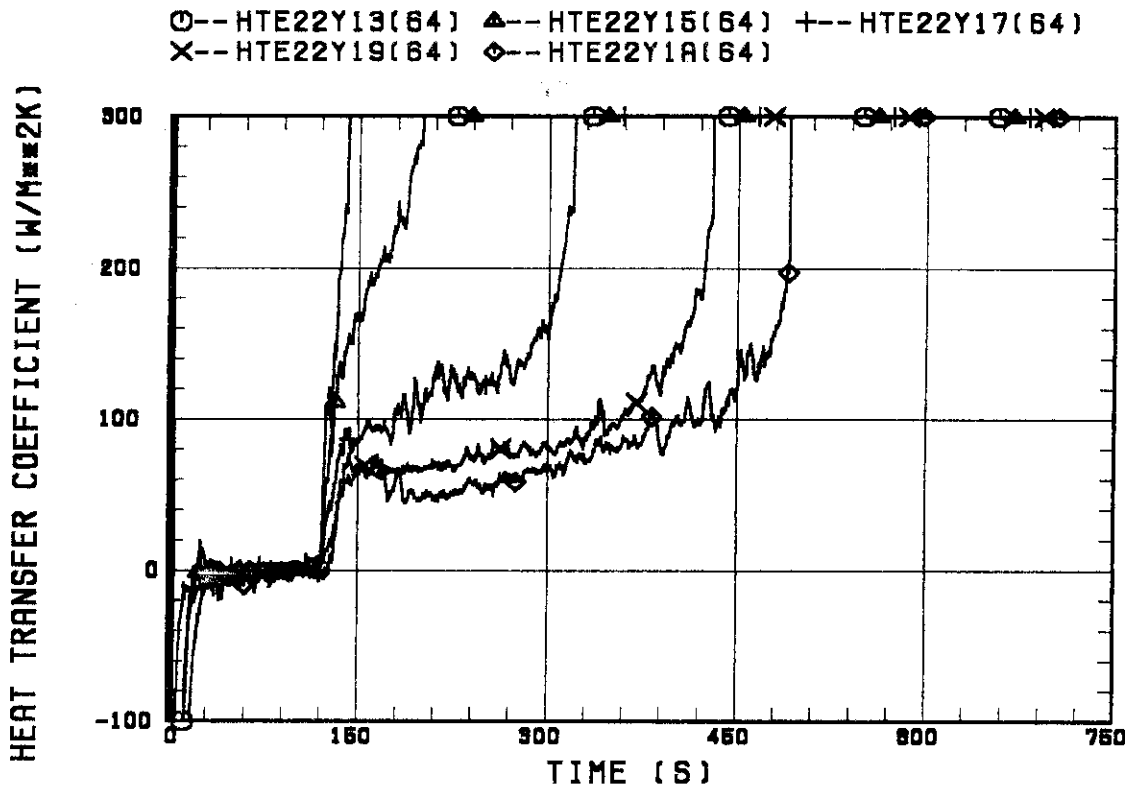

Fig. B.9 Heat transfer coefficient at various elevations along a heater rod in medium power region (B region).

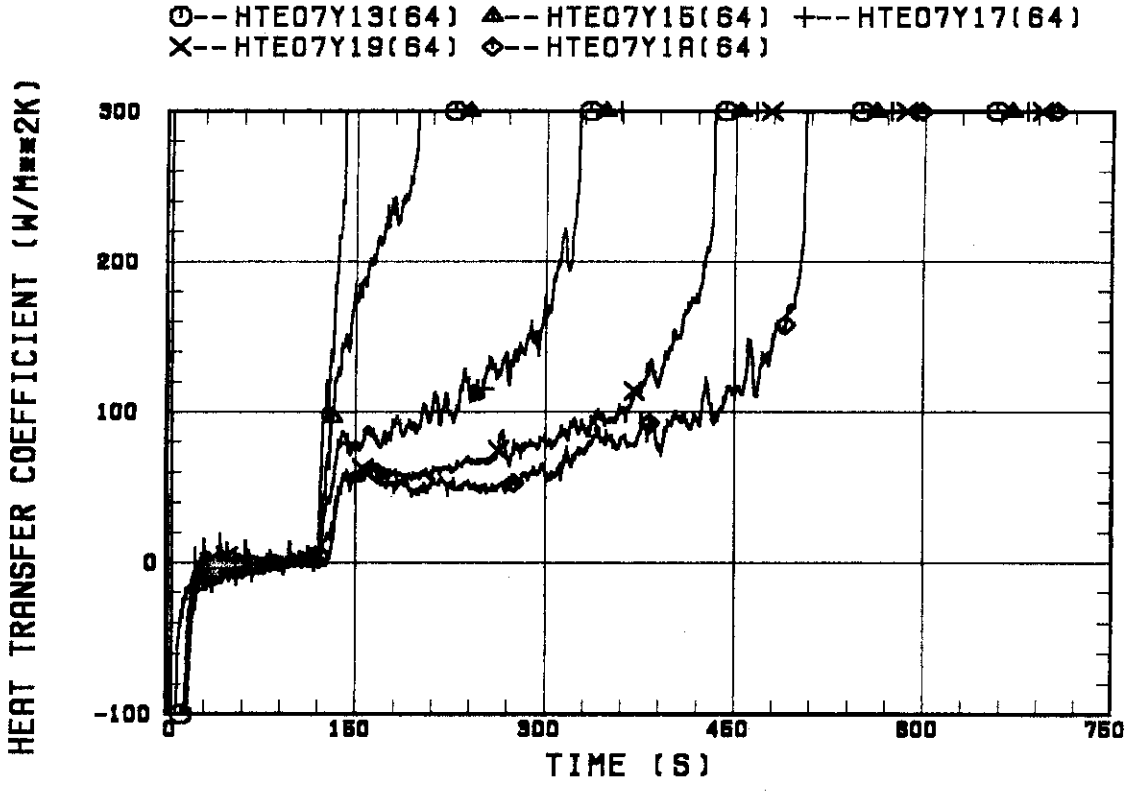

Fig. B.10 Heat transfer coefficient at various elevations along a heater rod in low power region (C region).

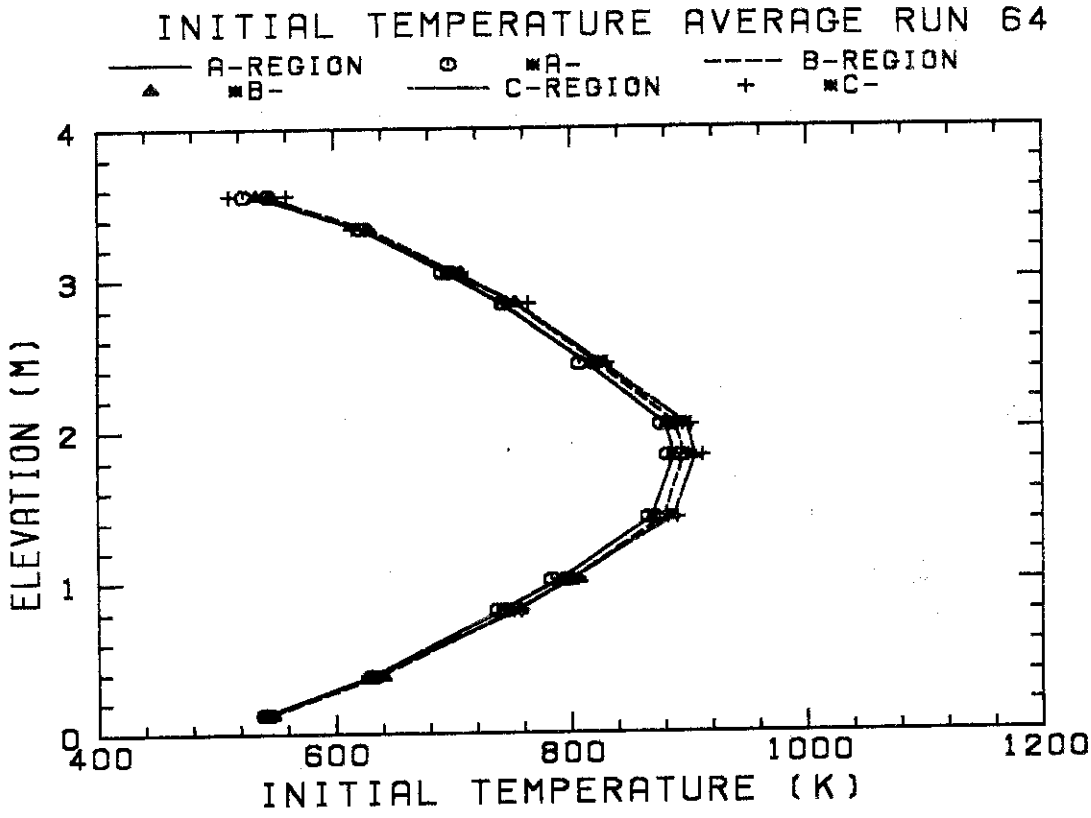

Fig. B.11 Initial clad surface temperature.

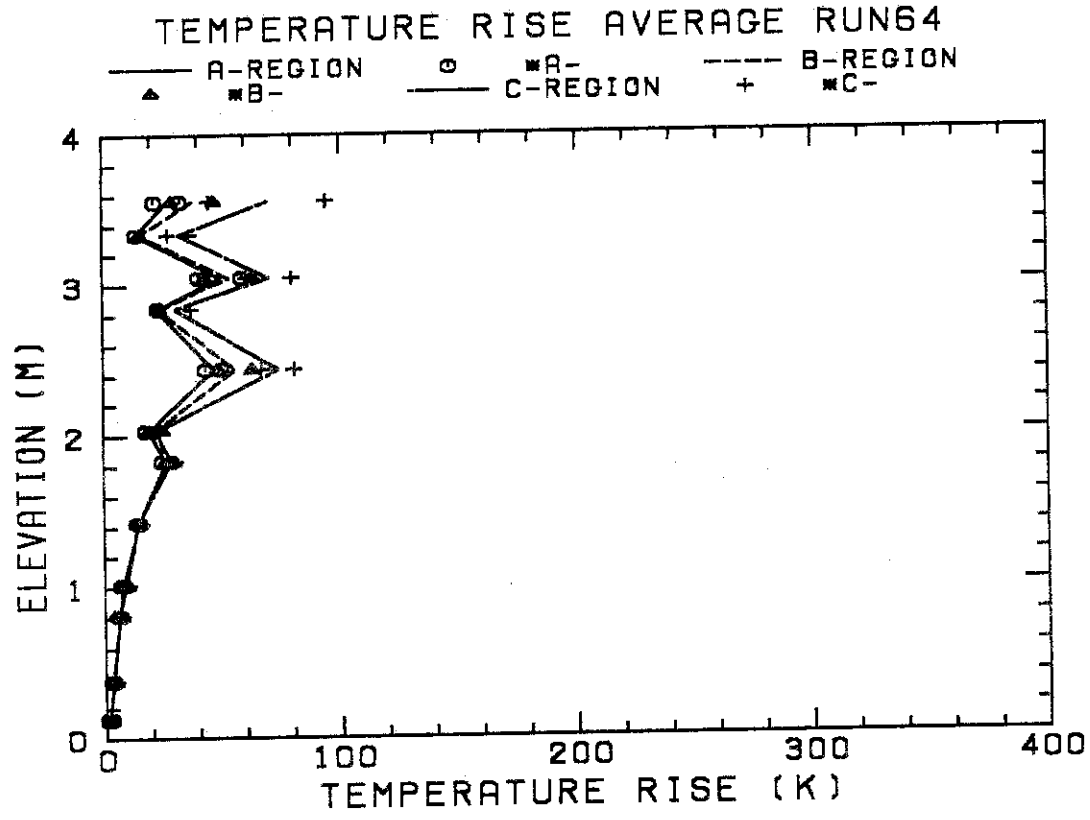

Fig. B.12 Temperature rise.

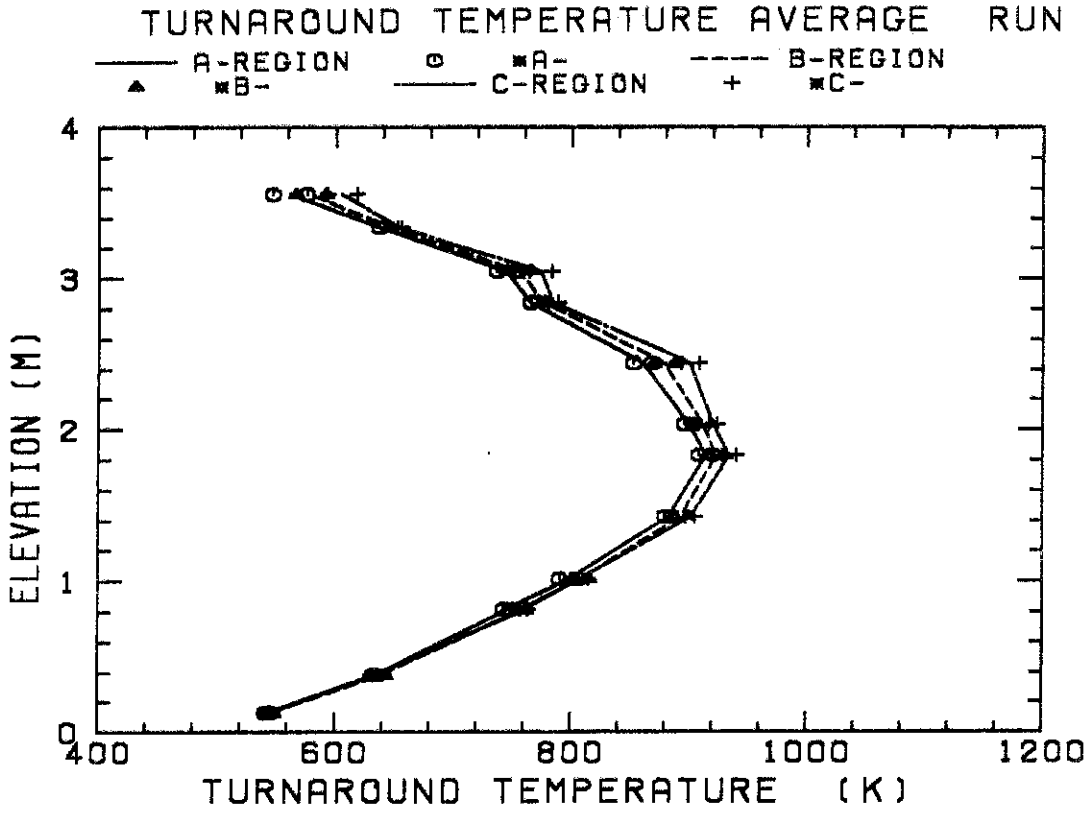

Fig. B.13 Turnaround temperature.

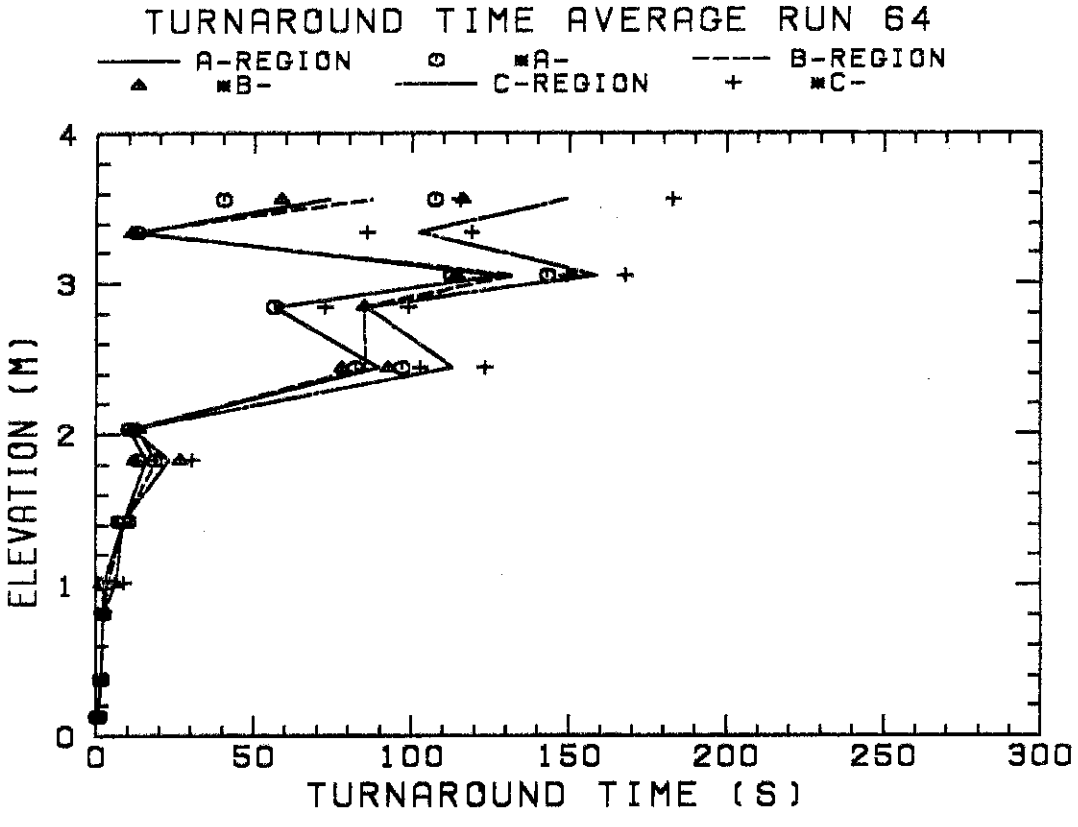

Fig. B.14 Turnaround time.

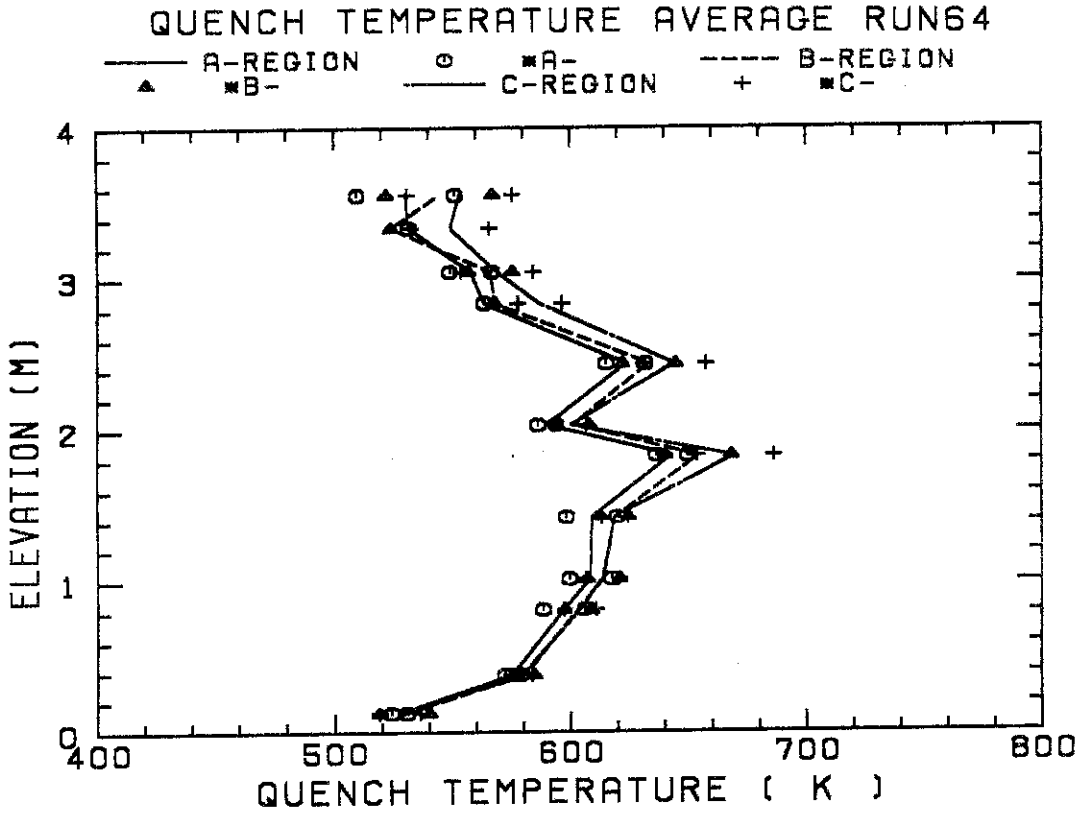

Fig. B.15 Quench temperature.

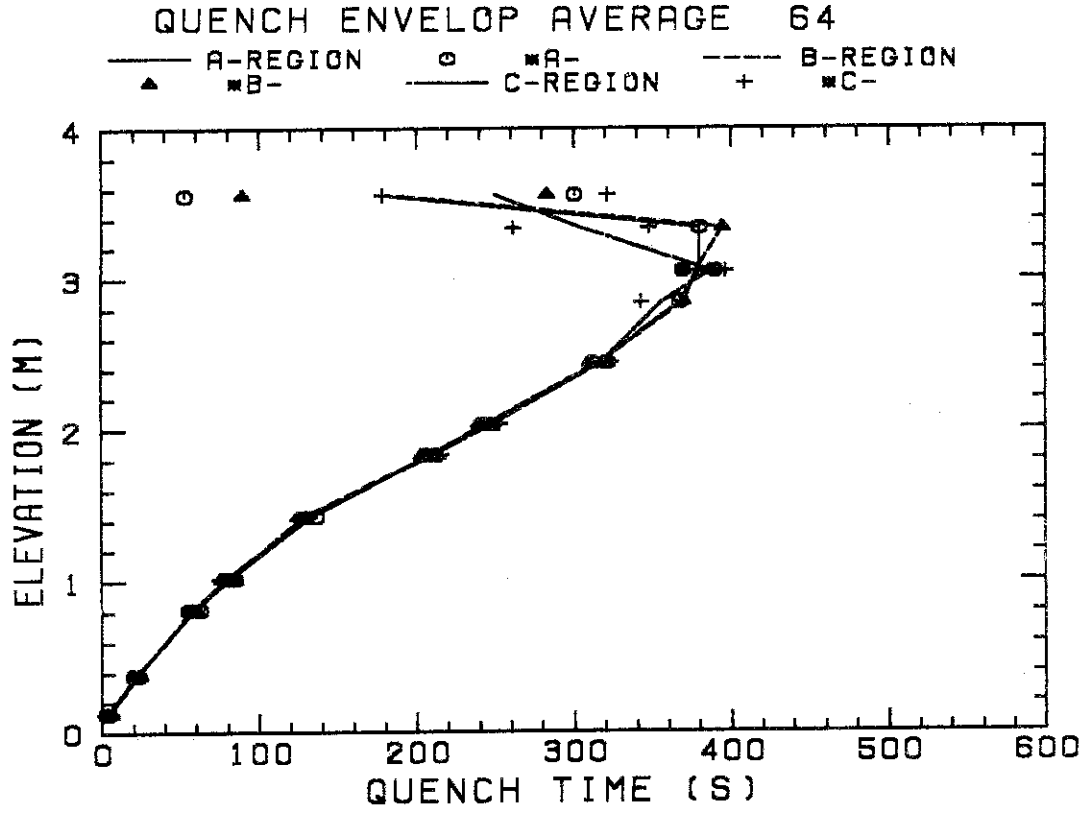

Fig. B.16 Quench time.

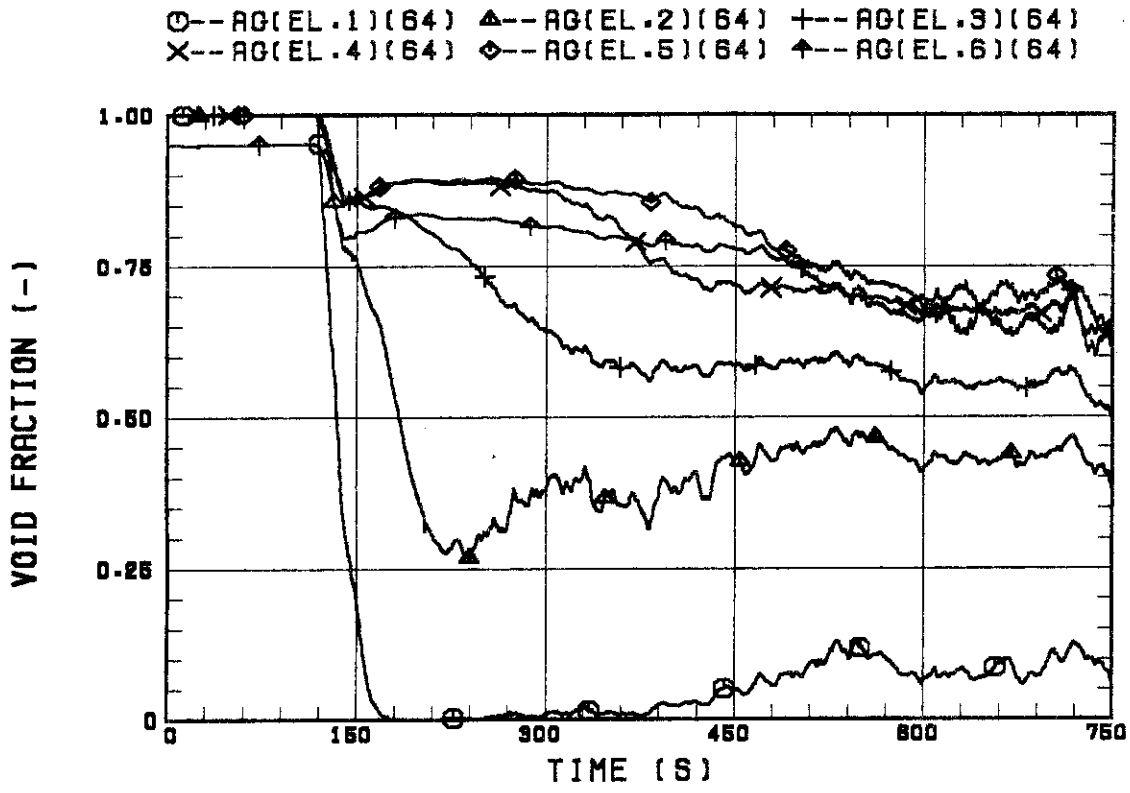

Fig. B.17 Void fraction in core.

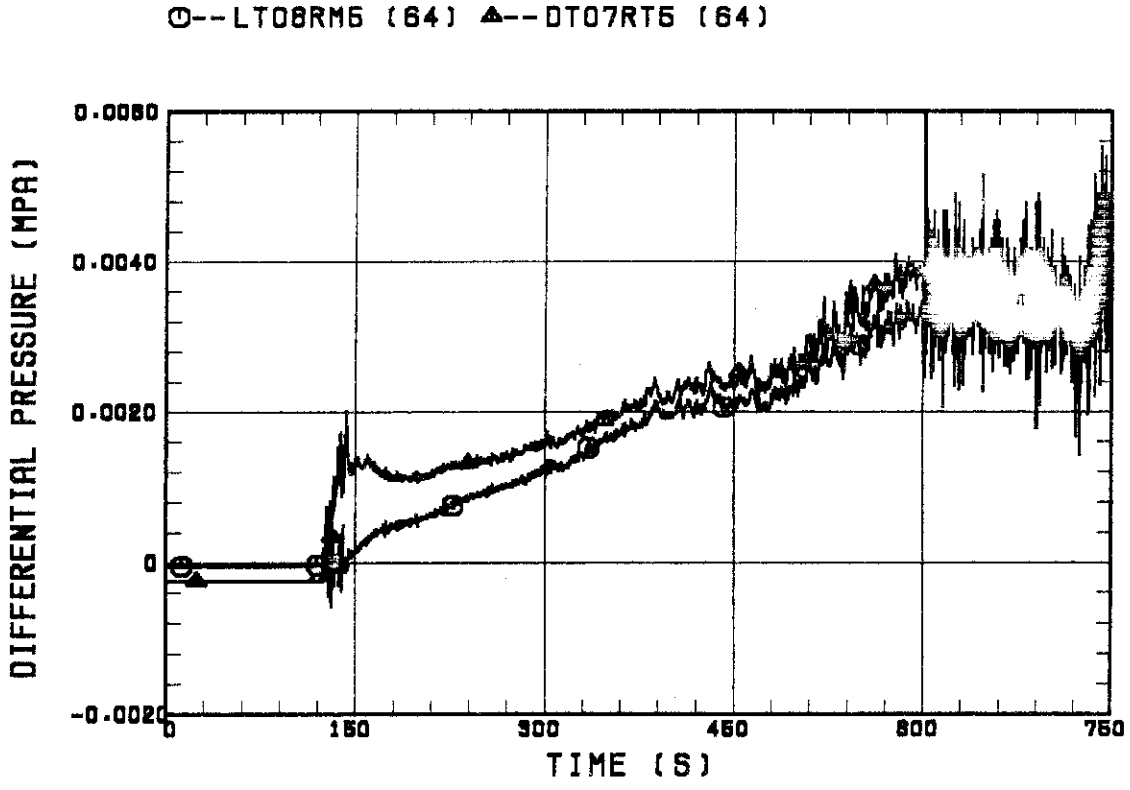

Fig. B.18 Differential pressure through upper plenum.

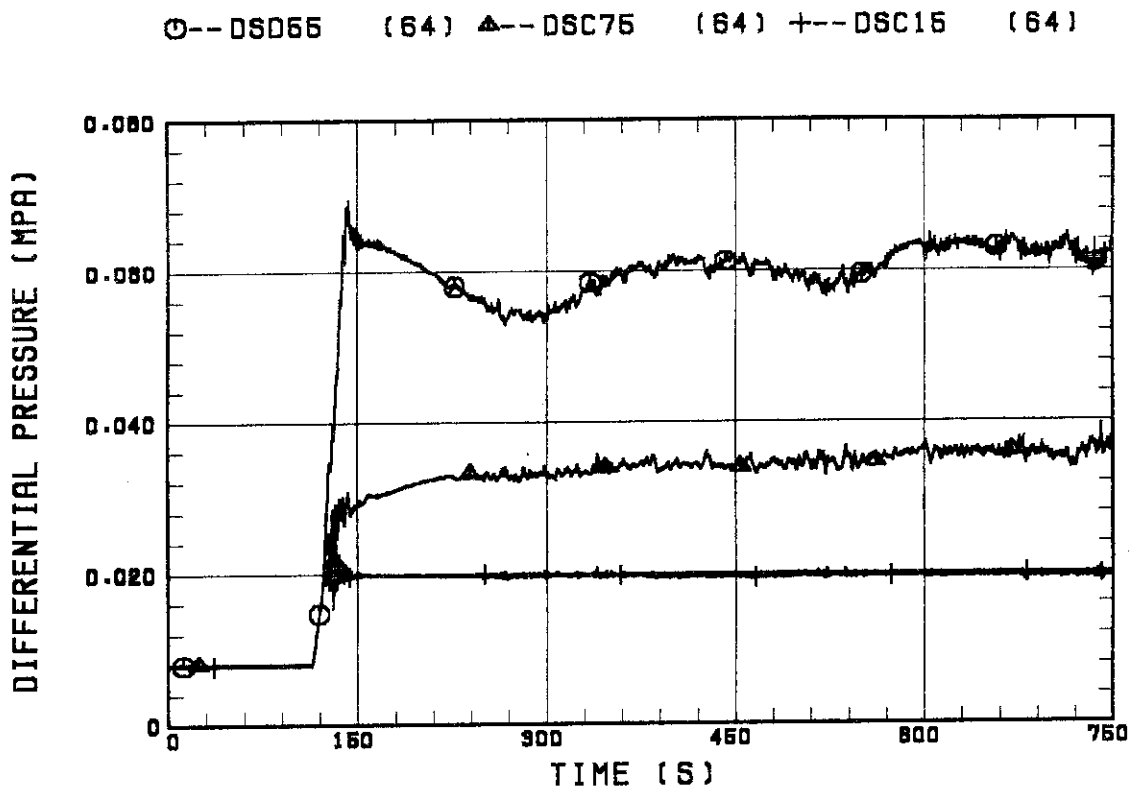

Fig. B.19 Differential pressure through downcomer, core, and lower plenum.

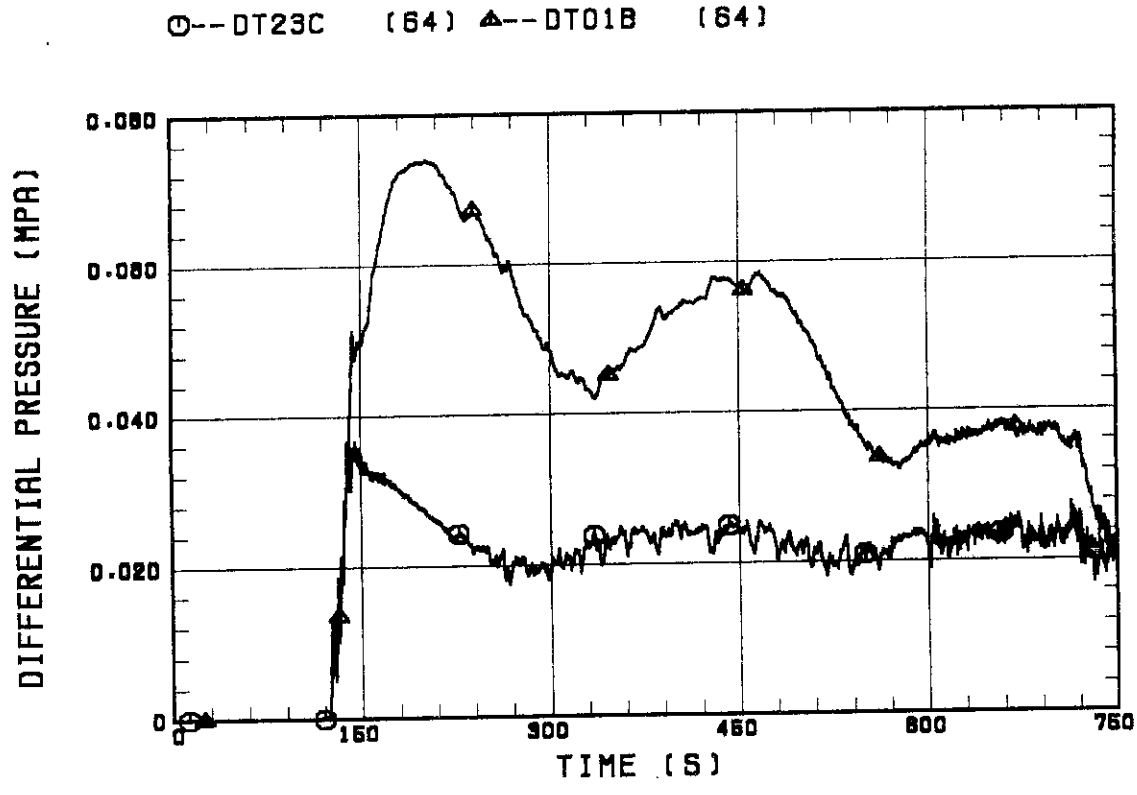

Fig. B.20 Differential pressure through intact and broken loops.

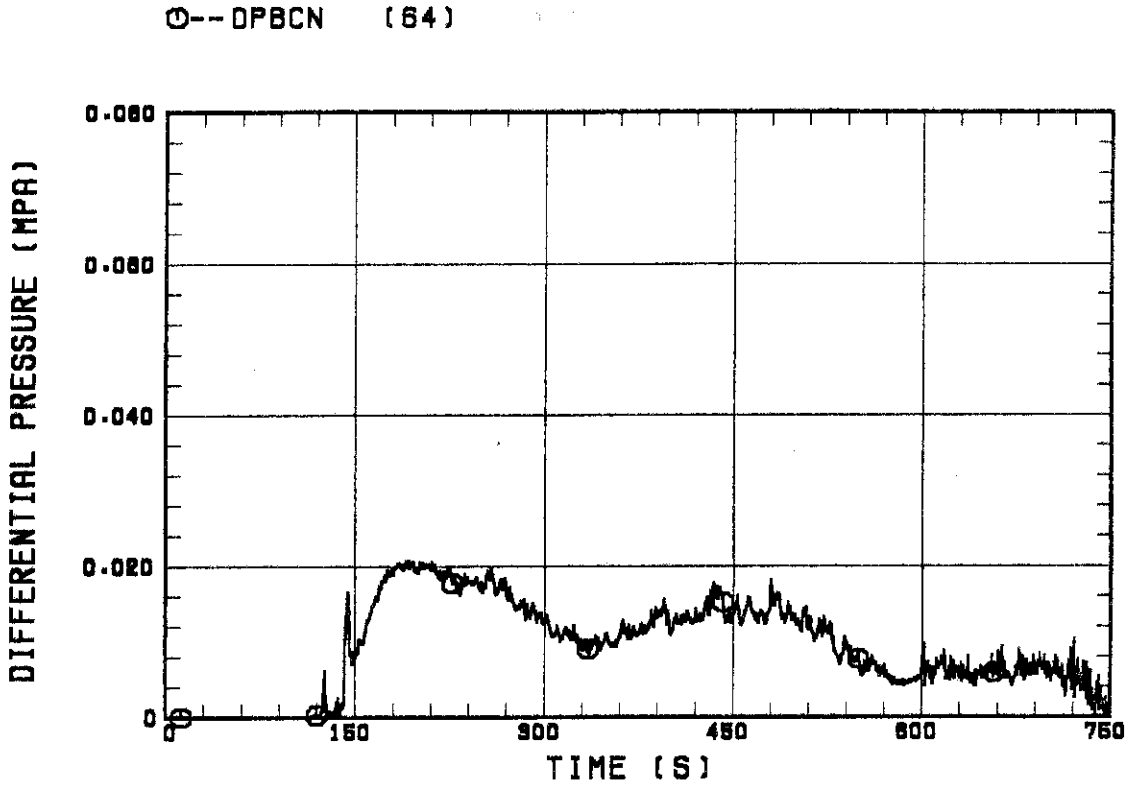

Fig. B.21 Differential pressure through broken cold leg nozzle.

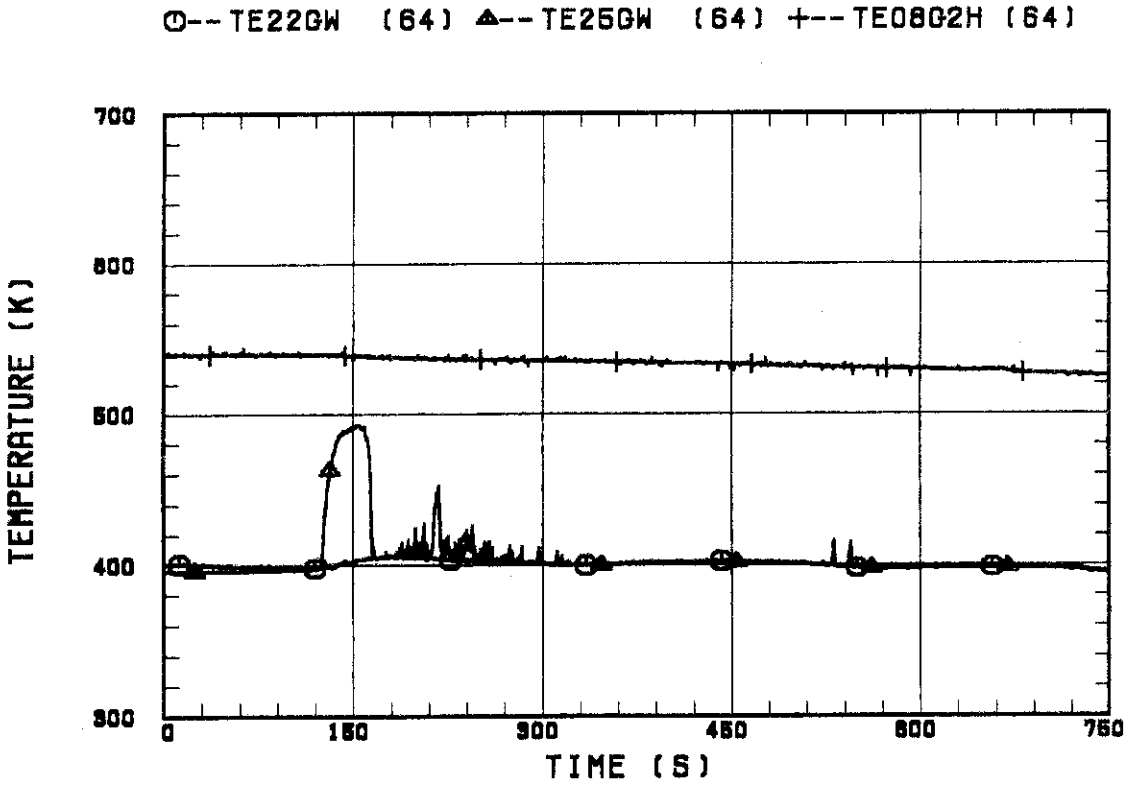

Fig. B.22 Fluid temperature in inlet plenum, outlet plenum, and secondary of steam generator 1.

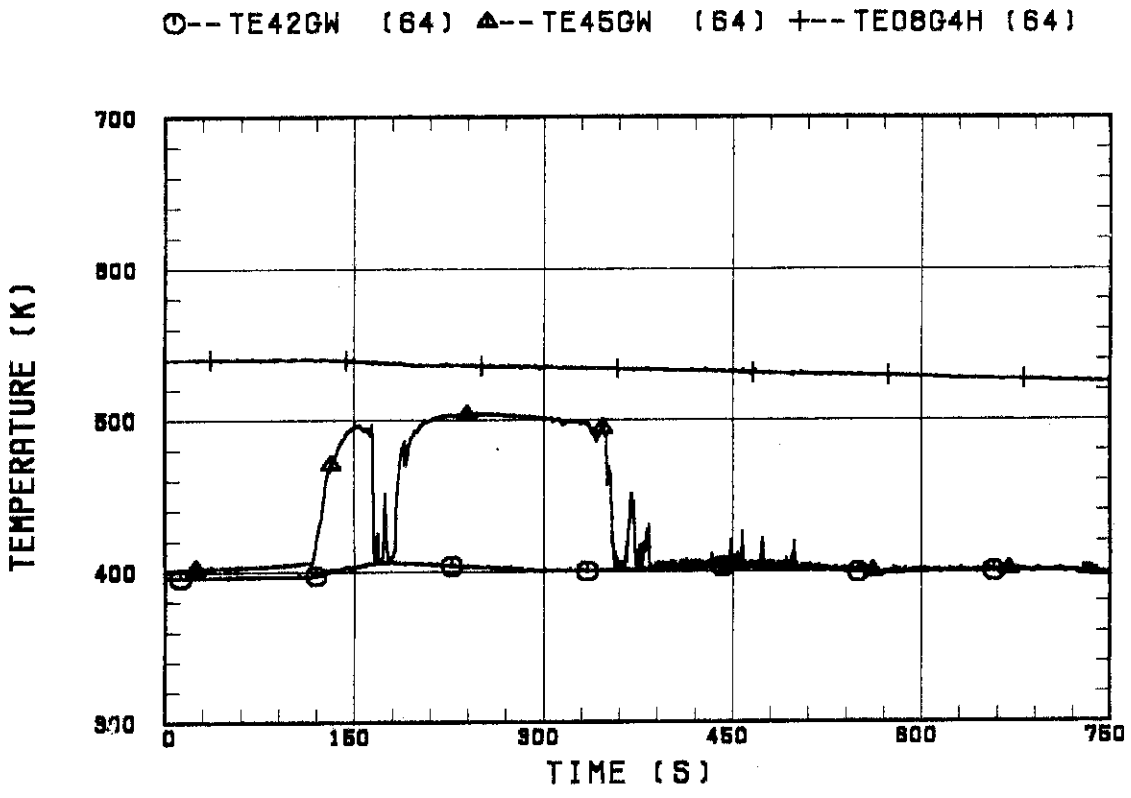

Fig. B.23 Fluid temperature in inlet plenum, outlet plenum, and secondary of steam generator 2.

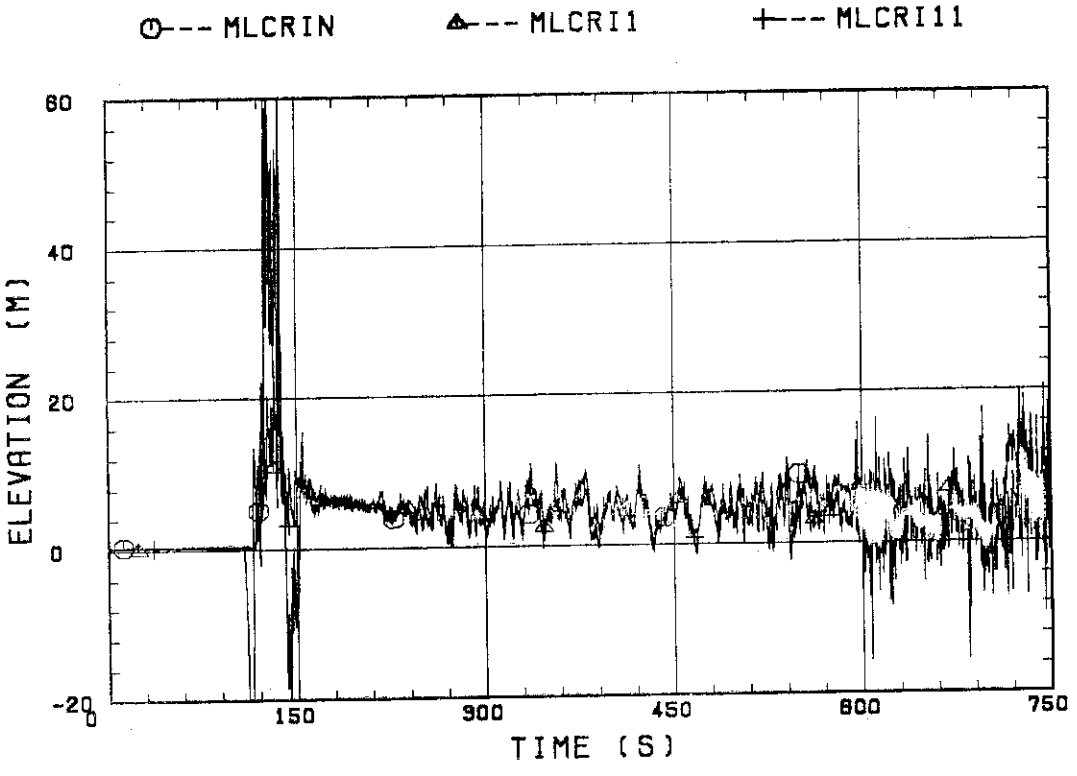

Fig. B.24 Core flooding mass flow rates evaluated with Eqs. (A.1) and (A.2)

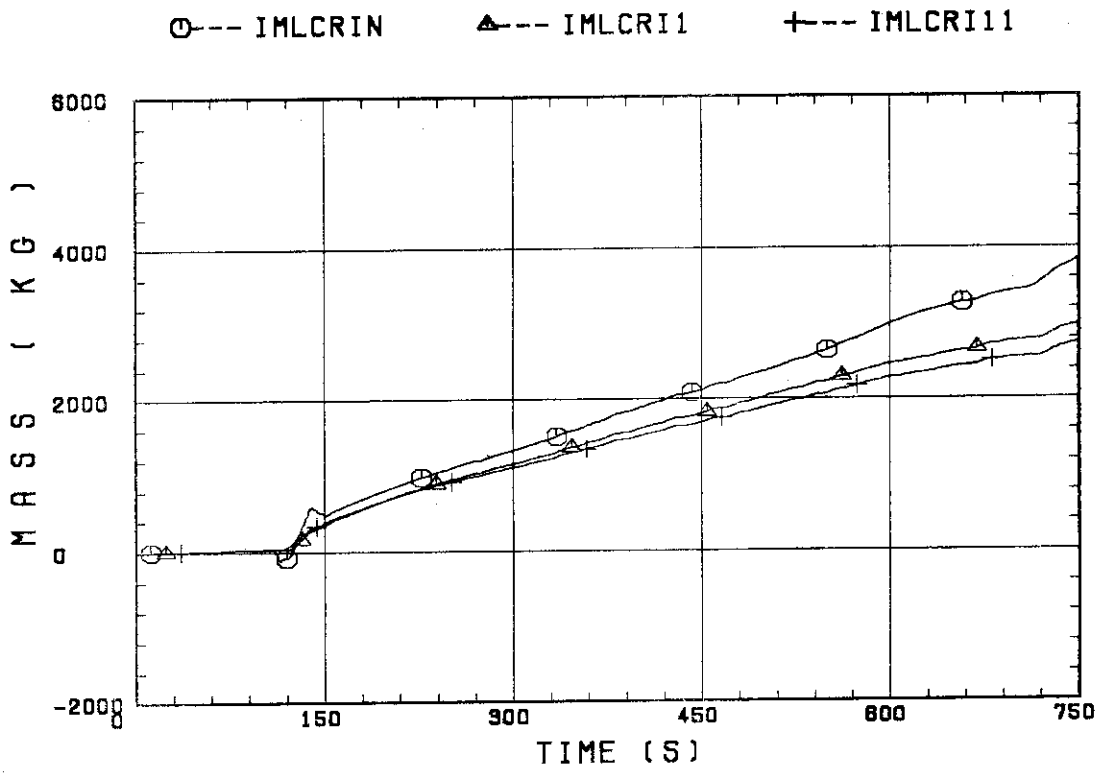

Fig. B.25 Time-integral mass flooded into core evaluated with Eqs. (A.1) and (A.2).

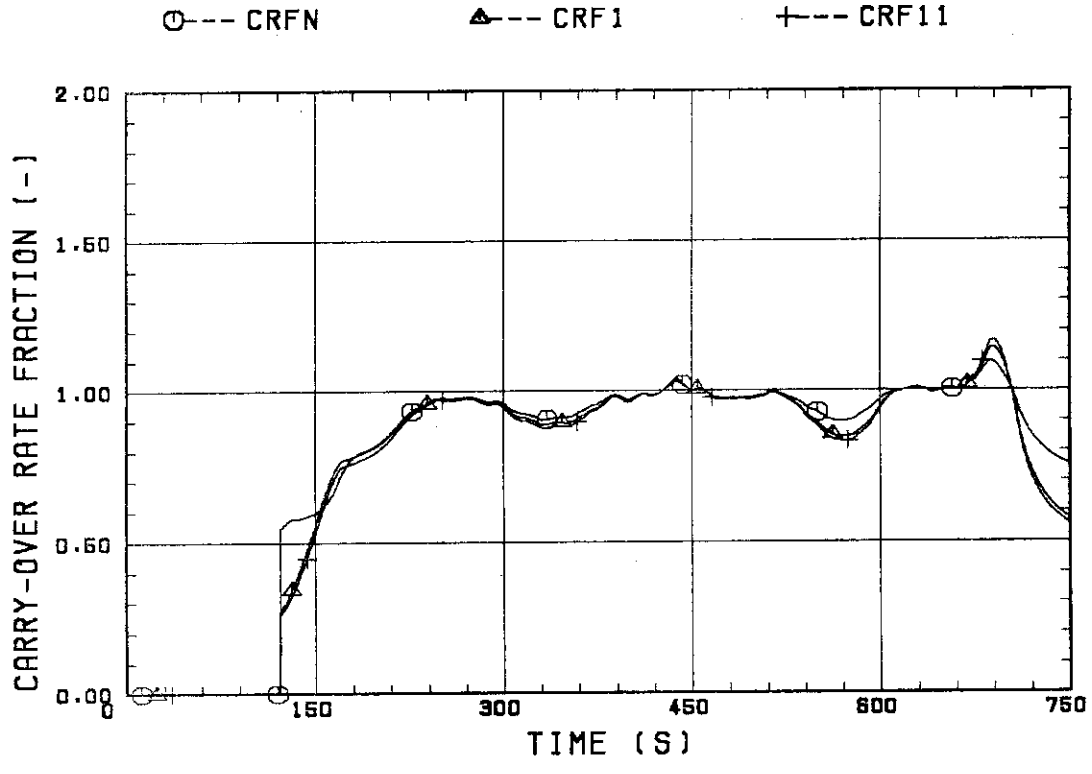

Fig. B.26 Carry-over rate fraction.

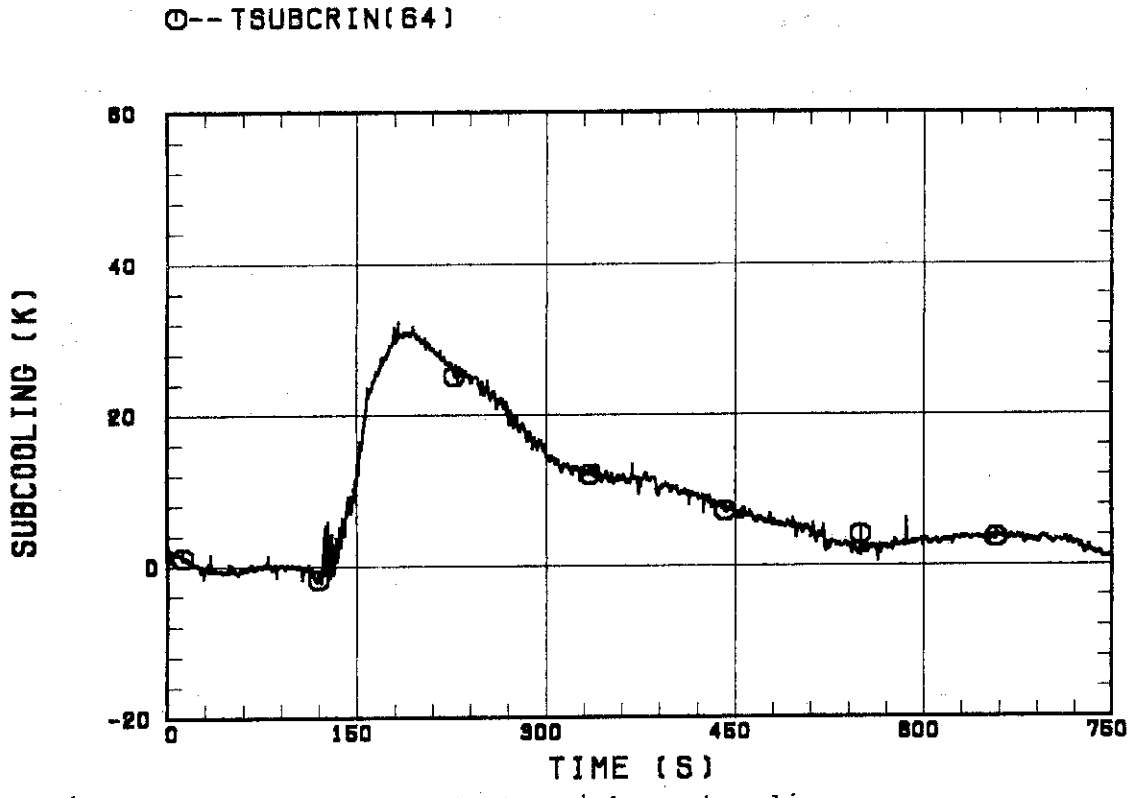

Fig. B.27 Core inlet subcooling.

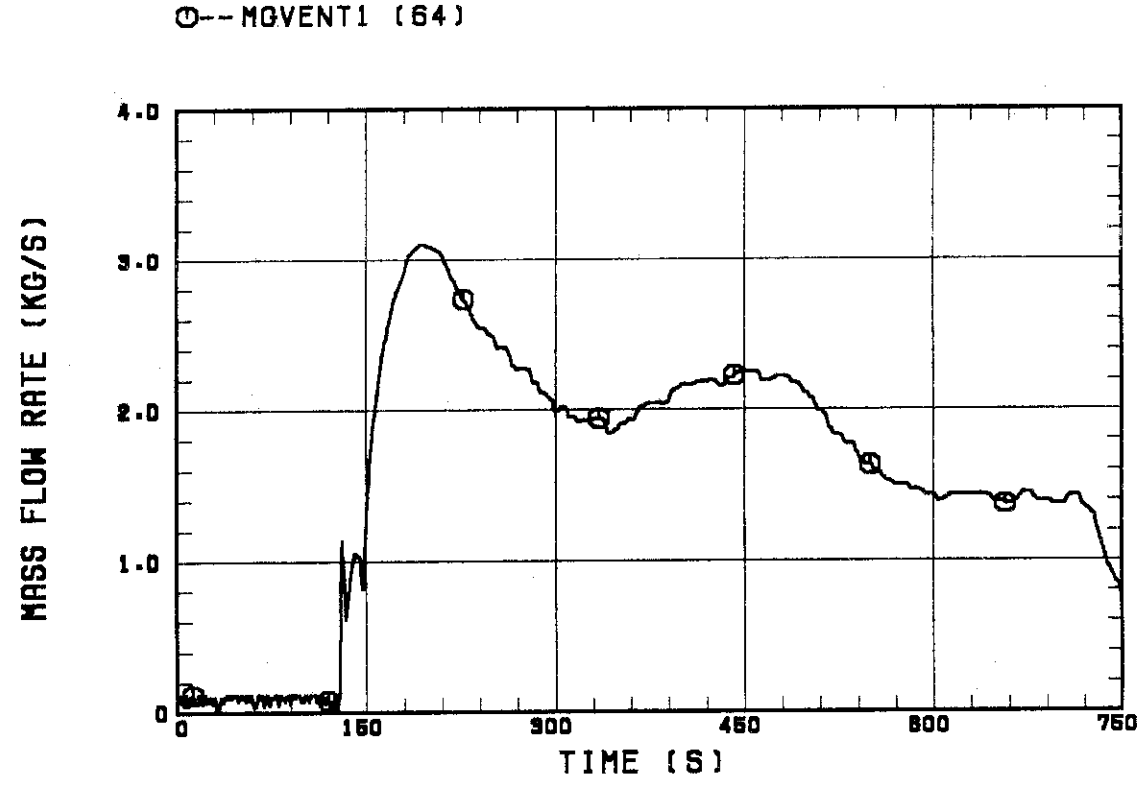

Fig. B.28 Exhausted mass flow rate from containment tank 2.